UNIVERSITY OF CALIFORNIA SAN DIEGO

Developing the Technology of Compaction Self-Assembly for Green Construction Materials

A dissertation submitted in partial satisfaction of the requirements
for the degree Doctor of Philosophy

in

Structural Engineering

by

Haozhe Yi

Committee in Charge:

Professor Yu Qiao, Chair
Professor Shengqiang Cai
Professor Machel L. Morrison
Professor Gilberto Mosqueda
Professor Michael D. Todd

2022

This dissertation of Haozhe Yi is approved, and it is acceptable in quality and form for publication on microfilm and electronically.

University of California San Diego

2022

DEDICATION

This dissertation is dedicated to my parents and my wife.

TABLE OF CONTENTS

LIST OF FIGURES

LIST OF TABLES

ACKNOWLEDGEMENTS

I am deeply grateful to my advisor, Professor Yu Qiao, for his continuous support, invaluable guidance, and patience. I would like to thank my committee members, Professor Shengqiang Cai, Professor Machel L. Morrison, Professor Gilberto Mosqueda, and Professor Michael D. Todd for their valuable suggestions and time.

I would like to thank my colleagues, Dr. Meng Wang, Dr. Ying Zhong, Dr. Rui Kou, Dr. Kiwon Oh, and Mr. Zhaoru Shang for their help and suggestions.

I would like to thank my parents and my wife for their endless support.

Chapter 2, in full, is a reprint of the material as it appears in Sustainable Materials and Technologies. Haozhe Yi, Kiwon Oh, Rui Kou, and Yu Qiao, 2020. Sand-filler structural material with a low content of polyethylene binder. 25 (2020): e00194. The dissertation author was the primary investigator and first author of the paper.

Chapter 3, in part, is currently being prepared to be submitted for publication. Haozhe Yi, Kiwon Oh, Rui Kou, and Yu Qiao. Algae-based artificial timber with an ultralow binder content. The dissertation author was the primary investigator and first author of the paper.

Chapter 4, in part, is currently being prepared to be submitted for publication. Haozhe Yi, Kiwon Oh, Rui Kou, and Yu Qiao. The dissertation author was the primary investigator and first author of the paper.

Chapter 5, in part, is currently being prepared to be submitted for publication. Haozhe Yi, Kiwon Oh, Rui Kou, and Yu Qiao. “Sectioned Compaction of Low-Binder Concrete Parts”. The dissertation author was the primary investigator and first author of the paper.

Chapter 6, in part, is currently being prepared to be submitted for publication. Haozhe Yi, Kiwon Oh, Rui Kou, and Yu Qiao. The dissertation author was the primary investigator and first author of the paper.

Chapter 7, in part, is currently being prepared to be submitted for publication. Haozhe Yi, Kiwon Oh, Rui Kou, and Yu Qiao. The dissertation author was the primary investigator and first author of the paper.

Chapter 8, in part, is currently being prepared to be submitted for publication. Haozhe Yi, Kiwon Oh, Rui Kou, and Yu Qiao. The dissertation author was the primary investigator and first author of the paper.

VITA

2022	Doctor of Philosophy	University of California San Diego
2018	Master of Science	University of Virginia
2015	Bachelor of Engineering	Dongguan University of Technology

ABSTRACT OF THE DISSERTATION

Developing the Technology of Compaction Self-Assembly for Green Construction Materials

by

Haozhe Yi

Doctor of Philosophy in Structural Engineering

University of California San Diego, 2022

Professor Yu Qiao, Chair

Modern concrete has been the major construction material for nearly two centuries. Portland cement, the binder in modern concrete, is being produced worldwide in large quantity (more than 3 billion tons per year). However, cement production is pollutive and energy inefficient. It is a main source of greenhouse gas emission, and the energy consumption is significant. For the past a few decades, a number of “green concrete”

concepts have been extensively studied.

In this research, we systematically investigate the technology of compaction self-assembly (CSA). It is a general-purpose processing approach of low-binder-content composites, and can be applied to fabricate ultralow-binder-content polymer cement, algae-derived artificial lumber, and cement-based green concrete. Compared to their conventional counterparts, these materials use small amounts of binders to reach the desired properties. Consequently, the cost-performance balance, the carbon emission, and the energy efficiency can be superior.

In the ultralow-binder-content polymer cement, ~4% polymer binder and ~96% sand form a strong solid. The polymer binder can be unsaturated polyester resin, epoxy, or waste plastics. The artificial lumber uses algae powders as the filler; 2-4% epoxy serves as the binder. The flexural strength is comparable with that of softwoods. It may open a door to upcycling the waste biomass from large-scale algae cultivation. The cement-based green concrete contains only ~14% ordinary portland cement. The key step is the section compaction self-assembly (S-CSA), in which a large part is processed section by section. It may pave the road to green buildings and green infrastructures of low embodied carbon footprint.

Chapter 1 Introduction

1.1 State-of-the-art of green concrete

Manufacturing of ordinary portland cement (OPC) is responsible for 5~10% industry energy consumption (Madlool et al. 2011) and 6~10% human-related CO_2 emission (Benhelal et al. 2013; Ang and Su 2016). The global cement market expanded by more than 400% in the past 40 years (Deja et al. 2010). The annual production reached 4.9 billion tons in 2020, and this number is expected to grow by ~5% per year during 2021-2028 (Pacheco-Torgal et al. 2013; Zhang et al. 2015).

For many decades, researchers have been actively studying the concepts of "green concrete" (Garg and Jain 2014; Suhendro 2014; Liew et al. 2017; Sivakrishna et al. 2020).The goal is to minimize the life-cycle carbon emission and energy use, while maintain the low cost and the adequate structural properties (Garg and Jain 2014). Supplementary cementitious materials (SCMs) are widely used in the cement industry as substitutions to replace part of the clinker used in cement (Juenger and Siddique 2015). It is the most commercially successful method to reduce the cement-industry-associated CO_2 emission (Torgal et al. 2012; Cyr 2013; Pacheco-Torgal et al. 2013; Elahi et al. 2021). Common SCMs include fly ash, silica fume, and blast furnace slag. Based on different applications or specific on-site conditions, SCMs are combined with cement and other active ingredients in different proportions to produce various modified cements, i.e., CEM I, II, III, IV, and V (Thomas 2013; Błaszczyński and Król 2015). The added SCMs usually help enhance the workability and lower the water requirement, which often leads to a considerable strength improvement. It reduces the heat generation during the hydration process, which mitigates thermal cracking. The durability, impermeability, and

sustainability of the cured concrete structures can also be improved, which is beneficial to the chemical resistance, especially for harsh environments. However, the development of the traditional SCMs is limited by the insufficient raw materials supplies. For instance, compared with the amount of OPC, the produced slag is only about 5-10%, much less than the 25-50% mixing proportion (Torgal et al. 2012; Scrivener et al. 2018). The produced fly ash is about 30% of OPC, but only around 1/3 of the fly ash is qualified for the use of cement additive (Scrivener et al. 2018), much less than the replacement ratio of 15-30% (Lloyd and Rangan 2010; Motorwala et al. 2013). The resource distribution of slag is highly dependent on the local steel industry, which may demand a high transportation cost and the associated heavy CO_2 emission. Furthermore, for the past decade, coal-based electricity production has been gradually replaced by cleaner methods, such as nuclear power, wind power, and hydroelectric power(Lew et al. 2021). The supply of fly ash will be in a decreased trend in the future. For silica fume, as a by-product of elemental silicon or silicon-doped alloy, the available amount is about 30-40 times less than that of concrete (Siddique 2011; Scrivener et al. 2018).

A novel SCM-modified material, limestone calcined clay cement (LC^3), attracted great attention in recent years. LC^3 uses calcined clay and limestone as substitutions, to partially replace OPC. It was developed to overcome the insufficient supply of traditional SCM. Clay is widely available worldwide. Calcined at 700~850 ℃, kaolinite from the clay transfers to metakaolin, and then reacts with calcium hydroxide to form a C-A-S-H hydrate (Sharma et al. 2021). Strength is achieved during the hydration process, similar to that of conventional pozzolanic materials, but usually with a better early strength due to the high material activity. For example, LC^3-50 has been proven strong with plain OPC at 7 days;

it is a combination of 50% ground clinkers, 30% calcined clay, 15% limestone, and 5% gypsum (Alujas et al. 2015; Avet et al. 2016). The 50% clinker replacement is attractive, compared to the conventional SCMs. One issue is that the calcination process may increase the cost. Therefore, a cheap and abundant raw material, limestone, is combined with the calcined clay as a substitution. Compared with the high temperature (~1450 ℃) used for clinker calcination, the 700-800 ℃ processing temperature of clay can avoid many technical difficulties, reduce the cost, and be safer.

Developing carbon negative materials is an emerging direction of research on green concrete. They are materials that emit less CO_2 than the sequestered CO_2 during the production process, so that the total CO_2 footprint is negative (Detz and van der Zwaan 2019). One example is C2CNT (CO_2 to carbon nanotube) cement plants (Licht 2017). CO_2 is captured by dissolving the exhaust from the cement plants into soluble carbonates (e.g., Li_2O) and forms molten carbonates (e.g., Li_2CO_3). Electrolysis is applied to split the captured CO_2 into solid carbon and O_2, and Li_2CO_3 is reduced to Li_2O. The generated carbon can be either carbon nanofibers (CNFs) or carbon nanotubes (CNTs), which have superior strength, remarkable electrical conductivity and thermal conductivity. The nontrivial cost from carbon capture and electricity usage may be balanced by the high-value CNFs or CNTs.

Over the years, OPC manufacturing is being continuously improved to enhance the material properties, to minimize the CO_2 emission, and to save energy (Mehta 2002; Mehta 2009; Meyer 2009). Typically, the crushed raw materials are dried and grinded in two separated chambers of raw mills. After grinding, the fine material (the raw meal) is separated from the coarse material, and fed into the preheater. The coarse material is sent

back for regrinding. After preheating, the raw meal, now called kiln feed, is calcined in a rotary kiln at ~1450 ℃ to form clinkers, followed by cooling down to about 120 ℃. Clinkers and gypsum, together with SCMs if applicable, are added into cement mills for grinding. The collected fine cement powders are stored in concrete silos for later packing. During this process, grinding and calcination are the critical steps. High-activation grinding was developed to boost the reactivity of each component in OPC (Hasanbeigi et al. 2012). High-energy mill is used for material activation (Cheng et al. 2012; Hasanbeigi et al. 2012). Studies showed that milled fly ash and blast furnace slag both benefit the concrete strength (Pavlů 2018). Fluidized-bed advanced cement kiln system (FAKS) was developed for next-generation calcination (Hasanbeigi et al. 2012). Different from the conventional rotary kilns, no movable fixtures are involved in the FAKS. Clinkers are produced in a fluidized bed kiln and cooled in a two-stage cooler system, formed through a self-granulation process. That is, a part of the raw materials are transferred to the granule cores first, and then the remaining materials are attached on these granule cores to form clinkers of a certain size. The size of the produced clinkers is 1.5~2.5 mm, which is much smaller than that of conventional clinkers. Thanks to the efficient heating technology, the CO_2 emission is decreased, due to reduced fuel consumption. Lower grade fuels are acceptable for this system. The combustion happens in the fluidized bed with no flame, so that the NO_x emission is decreased. The immobile structure leads to a low capital cost, a low maintaining cost, and excellent robustness. Currently, the R&D in this area is focused on system scaling-up.

Geopolymer-based green concrete has been extensively studied for more than two decades (Hardjito et al. 2004; Rangan 2008; Lloyd and Rangan 2010; Motorwala et al.

2013; Singh et al. 2015). When activated by a strong alkali solution, class-F fly ash or furnace slag can form a structurally integral alumino-silicate network, which may be stronger than regular OPC-based concrete and has a much faster curing process (Rangan 2008; Oh, Yi, Kou, et al. 2020a). It also has excellent workability, adequate fire resistance, and satisfactory chemical resistance (Singh et al. 2015). However, due to the reduced fossil fuel usage, in many areas in the U.S., class-F fly ash is being increasingly unavailable (Scrivener et al. 2018). The relatively high cost and the relatively large carbon emission associated with the use of the alkali solution also impose tough challenges (Lloyd and Rangan 2010; McLellan et al. 2011).

Polymer cement is another interesting structural material (Darnell 1991; Do and Soh 2003; Bozkurt and İslamoğlu 2013). By bonding aggregates (such as sand and gravel) directly by 10~15% polymer binder, the strength is usually much higher than that of OPC-based concrete, especially the flexural/tensile strength (Bedi et al. 2013; Bozkurt and İslamoğlu 2013). The durability and the water resistance are also superior , and the setting procedure typically takes only a few hours (Wongpa et al. 2010). The limiting factor is the high cost and the large overall carbon emission, associated with the use of the relatively large amount of polymer binder (e.g., unsaturated polyester resin).

1.2 Development of the compaction self-assembly technology

Recently, we developed the technology of compaction self-assembly (CSA) for the production of ultralow-binder-content (UBC) composites (Oh et al. 2019; Yi et al. 2020a; Oh, Yi, Kou, et al. 2020b; Oh, Chen, Kou, et al. 2020a). A filler (e.g., sand) and a binder (e.g., epoxy) were premixed first. The binder content could be as low as 2~4 wt%. The mixed material was transferred into a mold and compacted at 30~350 MPa. Under the

relatively high compaction pressure, the microstructure was much densified, and the binder droplets were squeezed to better cover the filler grain surfaces. More importantly, a high capillary pressure was formed in the narrow space between the tightly contacted filler grains. The capillary force effectively redistributed the small binder droplets to the most critical structural joints, to form polymer micro-agglomerations (PMA), which acted as strong connections to carry load. With CSA, composites can be stronger than regular steel-reinforced concrete. Thanks to the low binder content, the cost and the overall carbon emission of UBC composites are minimized.

The CSA technique was employed to produce UBC "lunar cement". The binder was either an unsaturated polyester resin (UPR) or an epoxy. The filler was the JSC-1A lunar soil simulant. Through CSA, only ~4 wt% binder was sufficient to reach a relatively high flexural strength above 20-30 MPa. The material worked well in a broad temperature range from -200 and 130 ℃, relevant to the lunar surface. The processing was fast and relatively simple, and the required equipment could be compact. The main concept was to use a small amount of thermoset binder transported from Earth, and to take advantage of the ample supply of lunar regolith on Moon. In addition to epoxy, thermoplastic binders were also evaluated (Oh, Chen, Kou, et al. 2020a), including polyimide (PI), polyamide (PA), and polyetherketoneketone (PEKK). Compared with thermosets, the thermoplastic binders might improve the material in some aspects, such as the durability, the recyclability, and the UV resistance. With only ~4 wt% PEKK binder, the flexural strength of the UBC "lunar cement" was comparable with typical steel-reinforced concrete. When the PEKK content was raised to ~6 wt%, the flexural strength could be as high as ~35 MPa.

The CSA process has been applied to fabricate geopolymer-based green concrete

(Oh, Yi, Kou, et al. 2020a). To subsist on the rapidly decreasing supply of class-F flay ash, to reduce the materials cost, and to minimize the carbon emission, we greatly reduced the geopolymer binder content from the regular level (25~30 wt%) to ~14 wt%. About ~1.2 wt% organic additives were used, which improved the rheology/workability during the premixing stage, and strengthened the connections among the filler grains. The compaction pressure was ~70 MPa. The flexural strength of the final material was ~10 MPa, exceeding the performance of regular concrete (2-6 MPa) (Mindess and Young 2002).

1.3 Outline of this thesis

In Chapter 2, we use the CSA technique to develop a sand-filler thermoplastic-binder composite material. Polyethylene (PE) is used to demonstrate the concept. With a ~10wt% binder content, the optimum compressive strength is 70-100 MPa, and the flexural strength is ~15 MPa. It offers a method to upcycle the large amount of waste plastics by producing green concrete.

In Chapter 3, algae-filler artificial timber is fabricated through CSA, with an epoxy binder. With a low binder content of 2-4 wt%, the flexural strength is comparable with that of softwood. This study may provide a solution to upcycle algae, and open a new door to carbon-sink buildings and infrastructures.

In Chapter 4, we perform prove-of-concept tests on inch-sized OPC-based low-binder-content green concrete. Parameterized studies are carried out. The testing results show that the critical factors are the compaction pressure, the OPC content (10-15%), and the water/cement ratio. Other key parameters the sand type, the sand grain size, and the additives.

In Chapter 5, we scale up the OPC-based low-binder-content green concrete from

the inch-sized (~10 grams per sample) to brick-sized (~1 lb. per sample). A compaction system (PS1) is designed and fabricated. Sectioned compaction self-assembly (S-CSA) is the key concept; that is, the relatively large sample is compressed section by section, so that the requirement of the machine capacity and the mold complexity is much reduced.

In Chapter 6, we investigate the advanced binders for the low-binder-content green concrete system. Microfibers (MF), ground quartz (GQ), and viscosity modifying admixture (VMA) are identified as the key components. When the OPC content is 15 wt%, the compressive strength and flexural strength can reach ~80 MPa and ~12 MPa, respectively. The compaction pressure is largely reduced to 15 MPa.

In Chapter 7, we further scale up the S-CSA production of the OPC-based low-binder-content green concrete, from brick-sized (~1 lb per sample) to paver-sized (~20 lb per sample). A relatively large compaction system (PS20) is designed and fabricated.

Eventually, in Chapter 8, through S-CSA, we produce full-size (~500 lbs) samples of OPC-based low-binder-content green concrete. A full-size compaction system (PS500) is designed and fabricated. With a OPC content of 15 wt% and a compaction pressure of 15 MPa, the compressive strength and flexural strength can reach ~100 MPa and ~15 MPa, respectively. The ductility is 1-2 orders of magnitude higher than that of conventional concrete.

In Chapter 9, we summarize our work and discuss future research.

Chapter 2 Compaction self-assembly for polymer cement

2.1 Introduction

As introduced in Chapter 1, in order to save energy and to reduce carbon emission, a major effort is to develop "green cement" – construction materials that can largely replace ordinary portland cement (OPC) (Garg and Jain 2014). Production of OPC demands calcination of mixed limestone, clay, and gypsum at ~1550 ℃ (Garcia-Lodeiro et al. 2015). The mineral decomposition releases more than 800 kg carbon dioxide (CO_2) per ton of manufactured cement (Karthik and Jagannathan 2015), and uses approximately 4 GJ energy (Marceau et al. 2002). Currently, in every ~15 parts of CO_2 generated from human-related activities, 1 part is from OPC manufacturing (Benhelal et al. 2013; Ang and Su 2016; Charoenkit and Yiemwattana 2016; Ji et al. 2017; Kou, Zhong, Kim, et al. 2019). In every 10 parts of industrial energy consumption, ~1 part is associated with OPC processing and transportation (Madlool et al. 2011). Conventional "green cements", such as fly ash modified OPC (Papadakis 1999) and alkali-activated geopolymers (Motorwala et al. 2013), are under extensive study. Another cement-free construction material is polymer cement (Ollitrault-Fichet et al. 1998). It is formed by mixing sand/soil particles and a polymer binder. This process emits almost no CO_2 and consumes little energy. However, conventional mixing relies on shear motion to distribute the binder phase, for which the binder amount needs to be larger than ~15 wt% (Ohama 1995; Abdel-Fattah and El-Hawary 1999). A lower binder content usually results in a much-reduced structural strength. Because the polymer binder is relatively expensive ($1-3 per kg) (Figovsky and Beilin 2013), traditional polymer cements cannot compete against OPC on cost. The applications of polymer cement are limited to small-sized high-end markets, such as waste chemical

storage, water pipes, floor tiles, etc. (Darnell 1991; Do and Soh 2003; Bozkurt and İslamoğlu 2013; Kou, Zhong, and Qiao 2019; Zhong et al. 2019), mainly because of their high strength, high corrosion resistance, and aesthetic features.

Previously, we performed investigation on the compaction self-assembly (CSA) technology to manufacture particulate composites with ultralow binder contents (Chen et al. 2018; Oh et al. 2019; Su et al. 2019; Oh, Chen, Kou, et al. 2020b; Yi et al. 2020b). In CSA, no long-range motion of materials components is involved. Premixed sand/soil and binder is quasi-statically compacted. Resin droplets are squeezed and driven by large capillary forces. Eventually, polymer micro-agglomerations (PMA) are self-assembled among adjacent filler grains. This nonuniform binder distribution maximizes the system efficiency of load transfer. With the binder content as low as 3~4 wt%, it leading to a high flexural strength around 20-40 MPa, stronger than most concrete parts with steel rebars. The compressive strength of the ultralow-binder-content (UBC) composite is 50-60 MPa, on the same scale as high-strength concrete (Caldarone 2014). The polymer binder could be a thermoset, e.g. epoxy. The cost of epoxy is around $2-3 kg (Biron 2013). Processing of thermosets consumes energy and emits about 2-3 kg CO_2 per kg of product (Joosten 2001).

Due to the large size of the construction materials market, it is desirable to have an alternative binder source that does not increase the burden of polymer production. One attractive method is to use recycled waste plastics. In 2013, ~300 million tons of plastics are produced worldwide, which causes tremendous environmental concerns (Gourmelon 2015). Common waste plastics include polyethylene, polystyrene, polypropylene, etc. Fabrication of construction parts is tolerate to the impurities and contaminations,

circumventing the main reason why currently most of the plastics cannot be recycled (Al-Salem et al. 2009). Thermoplastics do not crosslink but would melt upon heating. In this chapter, we investigate polyethylene (PE) as the binder. Once successful, it will offer a promising solution not only to the mitigation of "white pollution"(Blank et al. 2020), but also to the reduction of energy use and carbon emission from the construction industry.

2.2 Experimental procedure

Polyethylene (PE) was obtained from Sigma-Aldrich (SKU 434272), with the particle size around 40–50 μm. All-purpose sand was provided by Quikrete (Product No. 1152), meeting the requirement of ASTM C33/33M. The largest sand grains (> 2 mm) were removed through sieve analysis. The sand was air dried at ambient temperature (~22 °C) for over 24 h. About 3 g of the filler (sand) and the binder (PE) were weighed separately and transferred into a 40-ml beaker, and manually mixed by a steel spatula for 2 min (Figure 2.1A). The binder content ranged from 4% to 30%. The premixed material was poured into a cylindrical steel mold that had been preheated at 200 °C, and placed in a Jeio Tech OF-12G-120 convection oven at 200 °C. The heating time (t_H) ranged from 10 min to 1 h. The outer diameter, the inner diameter, and the height of the steel mold was 50.8 mm, 44.45 mm, and 19.05 mm, respectively. The two ends of the mold were end-capped by two preheated 25.4 mm-long 19.05 mm-diameter steel pistons. The mold was moved out of the oven, and immediately placed on the loading stage of an Instron type-5582 universal testing machine (Figure 2.1B). The upper piston was pushed into the mold, to reach the maximum compaction pressure (P_c). The loading rate was set to 15 mm/min. The value of P_c ranged from 70 MPa to 350 MPa. The peak pressure was maintained for 1 min, after which the compacted material was pushed out of the mold and air-cooled. By

using a high-speed diamond saw (MTI SYJ-40-LD), the produced PE-binder sample was sectioned into 18 mm-long 5 mm-large specimens. A set of 400-grit sandpapers were used to polish the specimen surfaces. The flexural strength was measured through three-point bending (Figure 2.1C). Two 20 mm-long 2 mm-diameter steel pins supported the specimen, with the span between the two pins (L) being ~16 mm. A compression pin was pressed downwards by the Instron machine, at the center of the upper surface. The compression rate was 6 mm/min. The flexural strength was $R = \frac{3}{2}\frac{F_f L}{bd^2}$, where F_f is the peak force at failure, b is the specimen width, and d is the specimen thickness. For each testing condition, at least 3 nominally same specimens were measured. Fractography was analyzed by using a scanning electron microscope (SEM).

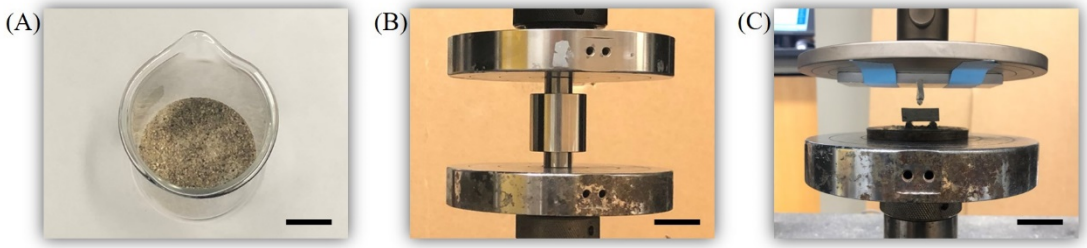

Figure 2.1 Typical photos of (A) premixed filler (sand) grains and binder (PE) powders (scale bar: 10 mm), (B) mixed materials compacted in a steel mold (scale bar: 20 mm), and (C) three point bending test (scale bar: 20 mm)

2.3 Results and discussion

Figure 2.2(A) shows the relationship of the measured flexural strength (R) and the PE content (c). While a lower c tends to improve the cost-performance balance, a larger c helps increase R. When the PE content is 4 wt%, the flexural strength is ~8 MPa, nearly two times stronger than typical concrete (Wood 1992). With 7 wt% PE, R is around 14 MPa, comparable to many steel-reinforced concrete (Leet and Bernal 1982). The strength

rapidly rises to ~23 MPa when c is 10 wt%. As c further increases, its beneficial effect becomes less pronounced. With c = 25 wt%, the optimum strength is achieved around 30 MPa, close to the inherent strength of PE (Billmeyer and Billmeyer 1984), suggesting that the materials system has saturated. An even larger PE content would not further enhance R. However, when the binder content is above 30 wt%, the material is quite ductile. Clearly, as the PE phase fully occupies the free space among the filler grains, it dominates the overall mechanical property.

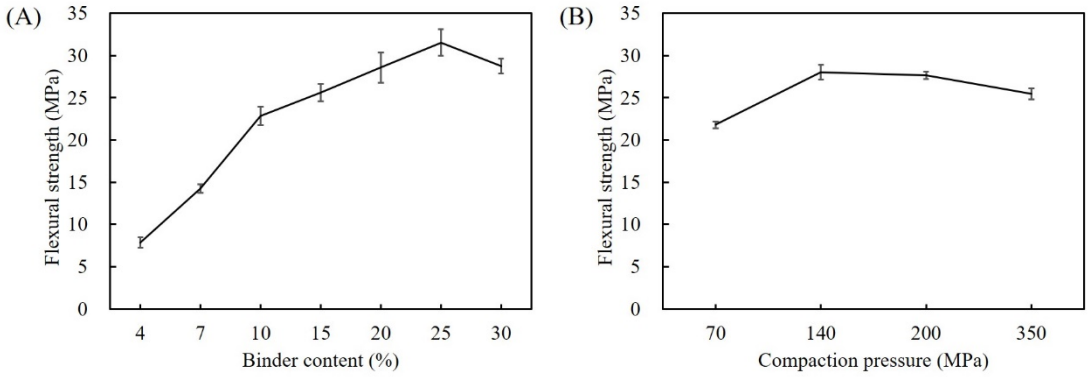

Figure 2.2 The flexural strength as a function of (A) the binder content and (B) the compaction pressure. The heating time is 30 min; the out time is 1 min; the compaction pressure in (A) is 350 MPa; the binder content in (B) is 10 wt%.

The PE is chosen for the current study mainly because of its particle size (40–50 um). It is comparable with but smaller than the sand grain size. Through manual premixing, the PE particles can fit into the interstitial gaps among the sand grains, beneficial for the micro-agglomeration formation. Compared to the PE under investigation, waste plastics contain various impurities and industrial additives, and have a broad molecular weight distribution. These factors may have detrimental effects on the material strength, which will be important topics in our future work.

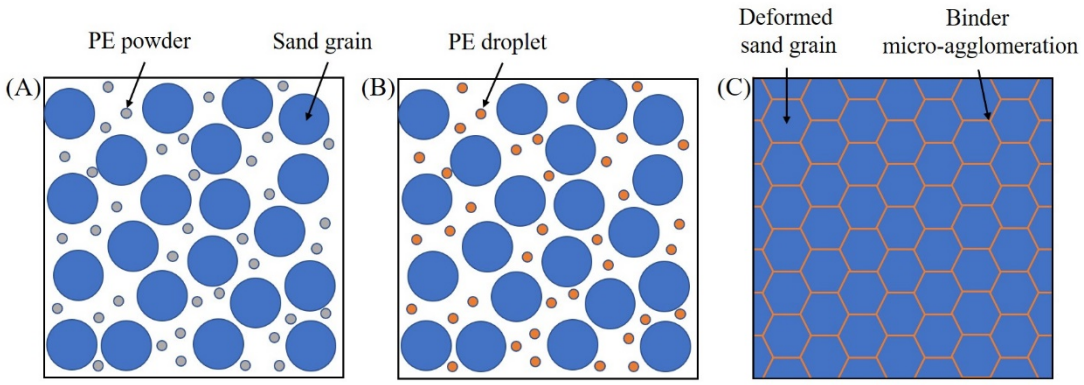

Figure 2.3 Schematics showing (A) mixed sand grains (the filler) and PE powders (the binder); (B) upon heating, PE is melted; (C) upon compaction, the sand grains are deformed and densified, and the PE droplets are self-assembled into binder micro-agglomerations.

Figure 2.2(B) demonstrates the influence of the maximum compaction pressure (P_c). When P_c is less than 140 MPa, increasing it is beneficial. As P_c rises from 70 MPa to 140 MPa, R is improved from ~22 MPa to ~27 MPa by nearly 22%. A larger compaction pressure above 140 MPa does not lead to a stronger material. In general, when the material is premixed (Figure 2.3A) and heated at 200 °C (Figure 2.3B), the sand grains cannot form bonding with each other, because the PE amount is small. The critical step is the CSA operation (Figure 2.3C). As the compaction loading is applied, the sand grains are pressed toward each other, accompanied by grain deformation, sliding, and rotation. As a result, the PE melt spreads over local areas. More critically, when the peak compaction pressure is maintained, a large capillary force presents at the narrowest microstructure sites. The capillary force pulls the PE melt to the contact places of adjacent sand grains, so that the binder is most efficiently utilized to bond the filler together. It explains why the material is much stronger than regular composites of the same binder contents, particularly when c < 10%.

With a higher compaction pressure, the short-range sand movement is promoted

and the capillary force is larger, so that the binder dispersion is more uniform and the final strength is higher. This is demonstrated by the comparison between Figure 2.4(A) and Figure 2.4(B). When c > 20 wt% or P_c > 140 MPa, the PE distribution is quite homogeneous. As R approaches the PE strength, no further improvement can be obtained (Figure 2.4B and Figure 2.4C). To maximize the production yield and to minimize the machinery complexity, the optimum PE content should be 7–10 wt% and the compaction pressure may be 70–100 MPa.

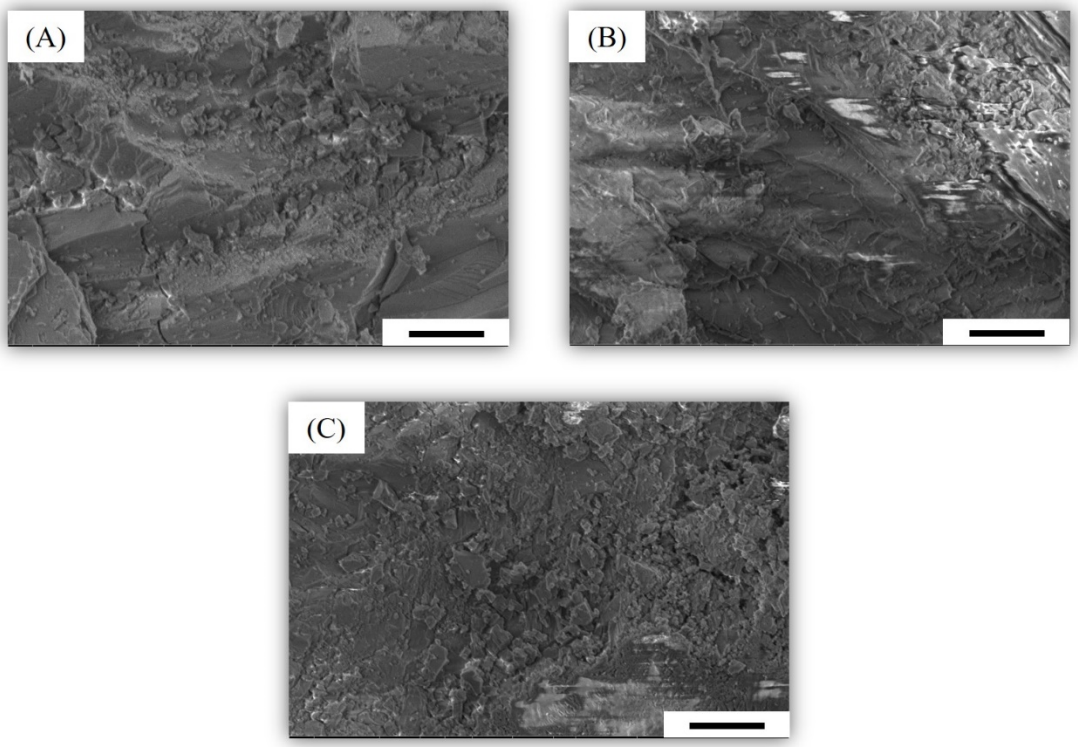

Figure 2.4 SEM images of the PE-binder samples formed at the compaction pressures of (A) 70 MPa, (B) 140 MPa, and (C) 350 MPa (scale bar: 10 μm).

Since sand is not a good heat conductor, melting of PE powders takes time. As shown in Figure 2.5(A), as the heating time (t_H) is increased from 10 min to 30 min, the material strength is considerably improved from ~14 MPa to ~25 MPa by ~80%. We

observed that as t_H became longer, the PE color changed from white to somewhat grayish. If t_H exceeded 30 min, the color turned slightly yellowish and correspondingly, the strength decreased. When t_H was 50–60 min, R was reduced back to ~14 MPa. It should be related to the oxidation and possible thermal decomposition of PE (Billmeyer and Billmeyer 1984). As the long chains are broken apart, the effective molecular weight is smaller, and the PE strength is lowered.

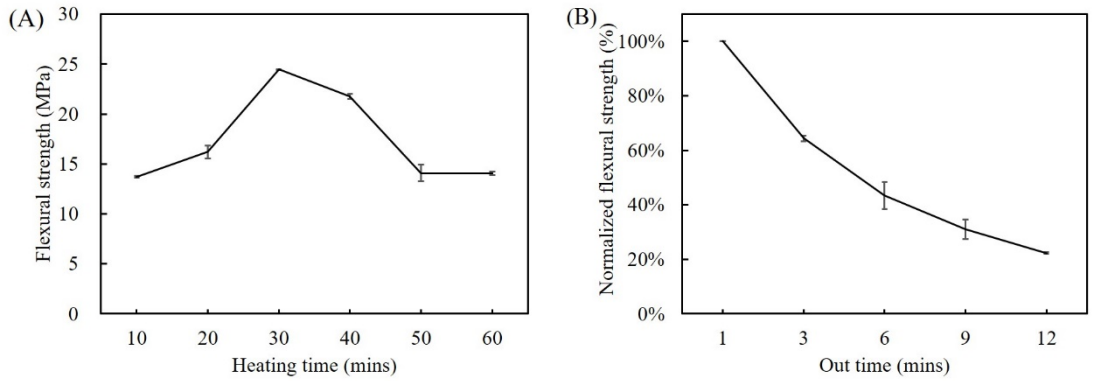

Figure 2.5 The flexural strength as a function of (A) the heating time and (B) the out time. The compaction pressure is 350 MPa; the binder content is 10 wt%; the out time in (A) is 1 min; the heating time in (B) is 30 min.

Another important processing parameter is the out time (t_O), i.e., the duration from the completion of heating to the onset of compaction. Its influence is shown in Figure 2.5(B). As the heating ends and the mold is moved out of the oven, the temperature begins to decrease. While no solidification takes place within a few minutes, the viscosity of the polymer melt rises (Meyer and Keurentjes 2005). The highest strength is achieved when the out time is less than 1 min. When t_O becomes longer, R decreases. As t_O is 3–6 min, R is only 40–60% of the peak strength. When t_O is around 10 min, local solidification can be observed, and the strength largely decreases by ~80%. The effects of the heating time and the out time are mainly determined by the thermal properties of the binder (PE), not directly

associated with the compaction pressure.

We also investigated the effect of the cooling rate. Instead of air cooling, after compaction, the material was immediately taken out of the mold and transferred to a temperature chamber at −5 °C for 1 h, and then rested in ambient air for 12 h. The compaction pressure was 350 MPa; the heating time was 10 min; the out time was 1 min; the PE content was 4 wt%. The fast cooling does not have any evident influence on the flexural strength, indicating that the solidification process is not a critical procedure. The microstructure of the material is formed during the CSA operation, before cooling starts.

In another set of tests, we confined the material during heating. As the mold was moved to the oven, the two pistons were firmly clamped, so that their positions were fixed. The rest of the procedure remained unchanged. The compaction pressure was 350 MPa; the heating time was 30 min; the out time was 1 min; and the PE content was 10 wt%. With the additional confinement, the material strength decreased from ~17 MPa to ~13 MPa by about 25%. This result suggests that free expansion is critical to the preparation of CSA. When PE melts, its volume considerably increases. If the system volume is fixed, the motion of the polymer melt is restricted, and may be forced into the largest vacancies by the internal pressure. Hence, widespread dispersion of the binder phase is difficult.

2.4 Conclusions

In summary, we investigated thermoplastic-binder sand-filler composites. Polyethylene (PE) was employed as the model material for waste plastics. The goal was to produce useful construction materials. After sand and PE powders were premixed, they were heated and then compacted. The compaction was not to form the material into shape, but to quasi-statically disperse the binder to the critical load-carrying microstructural sites.

The material strength increases with the binder content and the compaction pressure. The optimum binder amount is ~10 wt%; the optimum compaction pressure is 70–100 MPa. The so-processed material has a flexural strength around 15 MPa, better than many steel-reinforced concretes. If the heating time is too short or too long, the strength would be reduced. The out time should be as short as possible. Cooling rate does not have an evident influence. Free expansion during heating is beneficial. Because construction materials have a low requirement on the binder purity, this study may enable large-scale recycling of waste plastics, and also help reduce the energy use and carbon emission from the construction industry.

Chapter 2, in full, is a reprint of the material as it appears in Sustainable Materials and Technologies. Haozhe Yi, Kiwon Oh, Rui Kou, and Yu Qiao, 2020. Sand-filler structural material with a low content of polyethylene binder. 25 (2020): e00194. The dissertation author was the primary investigator and first author of the paper.

Chapter 3 Compaction self-assembly for algae-filler composites

3.1 Introduction

A promising method of carbon sequestration is to cultivate algae (Soratana and Landis 2011). Algae is low maintenance and fast growing (Blaas and Kroeze 2014; Bux and Chisti 2016). Compared to trees, algae can absorb carbon dioxide (CO_2) more efficiently by two orders of magnitude (Lee and Pirt 1984; Talbot et al. 1991; Bux and Chisti 2016). If equipped with bioreactor-enabled algae farms, a large city may have a negative overall carbon emission rate (Moreira and Pires 2016).

The major challenges to this concept are related to the large scale of algae production. To achieve a nontrivial impact on the CO_2 amount in the atmosphere, each year billions of tons of algae must be produced (Chi et al. 2014). They should not decompose back to CO_2. Permanent storage can be costly. It involves proper dehydration, transportation, and placement. One attractive approach is to use algae to help meet the increasingly high demand of food security (Duffy et al. 2009). Because algae is not traditionally a main food source, it must be processed to separate proteins and carbohydrates, for which basic research is being carried out (Wijesekara and Kim 2015; Wells et al. 2017). Another area of study is to utilize algae as fuel and biomass (Hossain et al. 2008; Dębowski et al. 2013). The main issues include the relatively high cost and the difficulties in scaling up. The cellulose content in cell walls of algae is in the range from 40% to 70% (Mihranyan 2011), offering an opportunity to fabricate structural parts. Dehydrated algae has been converted to polymers and foams (Rubin et al. 1966; Ragan and Craigie 1976; Fasahati and Liu 2015).

Among all the potential applications, construction materials form a sufficiently

large market. Every year, ~10 billion tons concrete are consumed worldwide (Meyer 2009), responsible to 12~15% of total industrial energy use (Madlool et al. 2011) and 5~8% of total human-related CO_2 emission (Benhelal et al. 2013). In addition, a few billion m^3 wood is used annually (Buchanan and Levine 1999). If algae-based materials can replace a portion of concrete and timber, it not only economically helps algae cultivation, but also reduces the energy use and carbon emission from the conventional construction industry.

Dehydrated algae often exist as non-cohesive powders. To apply it in engineering structures, particulate composites need to be processed. A regular particulate composite contains 70~80% filler particles and 20~30% binder (Harper 2002). The fillers are usually sand, wood chips, carbon black, etc. (Consoli et al. 2004). The binder can be epoxy, unsaturated polyester resin, vinyl ester, phenolics, or a thermoplastic (Pascault et al. 2002). These binders are relatively expensive, and their production emits CO_2 (Pascault et al. 2002; Pascault and Williams 2009; Biron 2013). If we use 30% binder in an algae-filler composite, the cost-performance balance and the overall environmental benefit would be unsatisfactory. It is desirable to largely decrease the binder content to below 5%.

With such an ultralow binder content, ordinary composite processing techniques are no longer relevant. The filler-binder wetting would be poor, and the final defect density would be large. To solve these problems, we recently developed the compaction self-assembly (CSA) technology (Chen et al. 2017; Chen et al. 2018; Kou, Zhong, Kim, et al. 2019; Oh et al. 2019; Su et al. 2019; Zhong et al. 2019; Yi et al. 2020a; Oh, Yi, Kou, et al. 2020a; Oh, Chen, Kou, et al. 2020a; Oh, Yi, Chen, et al. 2020). In CSA, filler and binder are first premixed, and then compacted under a relatively high pressure. The binder content can be only ~4%, and the maximum compaction pressure is generally 30~100 MPa. The

compaction pressure not only squeezes the binder droplets and densify the interstitial gaps, but also deforms and rotates the filler particles. More critically, as the filler particles are close-packed, at the direct contact points, a large capillary pressure would be built up, driving the binder to these most important microstructural sites. As the binder is self-assembled into binder micro-agglomerations (BMA), the load-carrying capacity is optimized.

In this chapter, we investigate how to fabricate ultralow-binder-content (UBC) algae-filler composites. The produced material will be referred to as artificial timber.

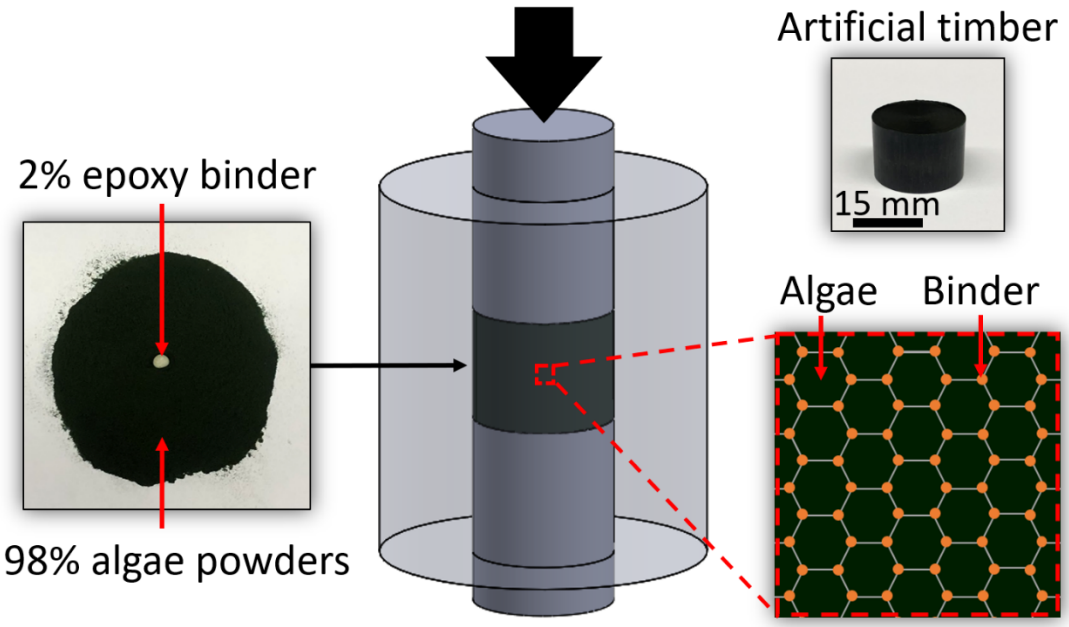

Figure 3.1 The processing procedure of the artificial timber

3.2 Experimental procedure

We investigated two types of algae, denoted by FP and SW, respectively. Algae FP was obtained from Good Natured in powder form (Product No. 857307002257), with the average particle size of 10~15 μm. Algae SW was prepared from zostera marina harvested

at the La Jolla Shore, La Jolla, California. The SW sample was thoroughly rinsed and dried in a mechanical convection oven (Jeio Tech OF-12G-120) at 80 ℃ for 24 hours, chopped by a razor blade into cm-sized pieces, and ground in a MTI MSK-SFM-14 roller mill at 50 rpm for 2 h. The particle size of the milled SW was around 50 μm to 0.5 mm.

Figure 3.1 and Figure 3.2 illustrates the material processing procedure. Epoxy resin (Hexion, Epon 828) was employed as the binder, with the curing agent being Hexion Epikure-3115 polyamide. For each part of epoxy, 1.2 parts curing agent and a certain amount of isopropyl alcohol (IPA) were added, and manually mixed in a glass vial at room temperature (~22 ℃) for 20 min. The IPA to epoxy ratio, $\alpha_{\mathrm{I}} = m_{\mathrm{IPA}}/m_{\mathrm{eh}}$, ranged from 2.5 to 6, where m_{IPA} and m_{eh} are the IPA mass and the epoxy-hardener mixture mass, respectively. Powders of algae filler were blended with the IPA-diluted epoxy in a Thinky ARE-310 centrifugal mixer at 2000 rpm for 3.5 min. The binder content, $\alpha_{\mathrm{b}} = m_{\mathrm{eh}}/(m_{\mathrm{eh}} + m_{\mathrm{a}})$, was in the range from 2% to 10%, where m_{a} is the algae mass.

The material was transferred into a steel cylindrical mold. Two pistons were inserted into the mold from both ends. The height, the outer diameter, and the inner diameter of the mold were 50.7 mm, 44.5 mm, and 19.1 mm, respectively. The height and the diameter of the piston were 25.4 mm and 19.1 mm, respectively. Compaction self-assembly (CSA) was carried out by compressing the algae-binder mixture in a universal testing machine (Instron 5582) at the loading rate of 15 mm/min, until the desired peak pressure (P_{c}) was reached. The loading plate held the peak pressure for 1 min. The peak pressure ranged from 10 MPa to 350 MPa. The two pistons were then fixed by a C-clamp (McMaster-Carr, 5133A19). The mold was placed in the convection oven, and the binder was hardened at 100 ℃ for 1 hour.

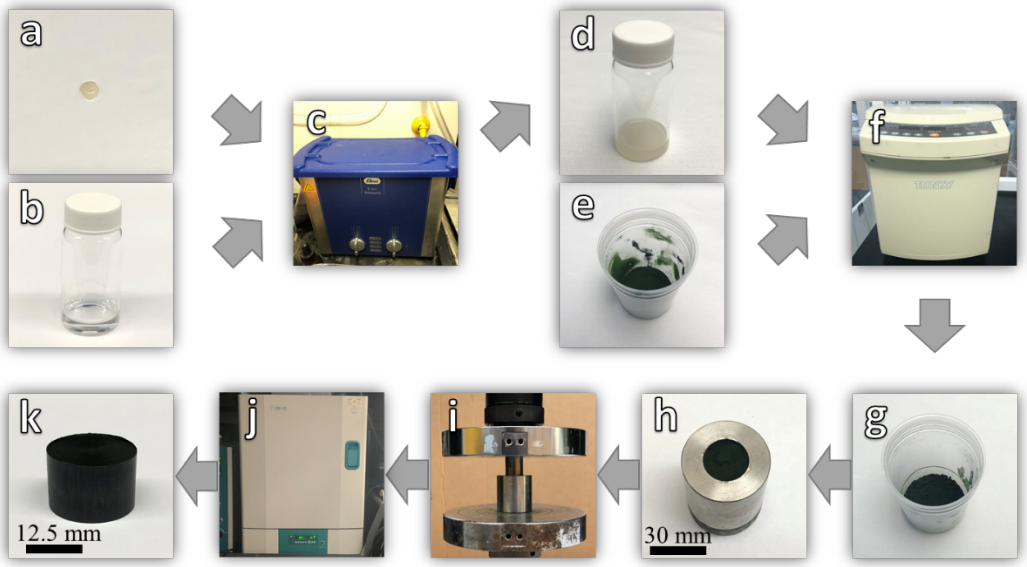

Figure 3.2 The processing procedure: (a) mixed epoxy resin and hardener, (b) IPA, (c) the sonication bath, (d) the IPA-diluted epoxy, (e) the milled algae, (f) the paste mixer, (g) the algae-binder mixture, (h) the steel mold, (i) the CSA setup, (j) curing in a convection oven, and (k) an artificial timber sample.

After curing, the mold was air-cooled for 1 hour, and the artificial timber sample was pushed out by a press. Flexural testing specimens were sectioned by a high-speed diamond saw (MTI, SYJ-40-LD), with the length, depth (d), and width (w) being 18 mm, 5 mm, and 5mm, respectively. The surfaces of the specimen were flattened by 400-grit sandpapers. The flexural strength was measured through three-point bending in the Instron testing machine. The specimen was supported at both ends by two 2.54 mm-diameter 19 mm-long stainless-steel pins. Another steel pin rested at the top of the beam specimen at the middle, and was compressed downwards at the rate of 6 mm/min, until the specimen failed. The peak loading, F_{f}, was recorded. The flexural strength was calculated as $R = \frac{3}{2}\frac{F_{\mathrm{f}}L}{wd^2}$, with $L = 16$ mm being the distance between the two supporting pins. At least three specimens were tested for each condition. Scanning electron microscope (SEM) images were taken at the fracture surfaces.

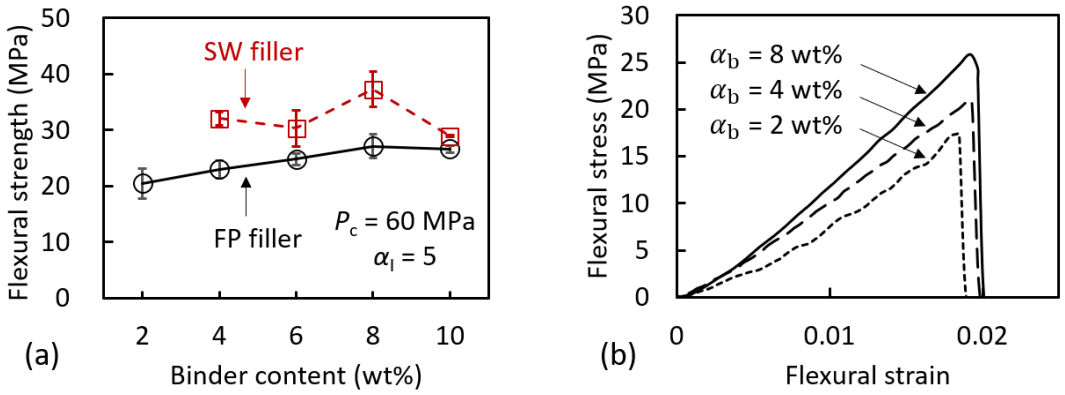

Figure 3.3 (a) The flexural strength (R) as a function of the binder content (α_b). (b) Typical stress-strain curves of FP-filler samples; the IPA to epoxy mass ratio (α_I) is 5, and the compaction pressure (P_c) is 60 MPa.

3.3 Results and discussion

Figure 3.3(a) shows the measured flexural strength of artificial timber samples. The binder content varies from 2% to 10%. Remarkably, with only 2% binder, the strength of the FP-filler samples can reach ~20 MPa, stronger than typical portland cement by more than 5 times and better than most steel-reinforced concrete (Leet and Bernal 1982). As shown in Figure 3.2(k), the compacted material is blackish, having a smooth surface. As the binder content (α_b) increases from 2% to 8%, R is improved somewhat linearly. When $\alpha_b = 8\%$, R is ~27 MPa. When α_I further rises to 10%, the strength remains similar; that is, the binder distribution has saturated. This is consistent with our previous result (Chen et al. 2017) that as the filler is densified, the minimum gap volume is ~8%. Excess binder would be squeezed out of the materials system, and does not contribute to the final structural integrity.

The stress-strain curves in Figure 3.3(b) show that as the binder content increases, both the strength and the stiffness become larger. The increase in strength is more pronounced, so that the failure strain rises with α_b. Because the samples are formed by

small powders, when the final cracking begins, no long fibers could bridge the crack flanks and consequently, the fracture process is abrupt.

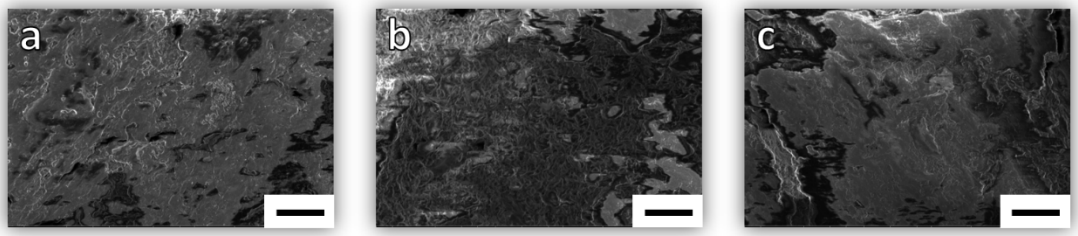

Figure 3.4 Typical SEM images of FP-filler samples, with (a) α_b is 2 wt%, (b) α_b is 6 wt%, and (c) α_b is 10 wt% (scale bar: 10 μm)

The relatively high strength should be attributed to the efficient BMA formation, as well as the filler densification. As shown in Figure 3.4(a), when $\alpha_b = 2\%$, the morphology of the material is already quite homogeneous. Few large-sized defects can be observed. Since algae is deformable upon compaction, during CSA the interstitial sites are largely reduced, and the premixed binder droplets necessarily aggregate into micro-agglomerations at the angular edges of adjacent filler particles. The binder motion is promoted by the capillary pressure, as the CSA pressure greatly decreases the characteristic size of the microstructural channels. As a result, the small amount of binder is dispersed as an efficient load-transferring network, connecting the algae powders into a solid. Such a dense microstructure is maintained in the curing process, as the steel pistons are clamped. If the pistons were free and the material were allowed to expand, the strength of the cured sample would be lowered by 3~4 times. Clearly, before hardening, the binder cannot lock the BMA structure. The thermal mismatch among various components would interrupt the close-packed filler-binder mixture.

When more binder is used, as indicated by Figure 3.4(b), the homogeneity is

improved and the defects formation is suppressed, leading to a higher strength. As the effective porosity is reduced, the modulus of elasticity is larger, causing the observed stiffening effect (Figure 3.3b). When the binder content is 10%, the material is similar to a conventional particulate composite, wherein the binder forms a continuous matrix and the algae powders are fully embedded. This critical value of binder content is 2~3 times less than that of regular composites, thanks to the compaction pressure that deforms, rotates, and compresses the algae phase.

According to Figure 3.3(a), the SW-filler samples generally exhibit a higher strength than the FP-filler samples. Because the SW powder size is considerably larger that of FP, SW tends to have a larger aspect ratio, somewhat similar to microfibers. Thus, in addition to the bonding through BMA, the SW particles may be entangled, further enhancing the structural properties. With only 4% binder, the flexural strength is ~33 MPa, comparable with softwoods (Green et al. 1999). Yet, if the binder content is reduced to 2%, the material would be quite weak and the flexural strength measurement becomes difficult. It is interesting that the flexural strength is not sensitive to the binder content in the range of α_{b} from 4% to 10%. As a considerable portion of strength comes from the internal friction and entanglement of algae, the role of binder is still important, but different from in FP-filler samples. The binder provides distributed locking sites that hold the algae together. As long as the MBA network is relatively complete, the material strength would be optimized.

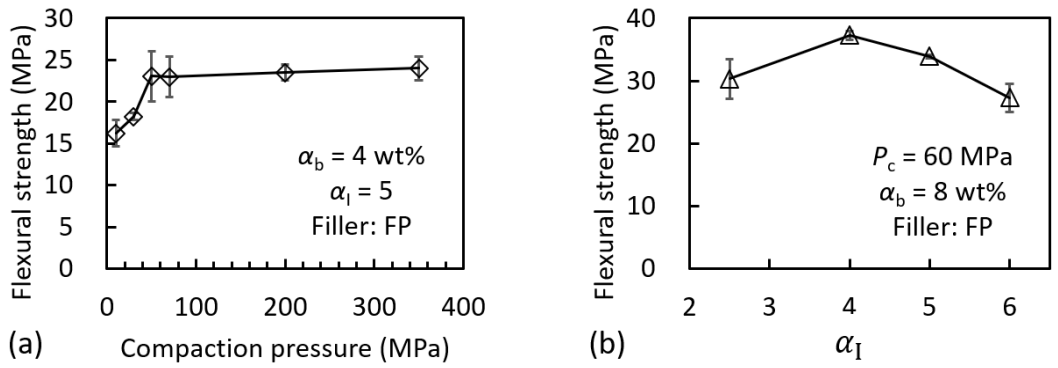

Figure 3.5 The flexural strength (R) as a function of (a) the compaction pressure (P_c) and (b) the IPA to binder mass ratio (α_I)

In addition to the binder content and the filler type, another important processing parameter is the compaction pressure, P_c. As suggested by Figure 3.5(a), in general, a higher compaction pressure is beneficial, especially when it is less than 60 MPa. When $P_c = 10$ MPa, the flexural strength is ~16 MPa. When P_c rises to 60 MPa, the strength increases nearly linearly to ~22 MPa by ~40%. Beyond 60 MPa, the effect of P_c is secondary. When P_c is very high ~350 MPa, R is ~24 MPa, only marginally larger than the strength of $P_c = 60$ MPa. It is clear that the densification effect saturates at ~60 MPa, at which the algae powders have collapsed and the powder rotation and sliding have nearly completed. A compaction pressure around 30~60 MPa is on the same scale as the pressure of compression molding (Suherman et al. 2013; Tatara 2017). To achieve a high strength, the optimum P_c is ~60 MPa.

The IPA to epoxy-hardener ratio (α_I) affects the material structure by changing the rheological properties of the binder. As demonstrated in Figure 3.5(b), when α_I is less than 4, using more IPA helps enhance the strength, since the binder viscosity is reduced and the binder dispersion is more widespread. When α_I exceeds 4, further increasing it would have a detrimental effect, probably because of the increase in defect density, associated with the

volume left by the evaporated IPA. IPA may also interrupt the epoxy ring opening, as the functional groups of polyamide are obstructed. The optimum α_I is ~4, at which the flexural strength reaches ~37 MPa, similar to those of aspen, basswood, sassafras, etc. (Green et al. 1999).

3.4 Conclusions

We produced artificial timber using algae as the filler and epoxy as the binder. The binder content could be only 2~4 wt%, and the flexural strength could be comparable with those of softwoods. The material was quite homogeneous, with a low defect density. The critical processing operation was the compaction self-assembly. Upon a sufficiently high compression pressure, algae powders were deformed, rotated, and densified, and the binder phase was efficiently dispersed. A large filler powder size and aspect ratio helped improve the structural integrity. The optimum compaction pressure was ~60 MPa; further increasing it would not lead to much enhancement in strength. The binder viscosity was critical. It should be controlled by a diluent, e.g., IPA. During curing, the material should be confined, so that the compacted microstructure could remain. This study may provide an important method to upcycle algae, critical not only to the study of algae cultivation and carbon sequestration, but also to the development of next-generation green construction materials.

Chapter 3, in part, is currently being prepared to be submitted for publication. Haozhe Yi, Kiwon Oh, Rui Kou, and Yu Qiao. Algae-based artificial timber with an ultralow binder content. The dissertation author was the primary investigator and first author of the paper.

Chapter 4 Compaction self-assembly for cement-based green concrete

4.1 Introduction

Production of ordinary portland cement (OPC) is a major source of carbon emission (Worrell et al. 2001). Each year, about 2~3 billion tons OPC are consumed worldwide (Karthik and Jagannathan 2015). Mixture of limestones, gypsum, and clay are calcinated at a high temperature ~1550 ºC, releasing ~800 kg carbon dioxide (CO_2) for each ton of OPC (Garcia-Lodeiro et al. 2015), responsible to ~8% human-related CO_2 emission (Ang and Su 2016), second only to the steel industry (Kim and Worrell 2002; Deja et al. 2010). It also uses ~5% of total industrial energy (Madlool et al. 2011).

Over the past a few decades, a number of "green cement" concepts have been actively studied. Increasing the efficiency of OPC plants is an attractive direction (Garg and Jain 2014; Liew et al. 2017). However, because the OPC processing technique has been mature, the improvement tends to be incremental. Using pozzolanic materials to replace a portion of OPC is a common practice (Pacheco-Torgal et al. 2013; Juenger and Siddique 2015), while it affects concrete curing and the benefit has been saturated. Geopolymer may be produced by using an alkali activator to upcycle industrial waste ashes, such as fly ash, furnace slag, etc. (Motorwala et al. 2013). Compared to OPC, geopolymer can be stronger and fast-curing (Hardjito et al. 2004; Singh et al. 2015). However, class F fly ash becomes increasingly unavailable in many areas in the U.S., as the use of coal is rapidly declining (Rangan 2008; Lloyd and Rangan 2010). The relatively large amount of strong alkali imposes challenges to the materials handling as well as the environmental protection (Singh et al. 2015). New methods are still being researched to overcome these hurdles (Sivakrishna et al. 2020). Polymer cement is fabricated by bonding sand and stones

by 10~15 wt.% polyester binder (Ohama 1995; Figovsky and Beilin 2013). It tends to be more durable and stronger than OPC-based concrete, but also much more expensive (Wongpa et al. 2010).

One promising method is to largely reduce the OPC content in concrete (c). Typically, a concrete consists of 25~30% OPC (the binder) and 70~75% aggregates (the filler) (Wilson and Kosmatka 2011). If the OPC amount can be lowered to below 15%, the cement consumption would be much lowered by more than 40%. Another motivation is the materials cost. The aggregate cost is typically ~$20/ton, while the OPC cost is $80~100/ton (Grace et al. 2012; Tedia and Maru 2014). With a smaller OPC content, the concrete can be significantly more cost-efficient.

The major problems of a low OPC content are related to the poor workability and the low strength. When c is less than ~25%, the OPC-aggregate mixture becomes dry, even with a high water-cement ratio. The long-range materials motion becomes jerky and therefore, regular mechanical mixing cannot achieve a uniform binder dispersion. As a result, a relatively large percentage of aggregates remain poorly wetted, leading to a high defect density. As OPC is inherently brittle, damages can easily propagate, and the overall structural integrity is low.

In Chapters 2 and 3, we discussed an advanced processing technology for low-binder-content composites, compaction self-assembly (CSA) (Yi et al. 2020a; Oh, Yi, Kou, et al. 2020a; Oh, Chen, Kou, et al. 2020b). CSA takes advantage of the high capillary pressure at the narrow space in microstructure. As the binder is driven to the contact points of the filler particles, it is efficiently utilized for load-carrying. The densification effect, the local particle sliding and rotation, as well as the “squeezing” effect also help to disperse

the binder. The compaction pressure is often 30~200 MPa. With a binder content as low as 3~4%, the material can be stronger than typical steel-reinforced concrete.

Previously, our work on CSA was focused on organic polymer binders and geopolymer binders. In this chapter, we investigate the OPC binder. As OPC is the dominant material in the present-day construction industry, we envision that the produced materials may have a direct and immediate impact.

4.2 Experimental procedure

All-purpose sand was provided by Quikrete. It was air-dried for more than 24 hours before use. For some tests, the sand grain size was controlled through sieve analysis. Type II/V OPC was provided by CalPortland, stored in a sealed box to keep it from moisture. In most tests, no coarse aggregates (e.g., gravel or crushed limestone) were used, except in Section 4.3.11.

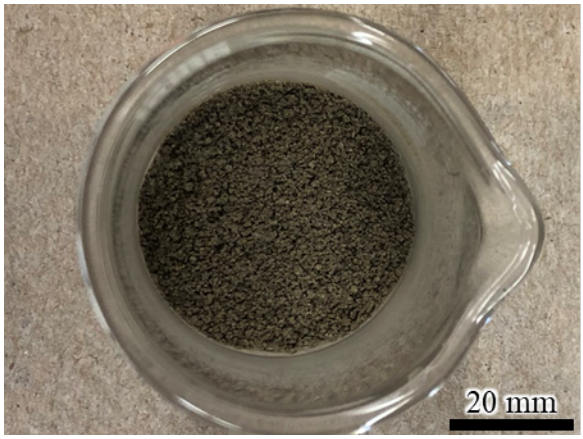

Figure 4.1 Premixed materials

Parameterized studies were performed on small samples. The sample mass was ~10 grams. First, sand and OPC were manually mixed in a glass vial for ~2 mins. Then, water was added and mixed for ~3 mins (Figure 4.1). In some samples, a superplasticizer (SP)

(1% of the OPC mass) and a polymer binder (0.4-0.8% of the sample mass) were used. Three types of superplasticizers were studied: SP1 (from Buddy Rhodes Concrete Products, Product No. 420), SP2 (from Globmarble, Product No. Melflux-2651F), and SP3 (from Buddy Rhodes Concrete Products, Product No. 310). The polymer binder was either an unsaturated polyester resin (UPR) or an epoxy. The UPR was 404 Tooling Polyester Resin-Isophthalic, with 2 wt% methyl ethyl ketone peroxide (MEKP) as the initiator. The epoxy was provided by EPON (Product No. 828), with 35% aliphatic amines (from EPIKURE, Product No. 3230) as the hardener.

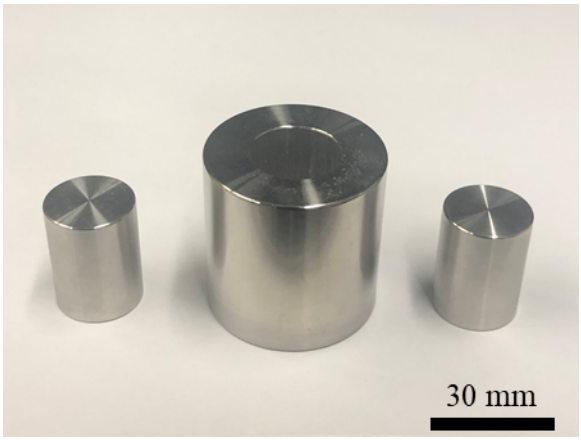

Figure 4.2 A cylindrical steel mold with two pistons

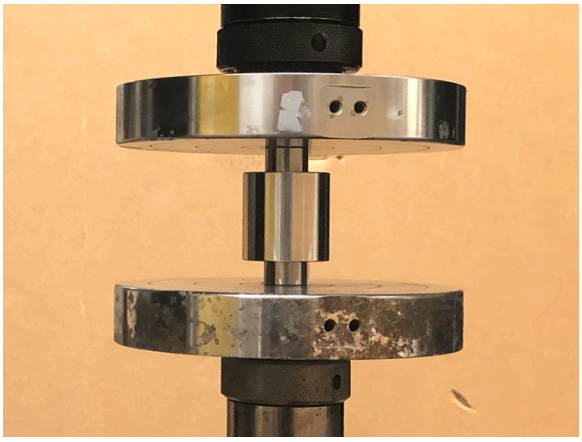

Figure 4.3 Compaction self-assembly (CSA), carried out by the Instron universal testing machine

The mixture was transferred into a cylindrical steel mold (Figure 4.2). The height, the outer diameter, and the inner diameter of the mold were 50.7 mm, 44.5 mm, and 19.1 mm, respectively. Two pistons were inserted from both ends of the cylindrical mold. The height and the diameter of the pistons were 25.4 mm and 19.1 mm, respectively. Compaction self-assembly (CSA) was carried out by a Model 5582 Instron universal testing machine (Figure 4.3). The pre-mixed material was compacted at a loading rate of 15 mm/min, until the desired compaction pressure (P_c) was reached. The peak compaction force was maintained for 1 min, and then released. After compaction, the two pistons were removed. The compacted sample was left in the mold. The mold was sealed in a glass bottle at ~22℃ for curing (Figure 4.4).

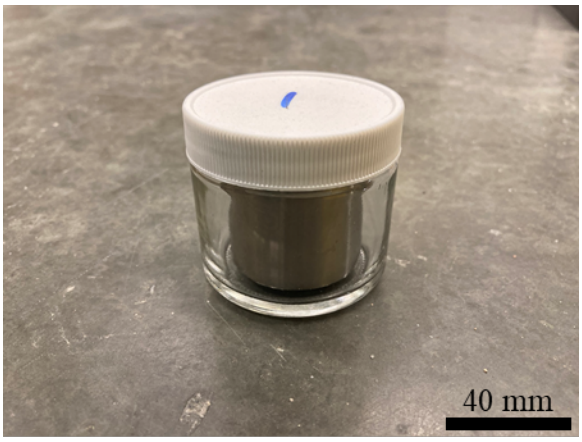

Figure 4.4 Cuing in a sealed glass bottle at ~22℃

For the proof-of-concept study, 3-day compressive strength (σ_c) was measured for most of the samples. They were compressed between the loading stages of the Instron machine at a loading rate of 6 mm/min. The peak loading force (F_c) was recorded. The compressive strength was calculated as $\sigma_c = \frac{F_c}{\pi a^2}$, where a is the diameter of the sample.

4.3 Results and discussion

The key processing parameters include the compaction pressure (P_c), the OPC content (α_c), the water/cement ratio (w/c), the curing time (t_c), the sand grain size (d_s), the sand type, the superplasticizer (SP), and the addition of polymer binder. All the components are measured in weight ratio.

4.3.1 Effect of the compaction operation

The importance of CSA in the production of low-binder-content green concrete is shown in Figure 4.5. When the material is compacted at P_c = 110 MPa, the compressive strength (σ_c) is greater than that of non-compacted reference samples by nearly an order of magnitude. For all the samples, α_c is 10%; w/c varies from 0.3 to 0.6; t_c is 3 days; the sand is the as-received Quikrete material; no SP is used; no UPR or epoxy binder is added. The reference samples are not compacted, with everything else being the same as the compacted samples.

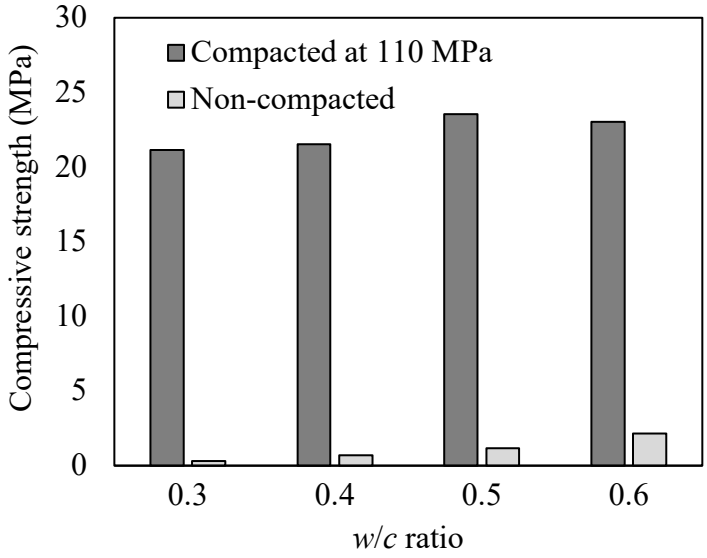

Figure 4.5 Compressive strength (σ_c) of compacted and non-compacted samples

4.3.2 Effect of the compaction pressure (P_c)

The effect of P_c is shown in Figure 4.6. A series of P_c from 10 MPa to 300 MPa are tested. It can be seen that σ_c rapidly increases with P_c, when $P_c < 150$ MPa. When P_c is in the range from 150-300 MPa, its effect on σ_c tends to be saturated. For all the samples, α_c is 10%; *w*/*c* is 0.45 or 0.5; t_c is 3 days; the sand is the as-received Quikrete material; no SP is used; no UPR or epoxy binder is added.

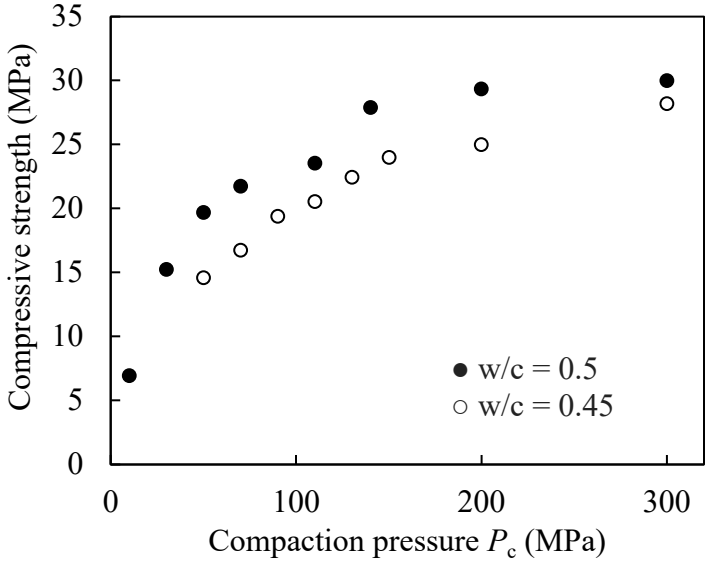

Figure 4.6 Compressive strength (σ_c) as a function of the compaction pressure (P_c)

4.3.3 Effect of the OPC content (α_c)

The effect of α_c is shown in Figure 4.7. For all the samples, P_c is 110 MPa, *w*/*c* varies from 0.25 to 0.45; t_c is 3 days; the sand is the as-received Quikrete material; no SP is used; no UPR or polymer binder is added.

With the same *w*/*c* ratio, it is clear that the compressive strength increases with the OPC amount, as it should. Interestingly, when *w*/*c* rises from 0.25 to 0.45, σ_c keeps increasing for all the α_c under investigation. It may be attributed to the influence of the *w*/*c*

ratio on the rheological behavior of the OPC binder. As less water is used, while the defect density in the OPC phase is inherently lower (Wilson and Kosmatka 2011; Caldarone 2014), the premixed material is drier and the OPC dispersion tends to be less complete. The testing data suggest that the latter effect is dominant.

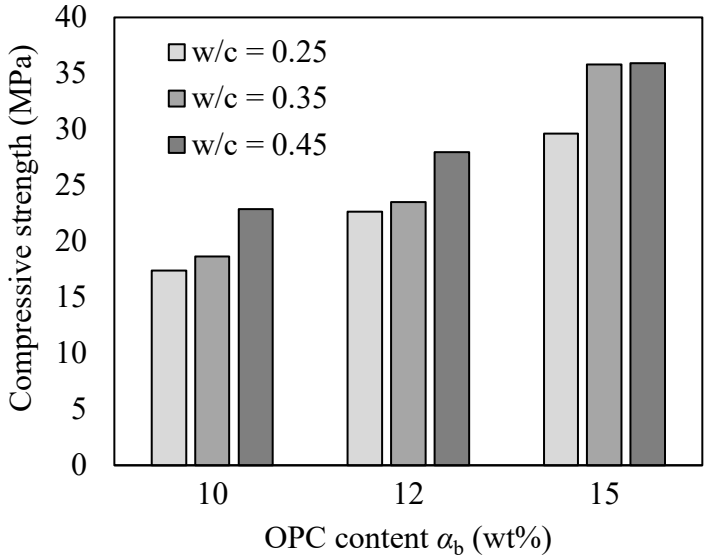

Figure 4.7 Compressive strength (σ_c) as a function of the OPC content (α_c)

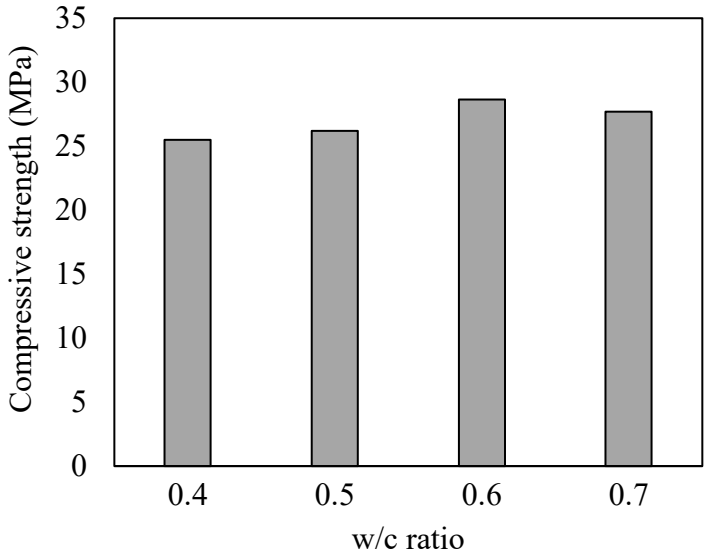

Figure 4.8 Compressive strength (σ_c) as a function of water/cement ratio (w/c)

4.3.4 Effect of the water/cement ratio (w/c)

The effect of w/c is shown in Figures Figure 4.8. For all the samples, P_c is 150 MPa; α_c is 10%; t_c is 3 days; the sand is the as-received Quikrete material; no SP is used; no UPR or epoxy binder is added. When w/c rises from 0.4 to 0.6, σ_c increases by ~10%; when w/c further rises to 0.7, σ_c decreases by ~7%. It should be related to the competition between the inherent defect density in OPC phase and the uniformity of OPC dispersion. A high water/cement ratio helps reduce the former, but suppresses the latter. The experimental result indicates that the optimum range is around 0.5-0.6.

4.3.5 Effect of the curing time (t_c)

The effect of the curing time (t_c) is shown in Figure 4.9. For all the samples, P_c is 110 MPa; α_c is 10%; w/c is 0.45; the sand is the as-received Quikrete material; no SP is used; no UPR or epoxy binder is added. Once curing begins, the compressive strength is measured after 3 days, 7 days, 28 days, and 60 days. It can be seen that σ_c increases by ~30% as t_c extends from 7 days to 28 days. Compared to the 28-day data, the 60-day strength is slightly higher by ~4%.

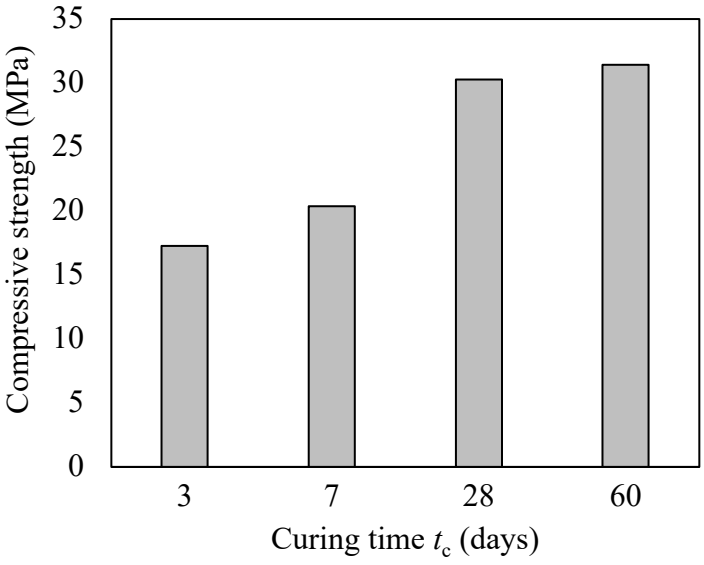

Figure 4.9 Compressive strength (σ_c) as a function of the curing time (t_c)

4.3.6 Effect of the curing mode

For all the samples, P_c = 110 MPa; α_c = 10%; w/c = 0.35; t_c = 3 days; the sand is the as-received Quikrete material; no SP is used; no UPR or epoxy binder is added. After compaction, one group of specimens are cured in the mold for 3 days, following the moisture curing described in Section 4.2; the other group are kept in the mold for 1 day, followed by moisture curing for 2 days. The compressive strength of the second group is reduced by ~7%, compared with that of the first group (Figure 4.10). That is, a longer in-mold curing time is beneficial to the strength development. However, the improvement is somewhat incremental.

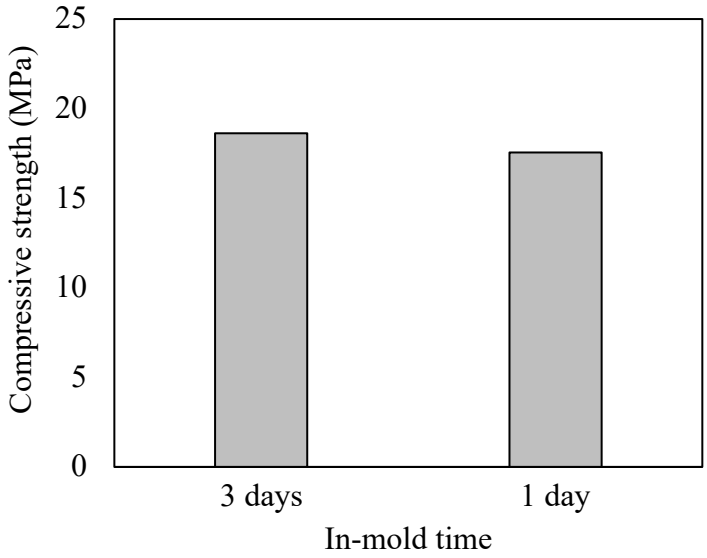

Figure 4.10 Effect of the curing mode

4.3.7 Effect of the sand grain size (d_s)

The grain size (d_s) of the as-received Quikrete sand ranges from ~ 0.5 mm to ~2 mm. Through sieve analysis, it is separated as the fine sand (d_s < 1 mm) and the coarse sand (d_s > 1 mm). For all the samples, P_c is 150 MPa; α_c is 10%; w/c is 0.5; t_c is 3 days; no SP is used; no UPR or epoxy binder is added.

As shown in Figure 4.11, the fine sand leads to the highest σ_c ~28 MPa; the strength of the samples based on as-received sand is slightly lower, ~26.5 MPa; σ_c of the samples made of the coarse sand is only ~14.5%. Clear, the presence of fine sand is critical to the dispersion of the OPC binder.

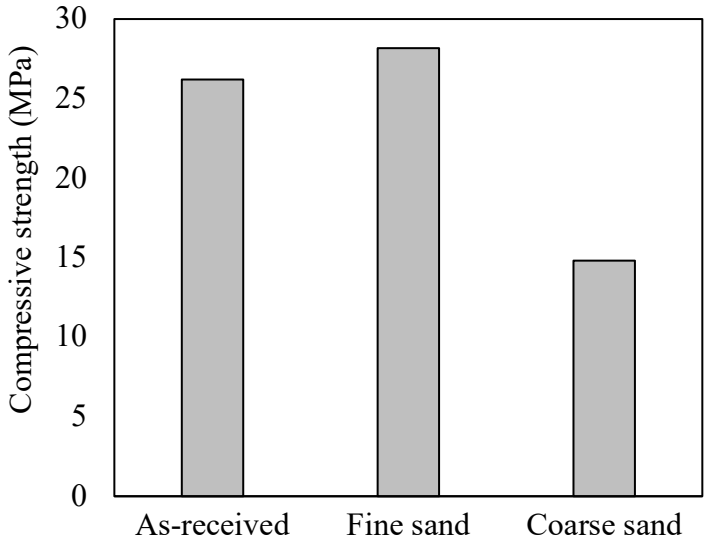

Figure 4.11 Effect of the sand grain size

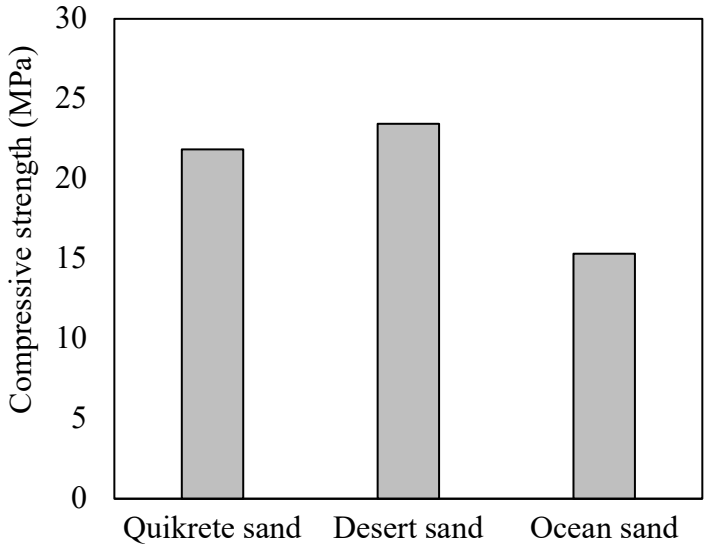

Figure 4.12 Effect of the sand type

4.3.8 Effect of the sand types

The effect of sand type is shown in Figure 4.12. Quikrete all-purpose sand is harvested from a river. The desert sand was gathered from the roadside of CA 111, close to Palm Desert, CA. The ocean sand was collected from the La Jolla Beach, La Jolla, CA.

For all the samples, P_c = 110 MPa; α_c = 10%; w/c = 0.45; t_c = 3 days; no SP is used; no UPR or epoxy binder is added. The desert sand leads to the highest strength, probably due to the high content of the fine grains. The ocean sand leads to the lowest strength, probably due to the high defect density.

4.3.9 Effect of addition of UPR binder

The effect of addition of unsaturated polyester resin (UPR) is shown in Figure 4.13. About 0.8% of UPR was added into the premixed sand-OPC material before compaction. For all the samples, P_c = 110 MPa; α_c = 10%; w/c ranges from 0.25 to 0.45; t_c = 3 days; the sand is the as-received Quikrete material; SP1 (1% of the OPC mass) is added. According to the testing results, UPR hurts σ_c by 35-50%.

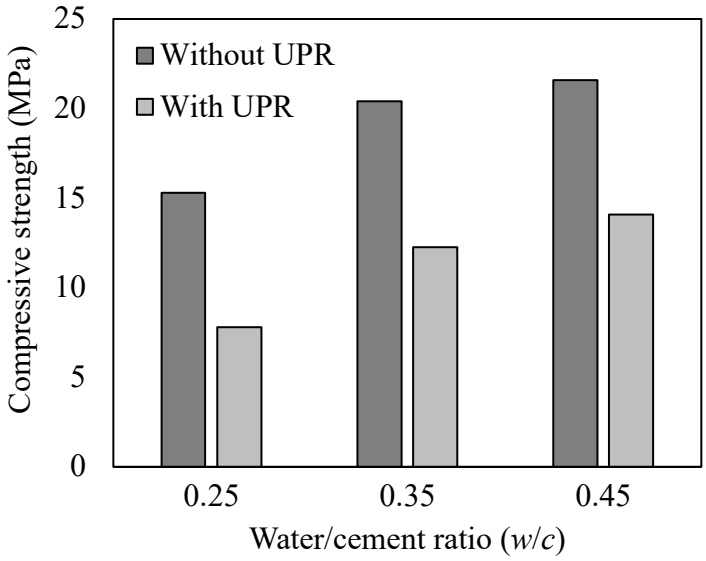

Figure 4.13 Effect of addition of the UPR binder

4.3.10 Effect of addition of epoxy binder

The effect of addition of epoxy is shown in Figure 4.14. The amount of epoxy

additives is either 0.4% or 0.8% of the sample weight. For all the samples, P_c =110 MPa; α_c = 10%; w/c = 0.35; t_c = 7 days; SP2 (1% of the OPC mass) is added. According to the testing results, σ_c increases by ~1% with 0.4% epoxy, and ~9% with 0.8% epoxy.

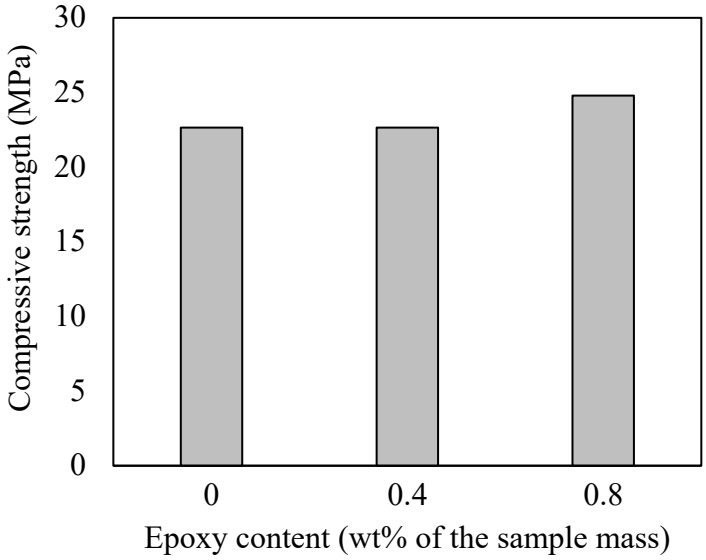

Figure 4.14 Effect of addition of epoxy binder

4.3.11 Effect of SP

The effect of superplasticizer (SP) was examined by testing relatively large samples. The sample mass was ~725 grams; gravel was used as the coarse aggregate. The contents of OPC, sand, and gravel were 19.6%, 34.9%, and 35.4%, respectively. The dry materials were manually mixed for 2 mins, and then water was added and the mixing continued for another 5 mins until the mixture was uniform. The pre-mixed materials were casted in 2 × 4 inches plastic concrete cylinders and sealed for room temperature (~22℃) curing. Three types of superplasticizers (SP1, SP2, and SP3) were analyzed. The dosage for all SPs was 1% of the OPC mass. For all the samples, the w/c ratio was 0.52; t_c was 28 days; no compaction was performed; the sand was the as-received Quikrete material.

As can be seen in Figure 4.15, addition of SP would benefit the compressive strength. Among the three superplasticizers, SP2 is most efficient. The effect of the UPR additives is consistent with the result in Section 4.3.9. It weakens the material, probably due to the interruption of the OPC hardening process.

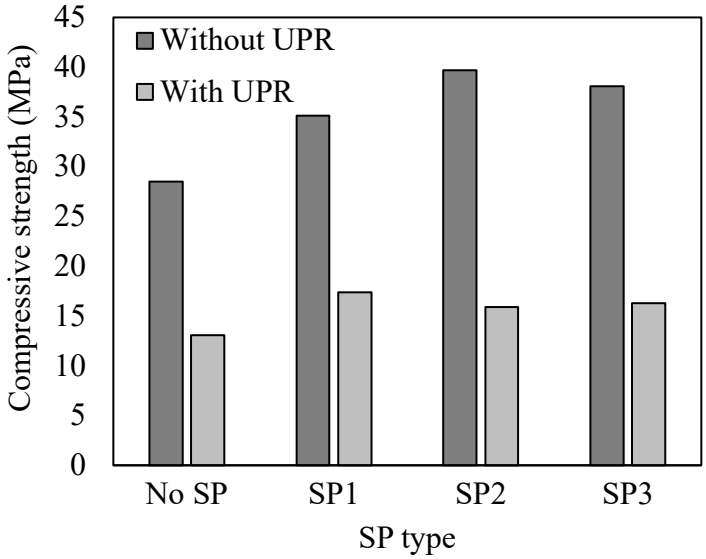

Figure 4.15 Effect of three types of superplasticizer

4.4 Conclusions

To summarize, we performed a parameterized study on OPC-based low-binder-content green concrete. The key parameters included the compaction pressure (P_c), the OPC content (α_c), the water/cement ratio (w/c), the curing time (t_c), the average size of sand grains (d_s), the sand type, the polymer additives, and the superplasticizer. According to the testing results, a higher compaction pressure helps to increase the compressive strength (σ_c), while this effect is saturated when P_c > 150 MPa. When α_c is changed from 10% to 15%, σ_c increases by 50-95%. The highest σ_c is achieved when w/c is 0.5~0.6. Consistent with regular concrete, most of the strength development occurs in the first 28 days of curing.

The sample made of fine sand (d_s < 1mm) has a higher σ_c compared to the samples made of as-received sand; coarse sand (d_s > 1mm) has a detrimental effect on σ_c. In terms of the final strength, desert sand is better than river sand; ocean sand results in a much lower σ_c. Addition of UPR considerably reduces σ_c; addition of epoxy has a mild beneficial effect. In general, SP helps to increase σ_c.

Chapter 4, in part, is currently being prepared to be submitted for publication. Haozhe Yi, Kiwon Oh, Rui Kou, and Yu Qiao. The dissertation author was the primary investigator and first author of the paper.

Chapter 5 Brick-sized low-binder-content green concrete

5.1 Introduction

As discussed in Chapter 4, to minimize carbon emission, to save energy, to lower the materials and transportation costs, and to enhance the construction efficiency, it is imperative to reduce the use of ordinary portland cement (OPC) in concrete (Mahasenan et al. 2003; Deja et al. 2010). The annual production of OPC is around 90 million tons in the U.S., and 2~4 billion tons worldwide (Association 2018). As one ton OPC is manufactured and transported, nearly 1 ton carbon dioxide would be released to the atmosphere (Karthik and Jagannathan 2015), and about 4 GJ energy would be consumed (Marceau et al. 2002). OPC manufacturing is responsible to 5~8% total human-related carbon emission and industrial energy use (Madlool et al. 2011; Benhelal et al. 2013).

In a regular concrete, OPC is used as the binder. The filler consists of the fine aggregates, e.g., sand, and the coarse aggregates, e.g., crushed stones or river gravels (MacGregor et al. 1997). The aggregates improve the stiffness and more importantly, occupy space, so that the binder content (c) can be decreased. With an appropriate aggregate size gradation, the OPC usage is typically 25~30% (Leet and Bernal 1982; Wilson and Kosmatka 2011). If c is lower than this level, the workability tends to be low and upon hydration, there would not be sufficient calcium silicate hydrate (C-S-H) to form a continuous matrix.

Over the years, extensive research was conducted on green concretes. For instance, cementitious materials, such as fly ash and furnace slags, may replace a portion of OPC (Kisku et al. 2017; Xu and Shi 2018). The concrete strength remained similar or is slightly higher, yet the hydration procedure might be affected. Usually, the replaced OPC does not

exceed 25%. For another example, the cement production process may be optimized, to reduce the carbon emission and the energy consumption (Gao et al. 2016). While these techniques are important to the environmental preservation and sustainability, it is desirable to develop a general-purpose approach to minimize the binder content in concrete parts.

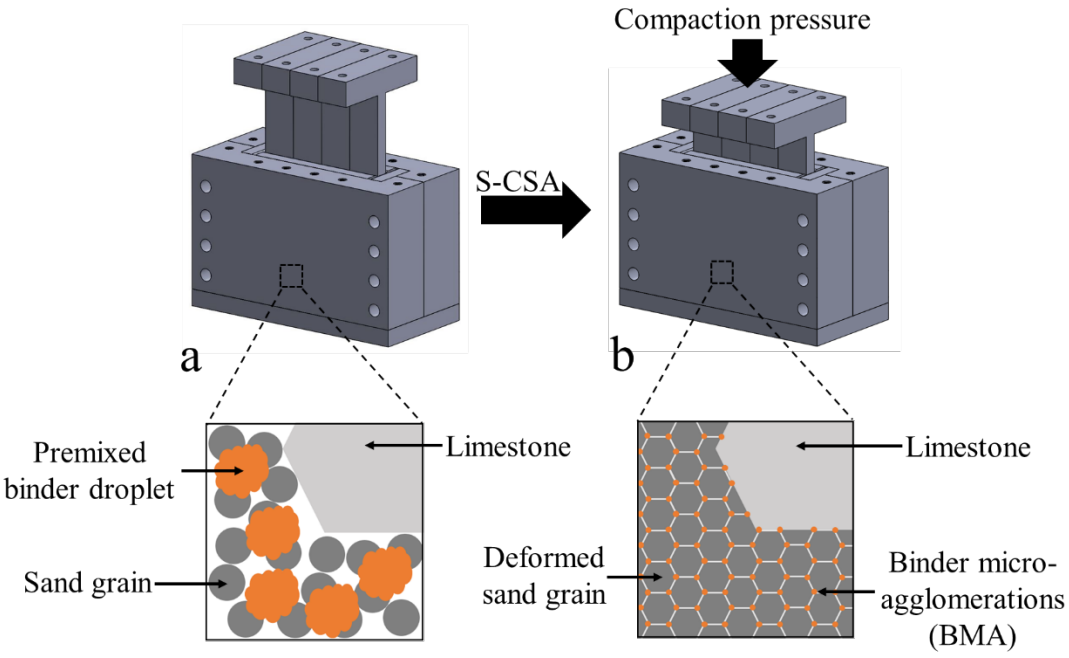

Figure 5.1 Schematic of the S-CSA process

Recently, we performed a series of studies on the compaction self-assembly (CSA) technique for low-binder-content composites (Chen et al. 2018; Oh et al. 2019; Su et al. 2019; Yi et al. 2020a; Oh, Yi, Kou, et al. 2020a; Oh, Yi, Kou, et al. 2020b; Oh, Chen, Kou, et al. 2020a; Oh, Yi, Chen, et al. 2020). In CSA, a relatively small amount of binder is first premixed with the filler, and then compacted in a mold. The binder can be a polymer resin, geopolymer, or OPC. The binder content is 4~15 wt%. The compaction pressure ranges from 30~200 MPa. As depicted in Figure 5.1 (a), after premixing, because the system does

not have enough binder to wet all the filler surfaces, the binder would form small droplets, dispersed among the filler particles. If the material is directly cured in this state, a significant part of filler would not be well bonded, and the sample may disintegrate spontaneously. As shown in Figure 5.1 (b), upon appropriate compaction, the binder droplets can self-assemble into binder micro-agglomerations (BMA), connecting the filler particles into a strong monolith. The driving forces of the BMA formation include the squeezing effect, the sliding and rotation of the filler particles, and probably most importantly, the capillary effect. Since the binder is typically wettable to the filler, once the filler is compressed toward each other, there is a large capillary pressure gradient toward the narrowest gaps, where the particles are in contact. These sites are most critical to the internal load transfer. As they are secured by the MBA, a relatively high strength can be reached with a low c, as the system redundancy is minimized.

As shown in Chapter 4, the preliminary results of the CSA processing of OPC-binder materials are encouraging. The 28-day compressive strength reaches ~30 MPa when the OPC amount is only 10 wt%; the flexural strength is 7~9 MPa, greater than that of typical OPC concretes (2~6 MPa). However, the previous work was focused on the proof-of-concept tests on inch-sized specimens. In order to obtain testing data directly relevant to the construction industry, the samples should be at least brick-sized.

One challenge to production of larger samples is the processing cost. If the CSA operation is completed in one step, the compression capacity of the compaction system must be high. It raises the complexity of the machinery and the mold. One way to circumvent this issue is to perform the compaction section by section, as discussed below.

5.2 Compaction system design

Figure 5.2 shows the sectioned compaction self-assembly (S-CSA) system, which was adaptive to wide ranges of compaction pressure and sample geometry. It contained two U-shaped outer walls, two large inner walls, two small inner walls, four compression pistons, a bottom plate, and two securing bars. All the parts were made from A36 low-carbon steel.

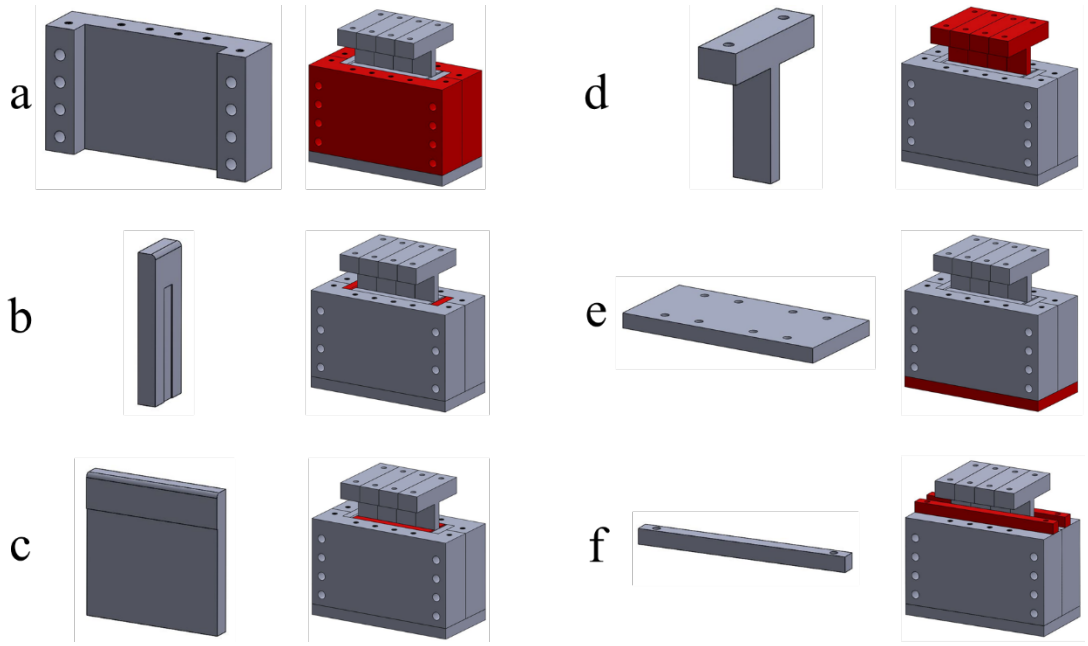

Figure 5.2 Components of the compaction system: (a) U-shaped outer walls, (b) small inner walls, (c) large inner walls, (d) T-shaped compression pistons, (e) bottom plate, and (f) securing bars

Each U-shaped outer wall was 203.2 mm high, 355.6 mm wide, and 50.8 mm thick. The two ends were 35 mm higher than the channel section (Figure 5.2a). The outer walls were the main load-carrying components. They were bolted together by two sets of 3/4-10 grade 8 threaded rods and nuts. In between the outer walls, two 203.2 mm-high, 69.9 mm-wide, 25.4 mm-thick small inner walls (Figure 5.2b) and two 203.2 mm-high, 203.2 mm-

wide, 25.4 mm-thick large inner walls (Figure 5.2c) were inserted, to form a rectangular chamber. There was a 1.5 mm-deep gap at the surface of each inner wall, to reduce the friction.

Through four T-shaped compression pistons (Figure 5.2d), the compaction could be conducted stepwise. One or multiple pistons might be compressed at a time. Each piston consisted of a 171.5 mm-long, 50.8 mm-wide, 38.1 mm-thick horizontal loading head and a 177.8 mm-long, 50.8 mm-wide, 19.1 mm-thick body. A 6.4 mm fillet was placed at the top inner edge of each inner wall, to facilitate the smooth movement of the pistons.

At the bottom of the chamber, a 355.6 mm-long, 152.4 mm-wide, 25.4 mm-thick bottom plate (Figure 5.2e) was attached to the U-shaped outer walls by eight 1/2-13 grade 8 socket head screws. Two 355.6 mm-long, 25.4 mm-wide, 25.4 mm-thick securing bars (Figure 5.2f) could be bolted on the top surface of the U-shaped outer walls, to affix the inner walls, especially when P_c was above 100 MPa.

5.3 Experimental procedure

All-purpose sand from Quikrete and crushed limestone from Greensmith Landscaping were air-dried for 24 hours before use. Type II/V OPC was provided by CalPortland, stored in a sealed box. Melflux-2651F superplasticizer was obtained from Globmarble. Figure 5.3 shows the experimental procedure. S-CSA was carried out by a Model 5582 Instron universal testing machine. The compaction box was assembled on the compression stage.

With a KitchenAid professional 600 stand mixer, 43.2 grams of OPC, 216.2 grams of sand, 173 grams of limestone, and 0.432 grams of superplasticizer were mixed at the Low speed for 5 mins. Then, 21.6 grams of water was added and mixed for 3 mins at the

Medium speed. If needed, the material could be manually stirred for another 1-2 min.

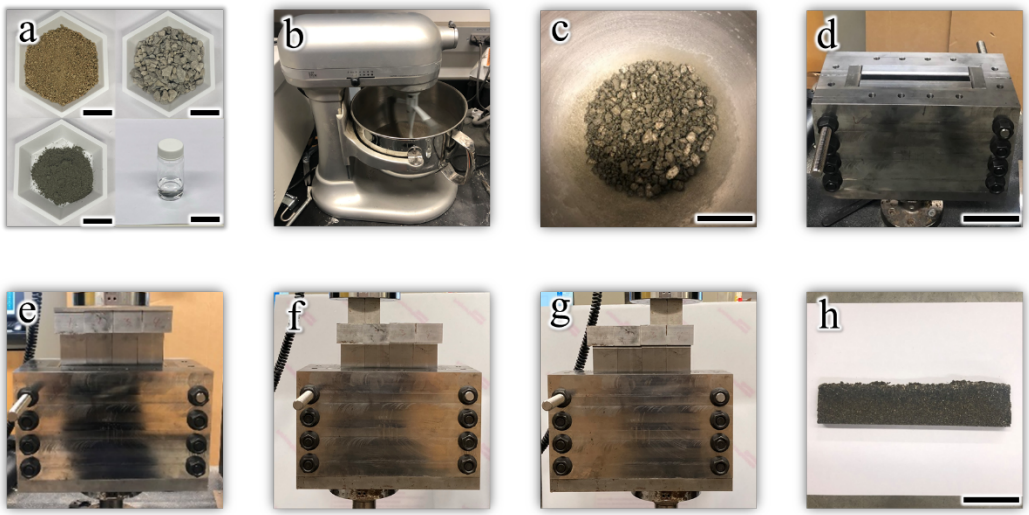

Figure 5.3 (a) Raw materials (sand, limestone, OPC, water) (scale bar: 30 mm); (b) premixing; (c) premixed materials (scale bar: 80 mm); (d) the compaction system (scale bar: 90 mm); (e) the initial compaction; (f) the 1st sectioned compaction; (g) the 2nd sectioned compaction; (h) a cured sample (scale bar: 60 mm)

The premixed material was separated into three equal parts and poured into the compaction box. Manual densification and flattening were performed during the pouring process. A thin layer of WD-40 lubricant was applied on the surfaces of the compression pistons. The four pistons were inserted into the top of the compaction box.

A 100-kN Instron loadcell was installed and calibrated. The initial compaction was conducted by compressing the four pistons simultaneously to 96.78 kN, at the loading rate of 15 mm/min. The average P_c was 25 MPa. The pressure was kept for 60 sec. Then, a 100 mm-long, 50 mm-wide, 50 mm-high steel extension block was placed on top of the first and the second pistons, and compressed to 96.78 kN at the loading rate of 15 mm/min. The associated P_c was 50 MPa. After maintaining the pressure for 1 min, the force was released. Following the same procedure, the other two pistons were also compressed at 50 MPa.

After the S-CSA process, the compacted material was kept in the compaction box for 1 day at ambient temperature (~22 °C), and transferred into a plastic box for moist curing for 27 days. Wet paper towels were used to cover the sample.

Five nominally same samples were produced. The samples were ~203 mm long, ~23 mm wide, and ~51 mm high. Compressive strength and flexural strength tests were performed on the harvested specimens, when the curing time was 3 days, 7 days, 14 days, or 28 days. The compression strength measurement specimens were cubic, with the specimen size (a) around 23 mm. The flexural strength measurement specimens were prismatic, with the length, width (b), and height (d) being 23 mm, 8 mm, and 8 mm, respectively. The cubic specimen was end-capped by USG hydro-stone. It was centered between two loading plates of the Instron machine, and compressed at the loading rate of 6 kN/min until failure. The peak compression force (F_c) was recorded. The compressive strength was calculated as $\sigma_c = \frac{F_c}{a^2}$. The prismatic specimen was tested through three-point bending. It was simply supported by two steel pins. The diameter of the steel pins was 2 mm, and the center-to-center distance (L) was about 16 mm. A third steel pin compressed the specimens at the top surface at the center point, with the loading rate of 6 kN/min until failure. The peak failure force (F_f) was recorded, and the flexural strength was calculated as $\sigma_f = \frac{3LF_f}{2bd^2}$.

5.4 Results and discussion

When the curing time was 3 days, 7 days, or 14 days, for each parameter setting, 5 specimens were tested, and the average strength was obtained. When the curing time was 28 days, for each parameter setting, 15 specimens were tested, and the average strength

was obtained. As shown in Figure 5.4 and Figure 5.5, the average 28-day compressive and flexural strengths of the five brick-sized samples were 39.14 ± 2.57 MPa and 8.13 ± 0.69 MPa, respectively.

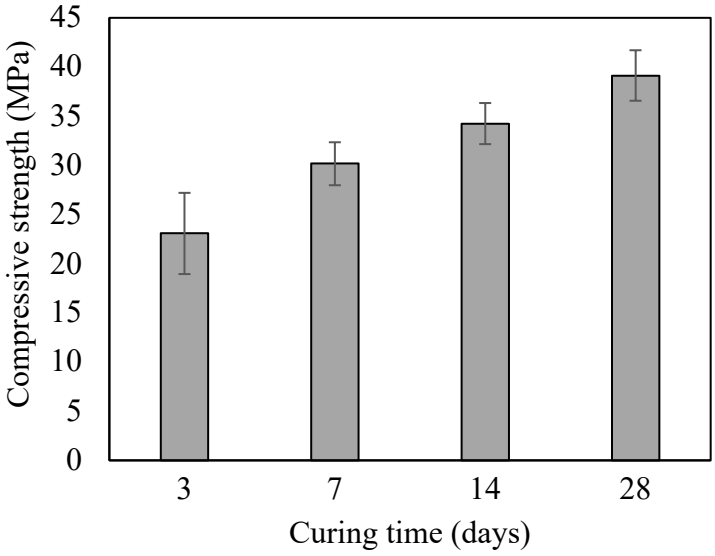

Figure 5.4 Compressive strength as a function of the curing time

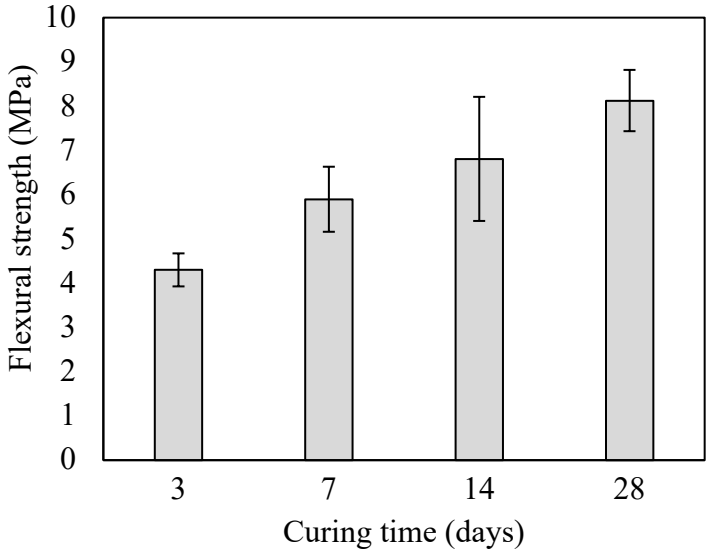

Figure 5.5 Flexural strength as a function of the curing time

The cubic and the prismatic specimens are harvested from various locations from

the brick-sized samples. There is no statistically significant difference in their strengths or stress-strain curves. That is, S-CSA leads to relatively uniform material properties. The evolution of the compressive and the flexural strengths is typical for OPC (Ho et al. 1989; Balayssac et al. 1995; Kim et al. 1998), suggesting that the compaction operation has little influence on the hydration reactions.

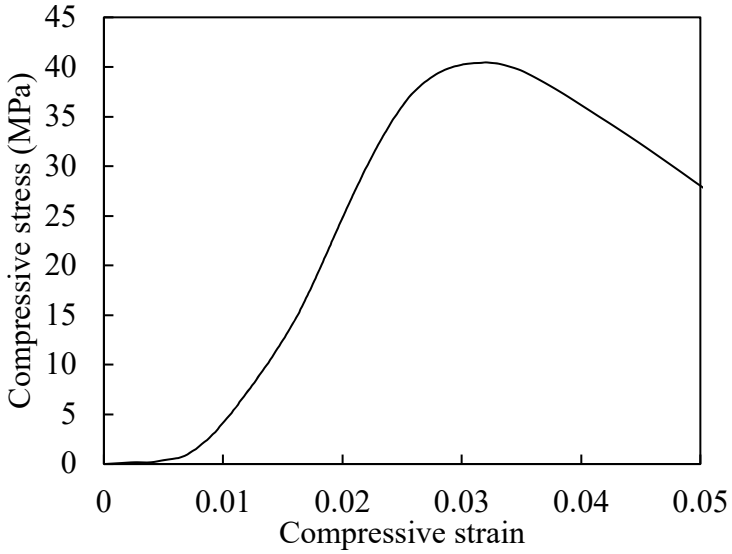

Figure 5.6 Typical compressive strength testing curve

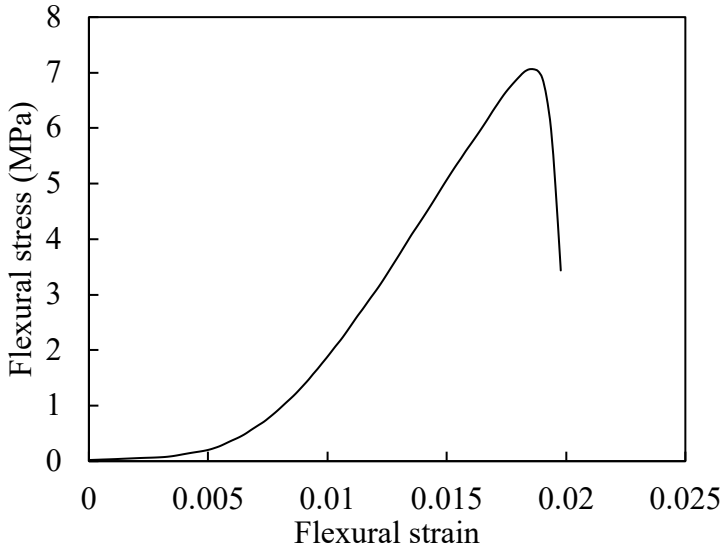

Figure 5.7 Typical flexural strength testing curve

The compressive strength of OPC is usually in the range from 25~50 MPa (Bloem 1968; Mirza et al. 1979; Wilson and Kosmatka 2011), compared to which the 28-day compressive strength of our samples (~39 MPa) is above average. The flexural strength of unreinforced concretes is often 2~6 MPa (Mirza et al. 1979; Mehta 1986; Popovics 1998; Wilson and Kosmatka 2011); the flexural strength of steel-reinforced concretes is often 10~15 MPa (Park and Paulay 1975; Ahmad and Lue 1987; MacGregor et al. 1997). The 28-day flexural strength of our samples is ~8 MPa, between the ranges of unreinforced and steel-reinforced concretes. Overall, while the OPC content in the current study is nearly halved from the typical level, the strength is not detrimentally affected. It should be attributed to the compaction-driven binder micro-agglomeration (BMA) formation. As depicted in Figure 5.1 and Figure 5.2, the relatively large compaction pressure promotes the rotation and shearing of the filler particles, densifies the interstitial gaps, and generates a large local capillary pressure to optimize the BMA distribution. As the OPC binder is best utilized at the most critical internal load transfer sites, a relatively high strength (σ_f and σ_c) is achieved. The pressure may also help enhance the stoichiometry of the hydration reactions, especially for the volume-shrinking processes in the early stage. Moreover, during compaction, redundant water is removed from the system, so that the effective water-cement ratio is lowered.

The stress-strain curves are shown in Figure 5.6 and Figure 5.7. The flexural stress-strain curve in Figure 5.7 is similar to those of regular OPC concretes, while the compressive curve in Figure 5.6 exhibits certain ductile characteristics. The post-peak tail is longer and higher than typical OPC (Barnard 1964; Popovics 1973; Dacheng and Ruqi 1982). It may be associated with the dense microstructure, as shown in Figure 5.8 and

Figure 5.9. The compaction is conducted during the dormant period, which presses the sand particles closely toward each other. This effect lasts even after the pressure is removed, as the material is confined in the compaction box. The material is removed after 1 day, when the surfaces of the OPC grains have been hydrated and the C-S-H phase begins to interlock. Therefore, the porosity is evidently reduced (Figures 5.8 and 5.9). As the defect size and the defect number are decreased, the crack initiation and propagation are suppressed, so that the final failure occurs more slowly.

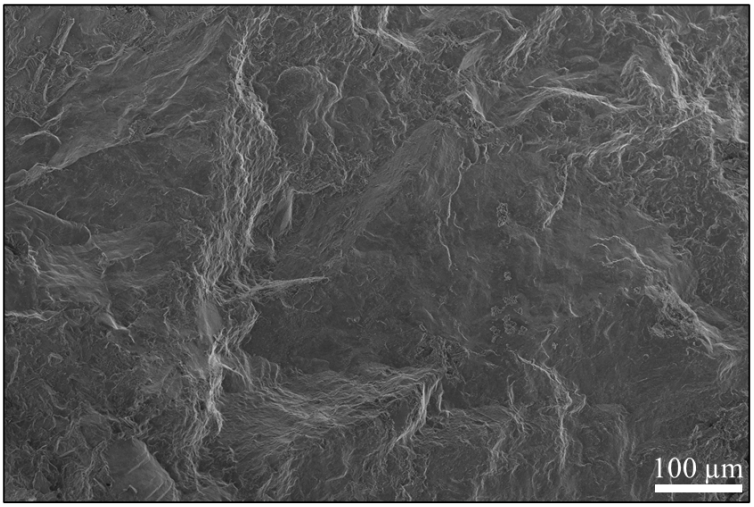

Figure 5.8 A SEM image of the fracture surface.

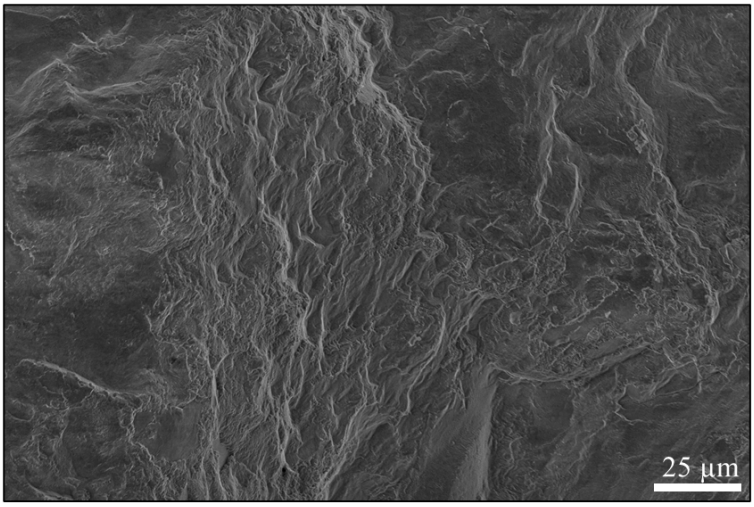

Figure 5.9 A SEM image of the fracture surface.

In the previous study on inch-sized samples (Chapter 4), the peak compaction pressure was 110~300 MPa. In this chapter, P_c is greatly reduced to 50 MPa. This, together with the sectioned CSA operation, much lowers the requirement on the capacity of the compaction machine and the complexity of the mold, beneficial to mass production. It would be desirable to eventually lower P_c to below 15 MPa, in the range of typical compression molding (Advani and Hsiao 2012; Suherman et al. 2013; Tatara 2017). We envision that the strength and the robustness of the material can be further improved by adding microfibers (Beaudoin 1990; Zollo 1997; Wang et al. 2018) or steel rebars (Song and Hwang 2004; Rabi et al. 2019).

5.5 Conclusions

To summarize, through sectioned compaction self-assembly (S-CSA), we scaled up the processing of low-binder-content green concrete from inch-sized to brick-sized. The peak compaction pressure was much reduced. The content of the ordinary portland cement (OPC) binder was only ~10%, significantly less than in regular concrete (25~30%). When

the compaction pressure was 50 MPa, the compressive strength reached ~39 MPa, and the flexural strength was ~8 MPa. The material exhibited certain ductile characteristics in compression. This study proves the concept that the CSA technique can be carried out section by section, which paves the road to the future mass production of larger parts.

Chapter 5, in part, is currently being prepared to be submitted for publication. Haozhe Yi, Kiwon Oh, Rui Kou, and Yu Qiao. “Sectioned Compaction of Low-Binder Concrete Parts”. The dissertation author was the primary investigator and first author of the paper.

Chapter 6 Advanced low-binder-content green concrete

6.1 Introduction

As discussed in Chapters 2-4, the compaction self-assembly (CSA) process offers a promising method to fabricate low-binder-content composites, in which compaction is the key step. In order to produce large parts, it is desirable to minimize the required compaction force, so that the processing system can be relatively simple, mobile, and cost-efficient. Thus, we developed the sectioned compaction self-assembly (S-CSA) technique in Chapter 5. With S-CSA, a relatively high compaction pressure (P_c) can be reached with a relatively small force, as the part is divided into a few sections; in each compaction operation, only one or two sections are compressed.

In addition to the compression area, another important factor is the compaction pressure, P_c. If a satisfactory materials performance can be achieved by using a relatively low P_c, the CSA or S-CSA setup and procedure would be further simplified. In this chapter, we investigate the advanced binders for low-pressure processing of low-binder-content green concrete. The goal is to minimize P_c, with a similar material strength and an improved ductility.

6.2 Components of the advanced binder

The advanced binder used polyvinyl alcohol (PVA) microfiber (MF) (Figure 6.1a), provided by Professor Mo Li from the University of California, Irvine. The fiber length was ~8 mm; the average fiber diameter was 38 μm. Usually, to process a fiber-reinforced composite, e.g., a ultrahigh performance concrete (UHPC), the fibers are added in the last step of mixing (Shi et al. 2015). In our material, however, due to the low binder content,

the mixture was dry and therefore, such a regular approach would lead to a poor fiber dispersion. The MF tended to form tangled, relatively large aggregates. Thus, a two-step mixing procedure was developed, so that the fiber load and the overall rheological properties could be well balanced.

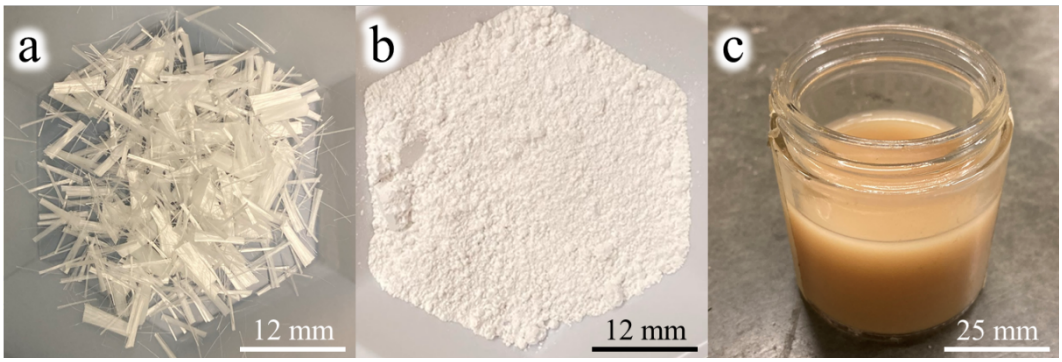

Figure 6.1 Components of the advanced binder: (a) microfiber (MF), (b) ground quartz (GQ), and (c) viscosity modifying admixture (VMA)

Ground quartz (GQ) (Figure 6.1b) and viscosity modifying admixture (VMA) (Figure 6.1c) were also provided by Professor Mo Li at the University of California, Irvine. The GQ had the particle size around 10 μm, and was not chemically reactive. It could improve the concrete strength by filling the gaps among the sand grains, so that the microstructure became denser (Kazanskaya et al. 2019). It also helped to enhance rheology of the concrete mixture (Lagerblad and Vogt 2004). The VMA was usually used in fresh concrete to adjust the workability, e.g., to mitigate bleeding (Leemann and Winnefeld 2007).

6.3 Experimental procedure

Silica sand (grain size #20) was obtained from Fairmount Santrol; gravel was from RCP Block & Brick. They were air-dried for 48 hours before use. Type II/V OPC from

CalPortland was stored in a sealed box. Superplasticizer was obtained from Globmarble (Product name: Melflux 2651F).

A Kitchen Aid professional 600 stand mixer was used for pre-mixing, through a two-step procedure (Figure 6.2). In the first step, OPC, superplasticizer, ground quartz, and about 32% of sand were mixed at the lowest speed for 2 mins, followed by addition of water and VMA. Once the materials were completely wet, the mixing speed was increased to Medium for 5 mins, to produce a paste (Figure 6.2a). The second step used a EUROSTAR mechanical mixer. The mixing time was 5 min., and the speed was 300 rpm. PVA MF were gradually added into the paste (Figure 6.2b), followed by gradually adding gravel and the rest ~68% sand (Figure 6.2c). The mixing continued for another 5 mins at 300 rpm.

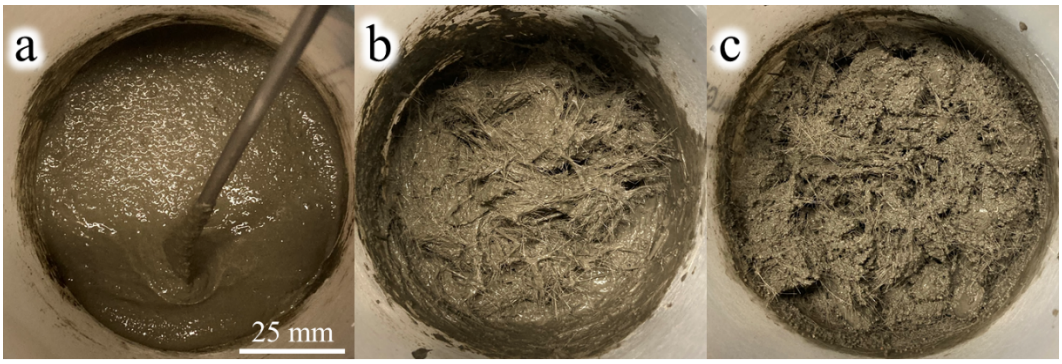

Figure 6.2 The two-step pre-mixing procedure: (a) paste formation, (b) MF dispersion, (c) and the final mixture.

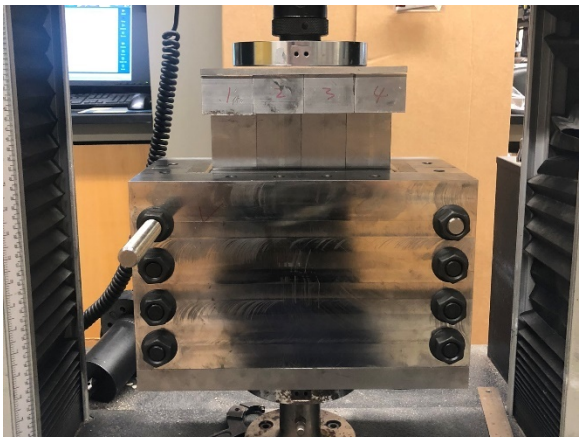

Figure 6.3 Compressing the four compaction pistons simultaneously

The sectioned compaction self-assembly (S-CSA) setup was the same as in Chapter 5. The S-CSA box was assembled on a type-5582 Instron machine. The premixed material was poured into the box in three equal parts. Manual densification and flattening were performed after each pouring. A thin layer of WD-40 lubricant was applied on the surfaces of the four compaction pistons. The pistons were inserted from the top of the compaction box.

Figure 6.4 A sample removed from the compaction system after initial hardening for 2 days

Figure 6.5 Moist curing for 28 days

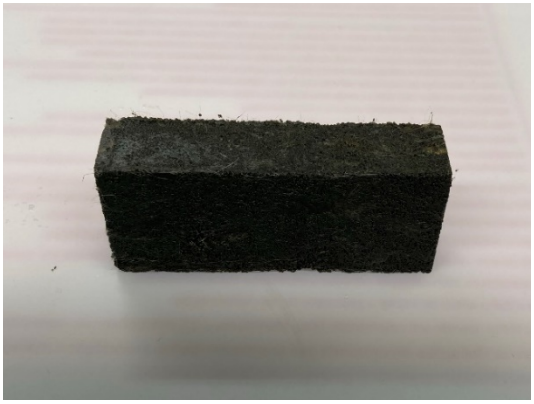

Figure 6.6 A sample after moist curing for 28 days

The S-CSA system was centered on the Instron machine. A 100-kN loadcell was set up and calibrated. The four compaction pistons were compacted simultaneously to 58.07 kN, to reach a compaction pressure (P_c) of 15 MPa (Figure 6.3). The loading rate was 15 mm/min. The pressure was maintained for 1 min, and then the force was released. The compacted material was kept in the compaction system for 2 days at ~22 ℃ for initial hardening (Figure 6.4). Then, it was transferred into a plastic box and covered by wet paper towels for moist curing for 28 days (Figure 6.5). Water was added every 2 days to maintain the moisture environment. A cured sample is shown in Figure 6.6.

Table 6.1 Recipes of the low-binder-content concrete samples with advanced binders

Sample no.	OPC	Sand	Gravel	Water	Fiber	P_c (MPa)	GQ	VMA
1	17%	43.04%	35%	4.96%	0.75%	15		
2	17%	43.04%	35%	4.96%	0.75%	15		0.4%
3	17%	43.04%	35%	4.96%	0.75%	15		0.8%
4	15%	45.04%	35%	4.96%	0.75%	15		
5	15%	44.54%	35%	4.96%	0.70%	15	0.5%	
6	15%	43.54%	35%	4.96%	0.70%	15	1.5%	
7	15%	42.54%	35%	4.96%	0.70%	15	2.5%	
8	15%	43.04%	35%	4.96%	0.70%	15	2.0%	0.2%
9	15%	42.04%	35%	4.96%	0.70%	15	3.0%	0.3%

Nine samples (Table 6.1) were produced for the parameterized study. In Table 6.1, the component amounts are in wt.%; MF and VMA are counted separately. Each sample was ~203 mm long, ~51 mm high, and ~23 mm wide. Cubic specimens and beam-shaped specimens were harvested when the curing time was 7 days, 14 days, or 28 days. The Instron machine was used to measure the compressive strength and the flexural strength. Cubic specimens were used for the compressive strength testing. The size (a) of the specimen was about 24.5 mm × 24.5 mm × 24.5 mm. The specimen was centered on the bottom loading plate, and compressed by the top loading plate at the loading rate of 6 kN/min. The loadcell measured the peak loading force (F_c); loading was stopped when the force dropped by 70% of the peak value. The compressive strength (σ_c) was calculated as $\sigma_c = \frac{F_c}{a^2}$. The beam-shaped specimens were used for three-point bending measurement. Each specimen was about 75 mm long, 13 mm wide (b), and 13 mm high (d). Two round aluminum tips supported the specimen from the bottom, and a third round-tipped aluminum probe compressed the specimen from the top, at the loading speed of 6 kN/min. After the peak loading force (σ_f) was reached, the test was stopped when the loading force decreased

by ~80%. The distance (L) between the two supporting tips was 38.1 mm. The flexural strength was calculated as $\sigma_{\mathrm{f}} = \frac{3LF_{\mathrm{f}}}{2bd^2}$.

6.4 Results and discussion

For each recipe, the compressive strength and the flexural strength were measured from 2 cubic specimens and 4 beam-shaped specimens when the curing times were 7 days, 14 days, or 28 days. The average 28-day strengths of samples 1-3 were shown in Figure 6.7 and Figure 6.8. It considerably increased, when the VMA content rose from 0% to 0.4%. The flexural strength improved only slightly. When we further increased the VMA content from 0.4% to 0.8%, both compressive strength and flexural strength decreased. That is, the optimum VMA content was below 0.4%. VMA costs ~$3.7/kg (Lachemi et al. 2004). The low usage of VMA is required to maintain an excellent cost-performance balance.

The average 28-day strengths of samples 4-9 were shown in Figure 6.9 and Figure 6.10. In addition to GQ, 0.2% and 0.3% VMA were used in sample 8 and sample 9, respectively. Both compressive strength and flexural strength improved as we increased the GQ content from 0% to 3%. The compressive strength was more sensitive to the use of GQ. When the GQ content was 3%, the compressive strength almost doubled, compared to its counterpart without GQ. The most notable improvement was achieved in the range of the GQ content from 1.5% to 2.5%. The flexural strength had a similar but less pronounced trend. It increased by about 40% with 3% GQ.

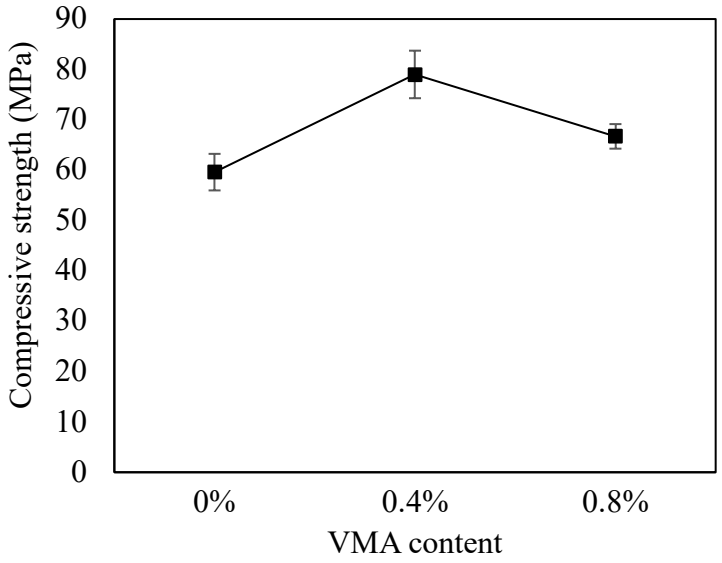

Figure 6.7 Compressive strength as a function of the VMA content

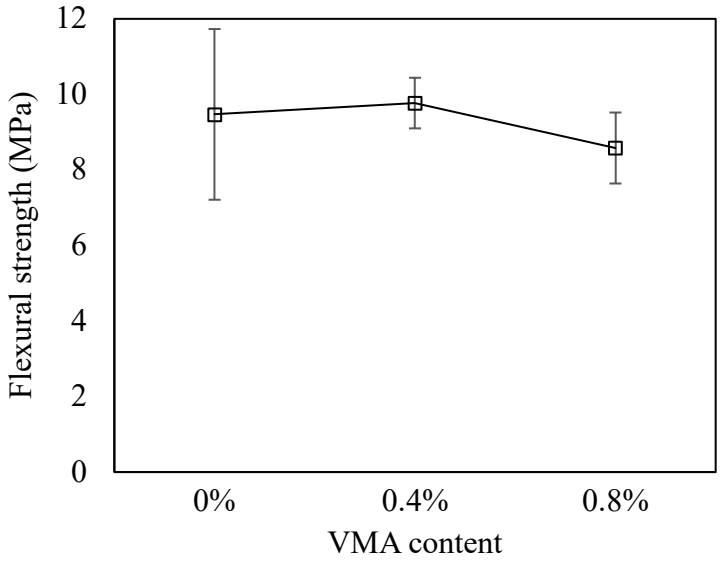

Figure 6.8 Flexural strength as a function of the VMA content

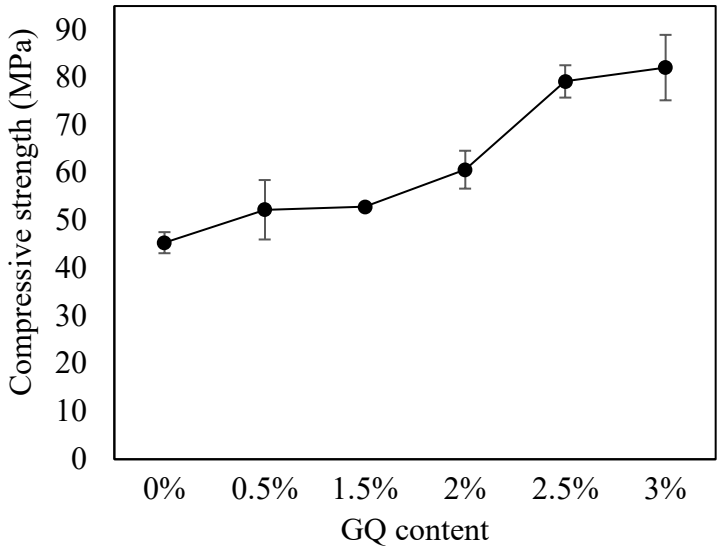

Figure 6.9 Compressive strength as a function of the GQ content

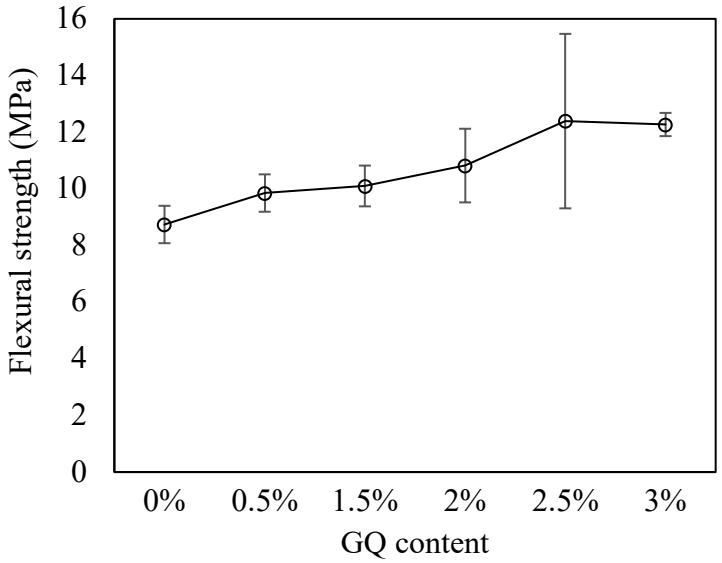

Figure 6.10 Flexural strength as a function of the GQ content

Compared to the compressive strength of typical unreinforced concrete (30-50 MPa) (Kong and Evans 1983), the 28-day strength of our material is about 60%-160% higher. The flexural strength of typical unreinforced concrete is 2-6 MPa (Kong and Evans 1983), compared to which the 28-day flexural strength of our material is about 100%-500% higher. In fact, the flexural strength of our material is comparable with that of typical steel-

reinforced concrete (10-15 MPa) (MacGregor et al. 1997).

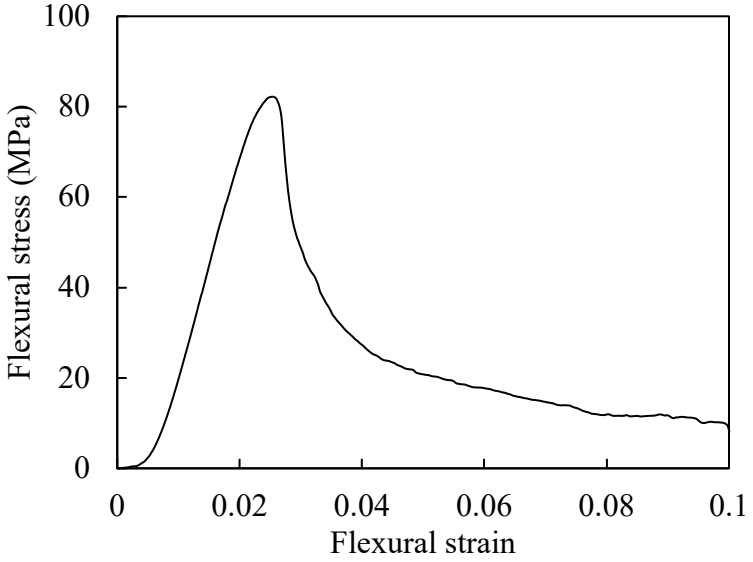

Figure 6.11 A typical compressive stress-strain curve

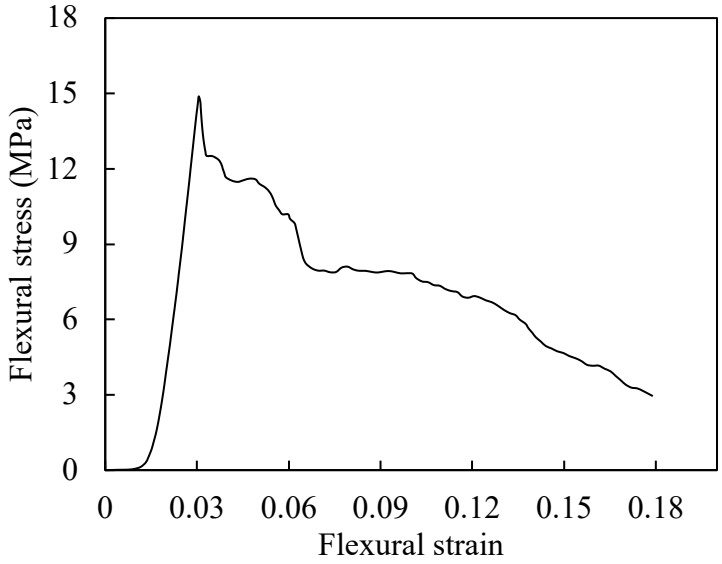

Figure 6.12 A typical three-point bending stress-strain curve

Typical stress-strain testing curves are shown in Figure 6.11 and Figure 6.12. Both compressive and flexural testing curves show significant ductile characteristics, thanks to the toughening effect of MF. After the peak loading is reached, the stress decreases much

more slowly than typical concrete. Particularly, the flexural strain can be as high as ~10%, and the stress is still above one half of the flexural strength. The fracture work, measured by the area under the stress-strain curve, is about two orders of magnitude larger than that of regular concrete (Neville and Brooks 1987).

6.5 Conclusions

In summary, we investigated advanced binders for low-binder-content green concrete, by using PVA microfibers (MF), ground quartz (GQ), and VMA. With only 15% OPC, the material reached a compressive strength of ~80 MPa and a flexural strength of ~12 MPa. MF greatly improved the ductility. VMA and GQ enhanced the workability and the microstructure, which led to a much higher strength. A two-step mixing method was employed to optimize the fiber dispersion. With the advanced binder, the compaction pressure was significantly reduced to 15 MPa.

Chapter 6, in part, is currently being prepared to be submitted for publication. Haozhe Yi, Kiwon Oh, Rui Kou, and Yu Qiao. The dissertation author was the primary investigator and first author of the paper.

Chapter 7 Paver-sized low-binder-content green concrete

7.1 Introduction

In Chapter 5, we scaled up the processing of low-binder-content green concrete from inch-sized proof-of-concept samples to 0.5-kg brick-sized samples. In Chapter 6, we developed advanced binders to improve the material properties and also to simplify the processing condition. Here, we further increase the production scale to fabricate paver-sized samples. Such a sample weights about 10 kg (or 20 lbs).

A new compaction system was designed. In order to produce relatively large samples by using a regular hydraulic machine, the compression operation should be completed section by section, through sectioned compaction self-assembly (S-CSA). It should be adaptive to a wide variety of processing parameters, such as compaction pressure, compaction sequence, and sample shape. The expected compaction pressure range was 10 MPa to 100 MPa. The system must be reusable, and operable by 1-2 people. Desirably, it should be formed by a set of strong and durable components, with each component being sufficiently small and lightweight. The setting and the disassembly procedures need to be straightforward and fast. The deformation of the system during compaction should be negligible; no permanent damage was allowed. Safety must be ensured by adequate protective parts. In addition, an appropriate mixing method was required, to process at least 10 kg materials in one batch, paving the path for the future larger-sized production of 500-lb samples. For S-CSA, the main concerns include the required processing time and the uniformity of loading.

7.2 Compaction system design

A production system for 10-kg paver-sized samples (PS20) was designed and fabricated. PS20 consisted of two large sidewalls, two small sidewalls, a bottom plate, four joint blocks, four compaction pistons, an extension rod, a securing plate, two sets of securing bars, a spacer, and a holding plate. All the parts were made of aluminum 6061 alloy. Figure 7.1 shows the assembled compaction system.

Figure 7.1 The assembled compaction system (PS20)

The two large sidewalls were 254 mm high, 406.4 mm wide, and 76.2 mm thick. A 3.175 mm gap was procedurally left on the inner surface of each large sidewall. It allowed for chafing-free movement of the compaction pistons. The small sidewalls were 254 mm tall, 254 mm wide, and 76.2 mm thick. They were placed in between the two large sidewalls to form the box-shaped mold. The large sidewalls were connected to the small sidewalls by twelve 1.00-8 high-strength grade 8 steel hex head screws. Likewise, a 3.175-mm gap was designed on the inner surface of the small sidewalls, to avoid excessive friction with

the compaction pistons.

A bottom plate was placed under the box and connected with the four sidewalls by joint blocks. On each joint block, five 1.00-8 high-strength grade-8 steel hex head screws were used to secure the connection. With such a design, the bottom plate could be disassembled from the sidewalls without lifting the entire system. The length and the width of the bottom plate were both 508 mm, and the thickness was 76.2 mm. Each joint block was 254 mm long, 63.5 high, and 50.8 mm wide.

Four compaction pistons were used to perform S-CSA. Each piston was 152.4 mm high, 127 mm long, and 127 mm wide. They could be compressed either individually or together. To compress a single piston, an extension rod was used. The diameter of the rod was 101.6 mm; the height was 152.4 mm. When only one or two pistons were compressed, if the sample thickness was small or the required compaction pressure was high, the squeezing effect might be non-trivial. To mitigate this problem, we designed a securing plate for the adjacent sections. It was a 254 mm-long, 254 mm-wide, 76.2 mm-thick plate; about 1/4 of the plate was removed to form an opening. Six 1.00-8 high-strength steel threaded rods and steel nuts connected the securing plate to the top of the sidewalls. Thus, when a piston was compressed by the extension rod, the other sections can be firmly held in place by the plate.

Two sets of securing bars were installed around the four sidewalls to enhance the safety. To efficiently adjust the height of the sample material, a 254 mm-long, 254 mm-wide, and 63.5 mm-thick spacer was placed at the bottom of the mold. If needed, the spacer thickness could be changed. A 254 mm-long, 254 mm-wide, and 6.35 mm-thick holding plate was on top of the spacer, for the convenience of sample transfer.

7.3 Experimental procedure

Two 10-kg samples were produced and tested. The binder was ordinary portland cement (OPC). The recipes are shown in Table 7.1. The compaction pressure (P_c) was 90 or 95 MPa. The component amounts are in wt.%. Superplasticizer (1% of the OPC weight) was used for both samples.

Table 7.1 Recipes of paver-sized green concrete samples

Sample #	OPC	Sand	Limestone	Water	P_c (MPa)
1	14%	39.50%	39.50%	7.0%	90
2	14%	39.85%	39.85%	6.3%	95

All-purpose sand was from Quikrete. Crushed limestone was from Greensmith Landscaping. They were dried in air for 24 hours before use. Type II/V OPC was provided by CalPortland, stored in a sealed box. Melflux-2651F superplasticizer was obtained from Globmarble.

Figure 7.2 Pre-mixing

Figure 7.3 Transferring the pre-mixed materials into the PS20 mold.

S-CSA was carried out by a SATEC universal testing machine, which had a capacity of ~363 tons. The PS20 system was assembled on the loading stage of the SATEC machine. The surfaces of the sidewalls and the compaction pistons were cleaned before assembly. The spacer and the holding plate were placed in the mold. Thin steel liners (0.6 mm in thickness) were attached onto the inner surfaces of the mold. Two Kitchen Aid professional 600 series stand mixers were used for pre-mixing (Figure 7.2). For each sample, the materials were divided into four equal parts. For each part, OPC, sand and crushed limestone were first mixed at a low speed (~60 rpm) for 2 mins. Then, water was added, and the material was continuously mixed for another 5 mins. After pre-mixing, the paste was transferred into the mold, and manually flattened (Figure 7.3). A layer of Sta-Lube marine grease was applied on the surfaces of the compaction pistons. The pistons were placed on top of the premixed material.

Figure 7.4 Initial compaction: compacting the four pistons simultaneously

The PS20 system was centered on the loading stage. The SATEC machine was set to the compression mode and calibrated. An initial compaction was performed on the four pistons simultaneously, until the compaction pressure (P_c) reached 25 MPa (Figure 7.4). The pressure was held for 1 min and released. Then, the securing plate was placed on top of the compaction pistons, and tightly bolted on the sidewalls. The extension rod was placed on the piston to be compacted, through the opening in the securing plate. S-CSA was carried out by alternatively compressing each piston to 90 or 95 MPa (Figure 7.5). At each piston, the peak pressure was maintained for 1 min, followed by releasing the force. S-CSA was conducted clockwise, until all the pistons were compressed.

Figure 7.5 S-CSA: compacting the pistons individually through the extension rod

Figure 7.6 Removing the bottom plate and pushing the sample from the bottom opening of the PS20 mold.

After S-CSA, the sample remained in the mold for 2 days. Then, the bottom plate was disassembled, and the sample was pushed out from the bottom opening (Figure 7.6), during which two wood blocks were used to raise the compaction system, with a thick cushioning foam sheet underneath it. The extracted sample is shown in Figure 7.7. Moist

curing was performed at room temperature for 28 days (Figure 7.8).

Figure 7.7 An extracted paver-sized low-binder-content green concrete sample

Figure 7.8 Moist curing at room temperature for 28 days

The cured samples were cut into cubic and beam-shaped specimens for compressive strength testing and flexural strength testing, respectively (Figure 7.9). A RIDGID 10 in. wet tile saw sectioned the samples and an ENCO MM491G bench sander polished the specimen surfaces. The size of the cubic specimens was ~25 mm. The size of the beam-shaped specimens was ~50 mm long, 13 mm wide, and 13 mm high. The specimens were harvested from different locations of the paver-sized sample, including corner, interior, boundary, and middle sections (Figure 7.10).

Figure 7.9 Cutting the paver-sized sample into cubic and beam-shaped specimens

Figure 7.10 Harvesting specimens from different locations of each sample

After wet cutting with the tile saw, the specimens were dried in ambient air for 1 day. Capping was performed on the cubic specimens with USG hydro-stone. Compressive strength testing was performed by compressing the cubic specimen at a loading rate of 6 mm/min, until the material was crushed (Figure 7.11). The compressive strength was calculated as $\sigma_c = F_c/A$, where F_c is the peak loading force and A is the cross-sectional area. The compressive strain was calculated as $\varepsilon_c = D/L_0$, where D is the displacement and L_0 is the initial height. Three-point bending tests were performed on the beam-shaped specimens for flexural strength measurement. Two aluminum round-tipped pins supported the specimen at the two ends from the bottom. Another aluminum round-tipped pin

compressed the specimen in the middle from the top, at the loading rate of 6 mm/min, until final failure occurred (Figure 7.12). The flexural strength was calculated as $\sigma_f = 3F_f L/(2bd^2)$, where F_f is the peak loading force, L is the span between the two supports (38 mm), b and d are the specimen width and height, respectively. The flexural strain was calculated as $\varepsilon_f = 6Dd/L^2$. The materials characterization used an Instron model 5582 universal testing machine.

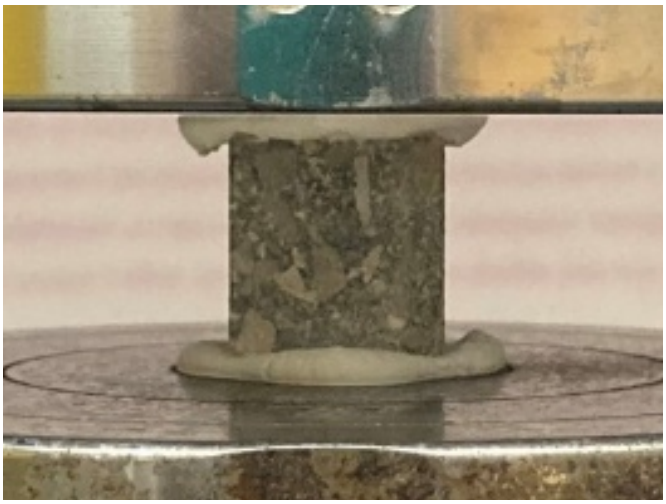

Figure 7.11 A cubic specimen in the compressive strength measurement test.

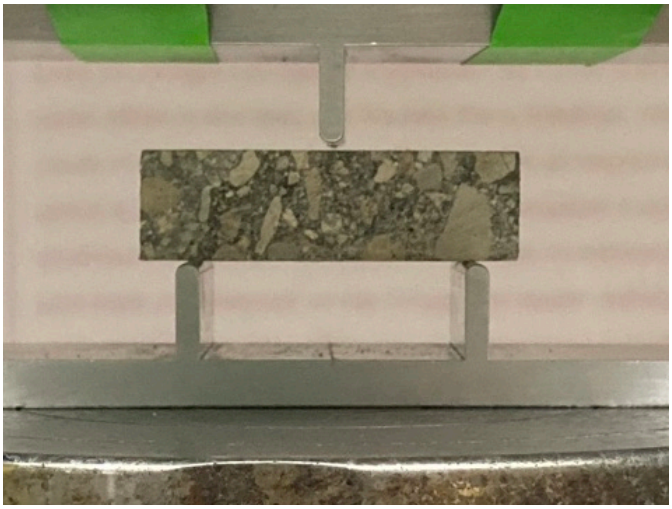

Figure 7.12 A beam-shaped specimen in the flexural strength measurement test.

7.4 Results and discussion

The measured 28-day compressive strength and flexural strength are shown in Figure 7.13 and Figure 7.16. The average strength and the standard deviation are calculated from four nominally same specimens for each data point (Figure 7.14 and Figure 7.17). For a regular unreinforced concrete, the 28-day compressive strength is typically in the range of 30-50 MPa (Kong and Evans 1983), and the 28-day flexural strength is typically 3-6 MPa (Kong and Evans 1983), with the OPC content of 25~30% (Shakhmenko and Birsh 1998). In our material, the OPC content (c) is only 14%, more than 30% lower than that of a regular concrete. The compressive strength of the low-binder-content green concrete is 56.7 MPa, ~13% higher than the high end of the range of regular concrete. The flexural strength of our material is 10.3 MPa, ~70% higher than the high end of the range of regular concrete. The flexural strength of steel-reinforced concrete is usually in the range of 10-15 MPa (MacGregor et al. 1997). It can be seen that our material falls in this range. Typical testing curves are given in Figure 7.15 and Figure 7.18.

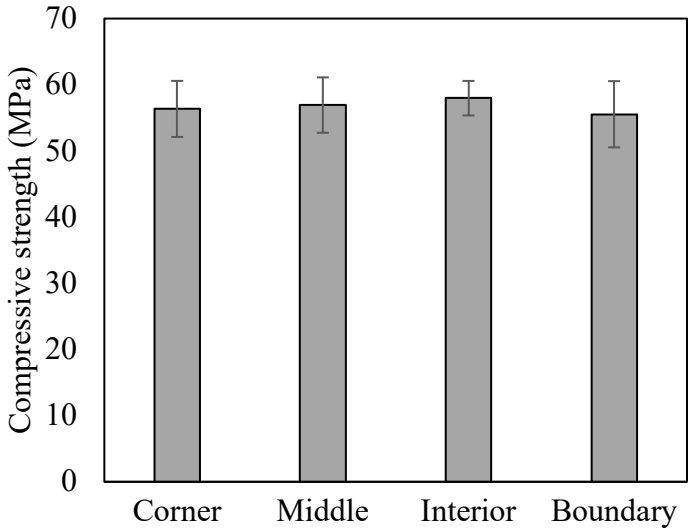

Figure 7.13 Compressive strength of paver-sized green concrete samples

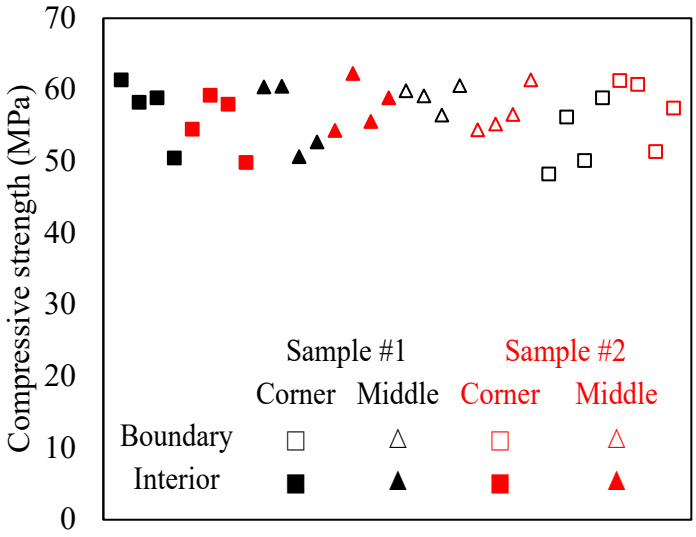

Figure 7.14 Data distribution of compressive strength

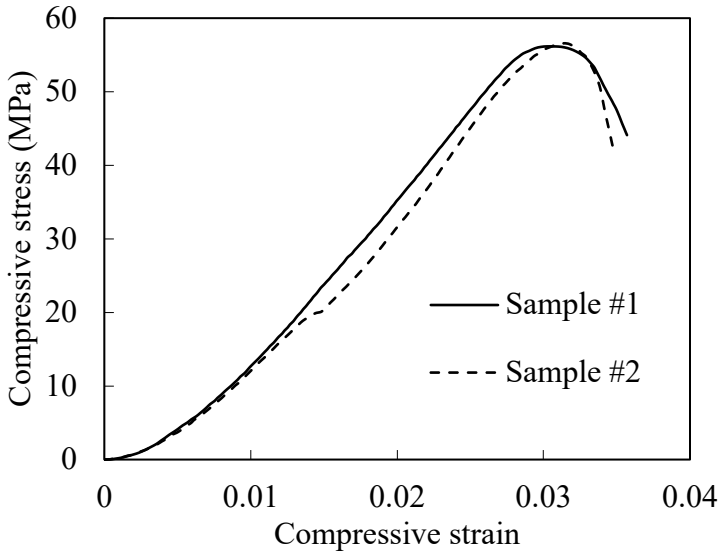

Figure 7.15 Typical compressive strength testing curves

The strength-measurement specimens are harvested from various locations in the paver-sized samples. In Figure 7.14 and Figure 7.16, “boundary” indicates the area in between the compaction pistons; “interior” indicates the area underneath a compaction piston; “corner” indicates the corner area on the large sample; “middle” indicates the middle section of the large sample. According to Figure 7.17, no evident strength

difference can be observed among the different locations. For all the locations, the data scatter of compressive strength is ~7.1%, and the data scatter of flexural strength is ~8.4%, comparable to regular concrete materials (e.g., (Neville and Brooks 1987)). Clearly, the material produced through S-CSA is quite uniform, and the properties of the two samples are similar. Typical testing curves are given in Figure 7.18.

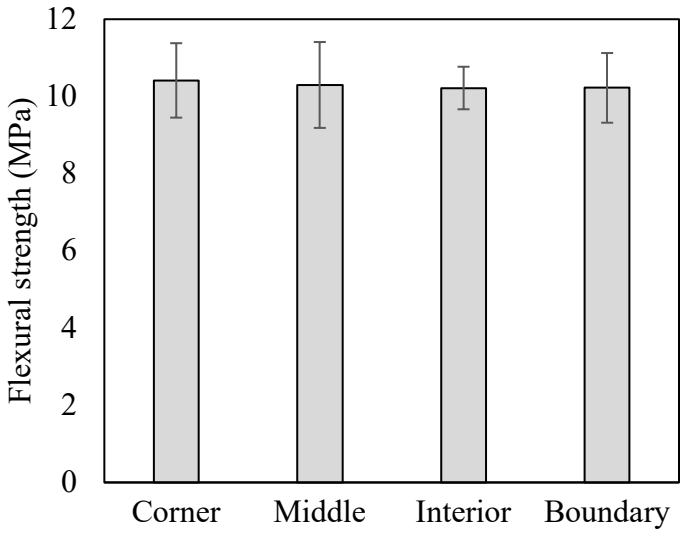

Figure 7.16 Flexural strength of paver-sized green concrete samples

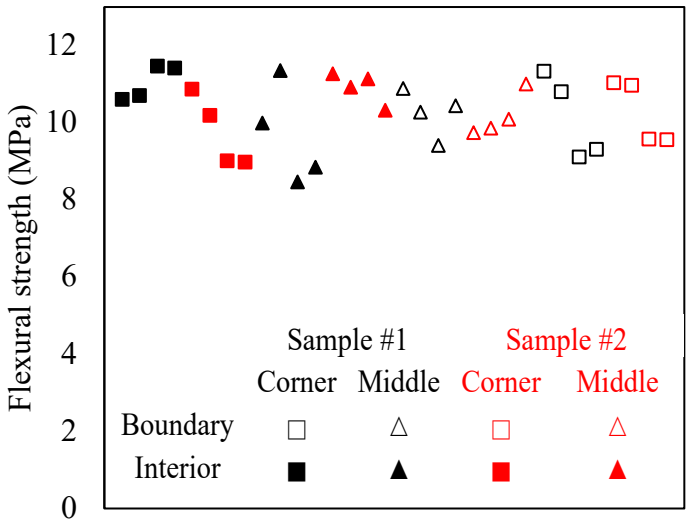

Figure 7.17 Data distribution of flexural strength

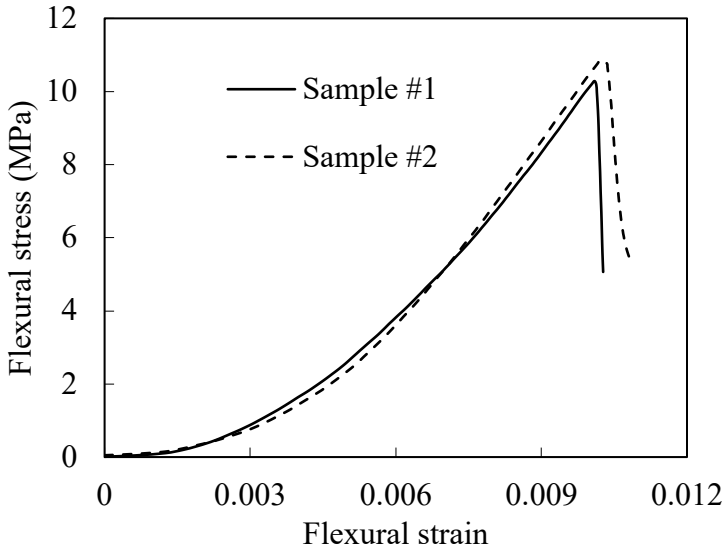

Figure 7.18 Typical flexural strength testing curves

SEM image was taken from the fracture surface of Sample #2. As can be seen in Figure 7.19, the compacted concrete material is dense and uniform.

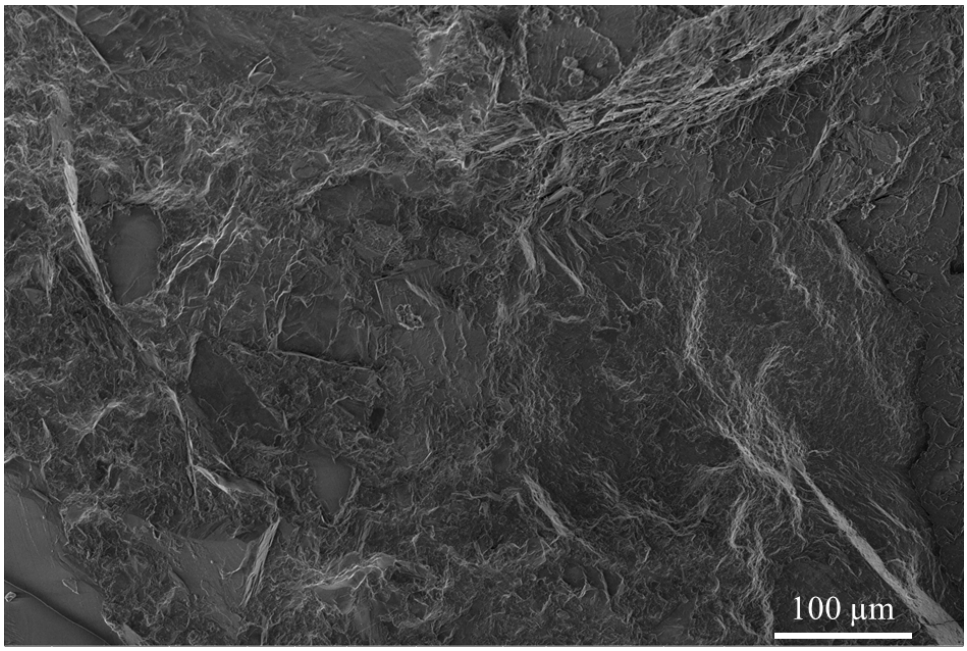

Figure 7.19 Typical SEM image taken from the fracture surface of Sample #2

7.5 Conclusions

To summarize, through sectioned compaction self-assembly (S-CSA), we scaled up the production of low-binder-concrete green concrete from brick-sized samples to paver-sized samples. A PS20 compaction system was designed and fabricated. With only 14% OPC binder, when the compaction pressure (P_c) was 90-95 MPa, the compressive strength was 56.7 MPa, and the flexural strength was 10.3 MPa. This study demonstrates that S-CSA can be used to produce uniform large-sized samples, which paves the road to our future study on full-size production.

Chapter 7, in part, is currently being prepared to be submitted for publication. Haozhe Yi, Kiwon Oh, Rui Kou, and Yu Qiao. The dissertation author was the primary investigator and first author of the paper.

Chapter 8 Slab-sized low-binder-content green concrete

8.1 Introduction

Compaction self-assembly (CSA), particularly sectioned compaction self-assembly (S-CSA), is the key technology for production of large-sized low-binder-content green concrete, as discussed from Chapter 4 to Chapter 7. In Chapter 4, we started with the prove-of-concept tests on inch-sized small samples. In Chapter 5, we designed and fabricated a S-CSA system, and successfully produced brick-sized samples. In Chapter 6, advanced binders were developed, which not only improved the material properties but also reduced the compaction pressure. It paved the path to the work in Chapter 7, where we increased the scale of the compaction setup to produce paver-sized green concrete samples. The experimental measurement confirmed that S-CSA was able to fabricate high-quality large concrete parts with a uniform microstructure.

In the current chapter, we further scale up the S-CSA processing. The goal is to produce and test slab-sized low-binder-content green concrete parts, with the mass more than 200 kg. Such a size is directly relevant to many industrial applications, e.g., slabs in residential buildings, pedestrian bridge decks, etc. Success of this work will also open a door to fabrication of larger-sized construction components, such as beams, columns, pipes, to name a few.

8.2 Compaction system design

The flexural test steel load (FTSL) fixture in Powell's Lab at the University of California, San Diego was used to transfer the compaction load from the actuators to the compaction plates (Figure 8.1). It was 3.3 m long, 0.86 m wide, and 0.76 m high. The

actuators were eight Enerpac HCL series hydraulic jacks, each having a load capacity of 136 tons. As shown in Figure 8.2, they were placed on top of the FTSL fixture and connected to the control panel. The hydraulic jacks were attached to the reinforced-concrete floor by eight 2”-2 thick screws, through the through-holes to the basement (Figure 8.3). The screws were locked by matching washers and nuts. When the hydraulic jacks were operated in the Extension mold, the FTSL fixture were pushed downwards. The through-holes on the concrete floor were 0.61 m apart from each other. The dimensions of the FTSL fixture, the location of the hydraulic jacks, and the size of the steel mold were designed to fit with the floor plan.

Figure 8.1 The 3.3 m-long flexural test steel load (FTSL) fixture.

Figure 8.2 Eight hydraulic jacks (the yellow cylinders) attached to the FTSL fixture

Figure 8.3 The hydraulic jacks are attached to the reinforced concrete floor.

As shown in Figure 8.4, the steel mold defined the shape of the green concrete sample. It consisted of two large sidewalls, two small sidewalls, and a bottom plate. The inner space of the mold was 1.83 m in length, 0.61 m in width, and 0.15 m in height. The thickness of the large sidewalls and the bottom plate were 100 mm and 50 mm, respectively. One of the small sidewalls was 50 mm thick and was made of steel. The other small sidewall was 75 mm thick and was made of aluminum 6061. These parts were assembled by using ½”-20 high strength threaded rods and nuts.

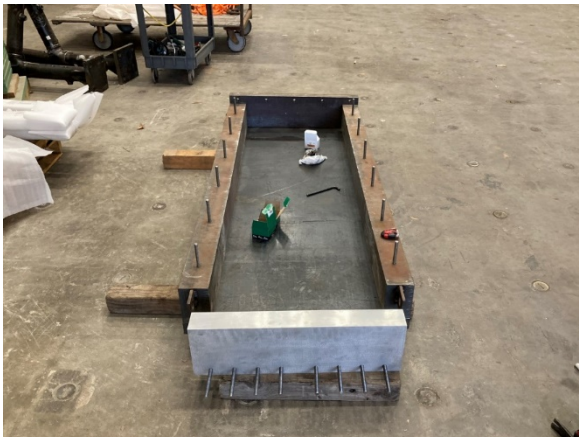

Figure 8.4 The steel mold. The compaction plates are not shown.

A reinforcing frame helped to carry the lateral expansion force during the

compaction. It consisted of two hollow structural section (HSS) beams. Each HSS beam was 150 mm wide and 150 mm high, with the wall thickness of 12.7 mm. As shown in Figure 8.5 and Figure 8.6, the HSS beams were connected by 2”-2 screws and nuts at both sides, along the short direction of the mold. Steel angles were welded on the two ends of the HSS beams, for load carrying along the long direction. Holes were drilled on one side of the steel angles. Threaded rods passed through the holes, to tighten or loosen the frame during assembly and disassembly (Figure 8.7).

Figure 8.5 The reinforcing frame and the mold (side view)

Figure 8.6 The reinforcing frame and the mold (front view)

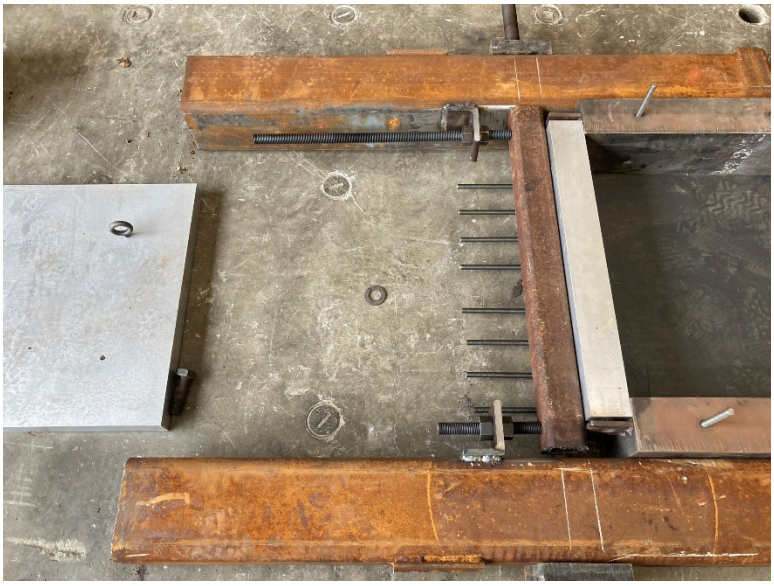

Figure 8.7 Threaded rods pass through drilled holes on the steel angles, to tighten or loosen the system.

As shown in Figure 8.8, a number of 610 mm long, 610 mm wide, and 50 mm thick aluminum 6061 compaction plates were fabricated. Three plates could fully cover the steel mold from the top, separating it into three sections. S-CSA was performed by compressing one plate at a time. According to necessity, more compaction plates could be added on top

of the first layer for height adjustment. Drill holes and eyebolts were used by the compaction plates for handling and lifting.

Figure 8.8 The compaction plates and the fixing bars

As one of the compaction plates was being compressed, the other two were secured by four fixing bars (Figure 8.8). They were bolted on the threaded rods on the large sidewalls of the mold. The fixing bar was made of aluminum 6061. Each bar was 810 mm long, 100 mm wide, and 50 mm in height.

Table 8.1 Compositions of the three slab-sized green concrete samples*

Sample	OPC	Sand	Gravel	Water	GQ	SP	VMA	MF	P_c
1	15%	42.04%	35%	4.96%	3%	0.15%	0.3%	0.7%	15 MPa
2 & 3	15%	42.75%	35%	4.25%	3%	0.15%	0.3%	0.7%	15 MPa

* All components are in weight percentage; SP, VMA, MF are listed as additional weights.

8.3 Experimental procedure

The compositions of three low-binder-content green concrete samples are shown in Table 8.1, using the advanced binders developed in Chapter 6. No. 20 silica sand was

obtained from Fairmount Santrol. Gravel was from RCP Block & Brick. Type II/V OPC was from CalPortland. Superplasticizer (SP) was from Globmarble (Product name: Melflux 2651F). PVA microfibers (MF), ground quartz (GQ), and viscosity-modifying admixture (VMA) were provided by Professor Mo Li at the University of California, Irvine. As shown in Figure 8.9 and Figure 8.10, sand and gravel were dried in air for 2 days before use. A fan was used to accelerate the drying process.

Figure 8.9 Sand drying for 2 days

Figure 8.10 Gravel drying for 2 days

A 0.127 mm-thick impact resistant polycarbonate sheet was used as the liner (Figure 8.11). It covered the inner surfaces of the steel mold and the bottom surface of the

compaction plates.

Figure 8.11 Covering the mold by a liner.

A common-purpose Collomix TMX 1500 mixer was used for pre-mixing (Figure 8.12 and Figure 8.13). The motor output was 2.8 kW, and the mixing speed was 30 RPM. The diameter and the depth of the mixer chamber were 610 mm and 508 mm, respectively; the capacity was 40 gallons.

Figure 8.12 Side view of the Collomix TMX 1500 mixer

Figure 8.13 The chamber of the Collomix TMX 1500 mixer

The two-step mixing method (Chapter 6) was employed for the MF dispersion. About 1/3 of the sand was first mixed with the OPC, GQ, and SP, followed by adding water and VMA to form a paste (Figure 8.14 and Figure 8.15). After mixing for 15 mins, MF were manually added (Figure 8.16). The mixing continued for another 15 mins. Once the MF were relatively uniformly dispersed, the rest of the sand and the gravel were slowly poured in the mixer (Figure 8.17). The MF-paste mixture was stirred for another 15 mins. The pre-mixed materials were transferred into the steel mold, manually flattened, and then covered by the three compaction plates (Figure 8.18).

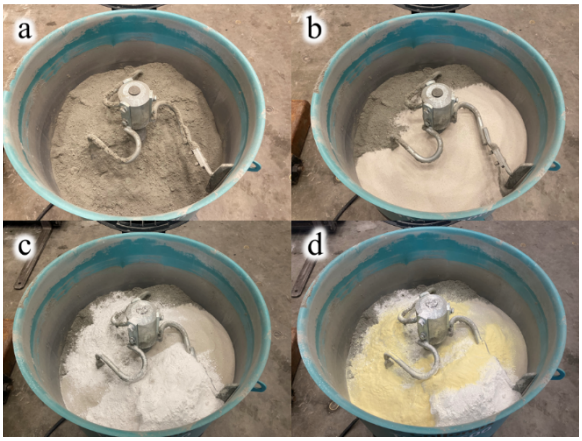

Figure 8.14 Pre-mixing of dry materials: (a) ordinary portland cement (OPC), (b) 1/3 of sand, (c) ground quartz (GQ), and (d) superplasticizer (SP)

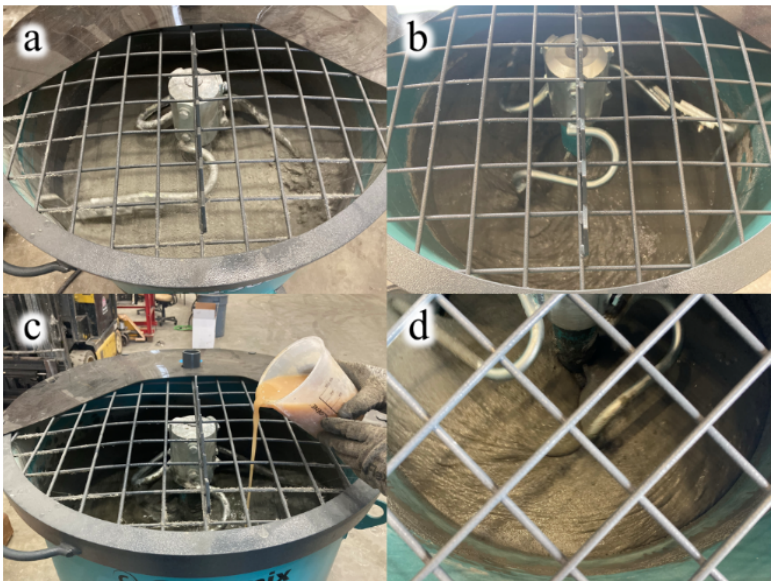

Figure 8.15 The first step of pre-mixing: (a) mixing of dry materials, (b) adding water into the mixer, (c) adding VMA, and (d) the produced paste.

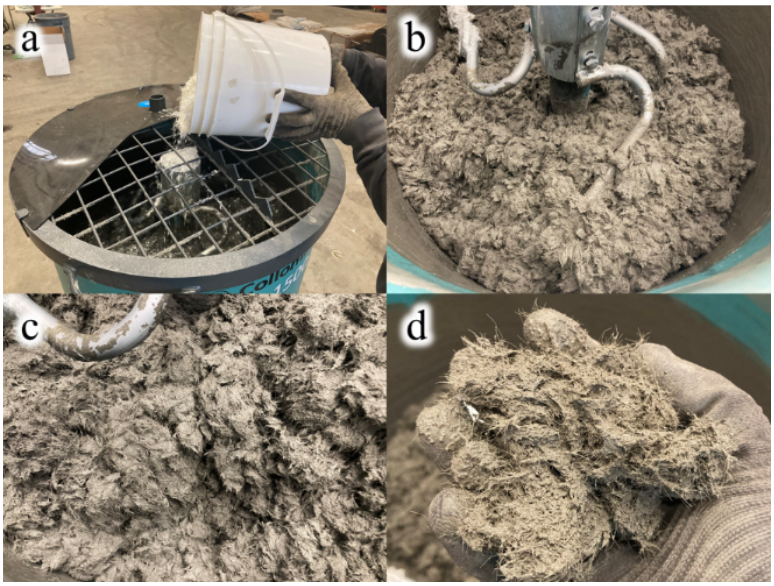

Figure 8.16 The first step of premixing (continued): (a) gradually adding MF into the mixer, (b) blending MF with the paste, (c) a close view of the MF-paste mixture. (d) MF are relatively well separated and dispersed in the paste

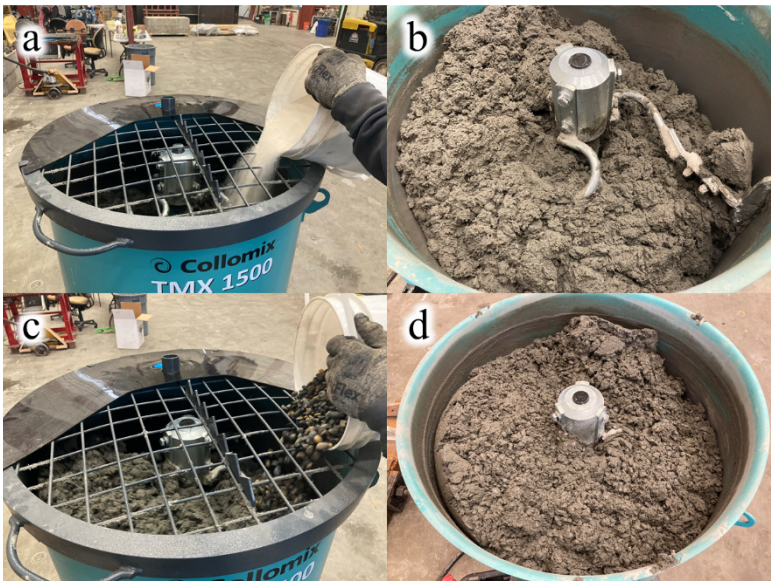

Figure 8.17 The second step of pre-mixing: (a) gradually adding the other 2/3 of sand into the mixer, (b) mixing the sand with the MF-paste mixture, (c) gradually adding gravel into the mixer, and (d) the pre-mixed material

Initial compaction was performed by compressing all the three compaction plates simultaneously. It helped to reduce the height difference between adjacent sections. Two concrete-filled HSS beams were placed on top of the compaction plates. A total force of 8585 kN was applied, to reach a compaction pressure of 7.5 MPa (Figure 8.19).

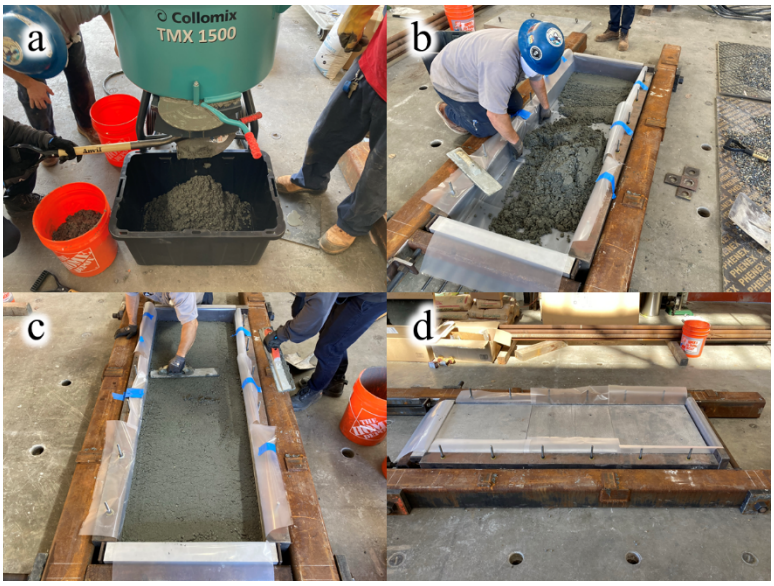

Figure 8.18 (a) Pouring the pre-mixed material from the bottom gate of the mixer, (b) pouring the pre-mixed materials into the steel mold, (c) flattening the pre-mixed material, and (d) adding the three compaction plates onto the mold.

Figure 8.19 (a) Placing concrete-filled HSS beams on top of the compaction plates. (b) The HSS beams cover all the three sections. (c) Lifting and placing the FTSL fixture on top of the HSS beams. (d) Fixing screws to the concrete floor and compacting the three sections simultaneously

Figure 8.20 Sectioned compaction: (a1-a2) compaction of the first section, (b1-b2) compaction of the second section, and (c1-c2) compaction of the third section

S-CSA was carried out by alternately compressing the three sections, from one side of the mold to the other side. A total force of 5725 kN was applied to each section, to reach the peak compaction pressure of 15 MPa. The procedure is shown in Figure 8.20. Four fixing bars secured the two plates that were not loaded.

After the S-CSA operation, the sample was kept in the mold at ambient temperature for initial hardening. After 3 days, the reinforcing frame was removed, and the mold was disassembled by lifting the compaction plates and removing the small sidewalls. Then, the sample was pushed out. The demolding procedure is shown in Figure 8.21.

Figure 8.22 shows a produced sample. It was ~1.8 m long, ~0.6 m wide, and ~0.09 m thick. Moist curing was conducted at ambient temperature for 28 days. The sample was

covered by rags and hosed until thoroughly wet. A plastic sheet covered the sample to maintain the moisture (Figure 8.23). Water was added every 2 days.

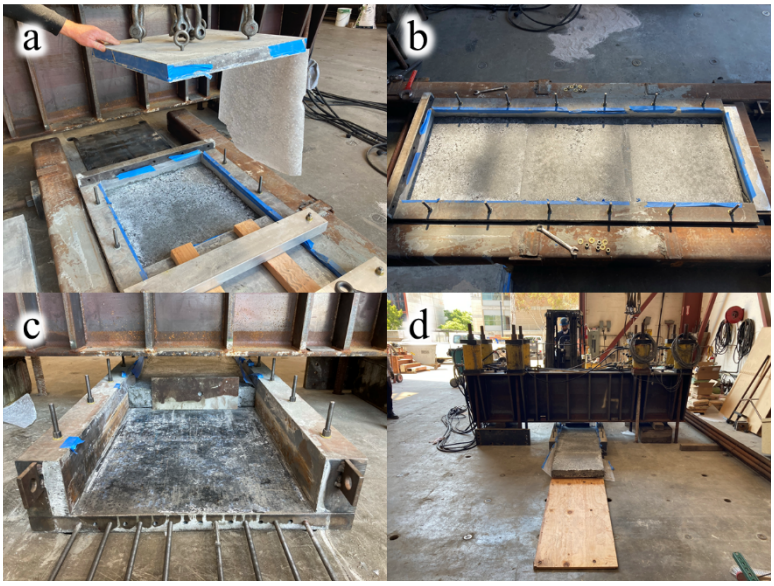

Figure 8.21 The demolding procedure: (a) lifting the compaction plates, (b) removing the reinforcing frame and the small sidewalls, (c) pushing the sample from one side along the long direction, and (d) sliding the sample onto a plywood plate

Figure 8.22 A slab-sized low-binder-content green concrete sample

Compressive strength testing and flexural strength testing were conducted

throughout the curing process. Small-sized testing specimens (Figure 8.24d) were harvested from various locations of each slab-sized large sample, including corner, interior, and boundary (Figure 8.24b), to measure the local material properties. The cutting tools (Husqvarna K970 III concrete saw and RIDGID 10 in. wet tile saw) are shown in Figure 8.24 (a) and Figure 8.24 (c).

Figure 8.23 Moist curing at ambient temperature for 28 days

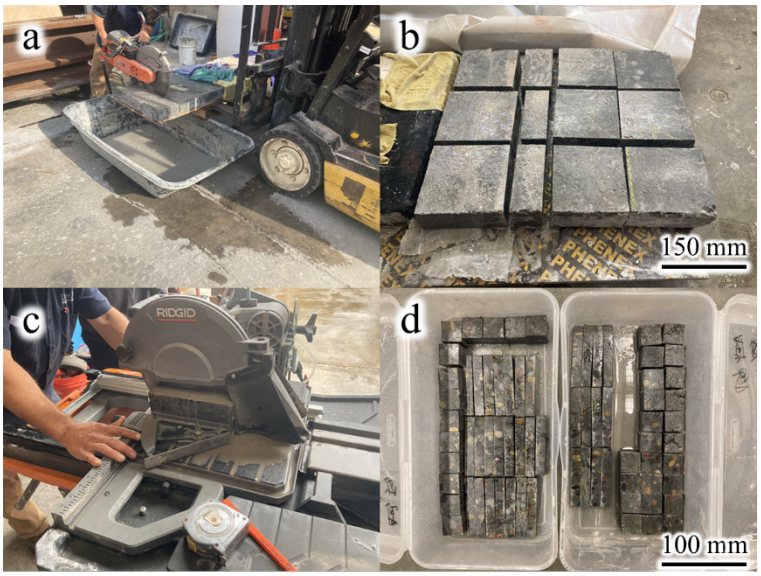

Figure 8.24 Specimen cutting: (a) dividing a slab-sized concrete sample by a Husqvarna K970 III concrete saw; (b) blocks from different locations (corner, interior, and boundary); (c) harvesting testing specimens from each block; (d) the sectioned cubic specimens and beam-shaped specimens

Cubic specimens (25 mm large) were crushed to measure the compressive strength (Figure 8.25). They were end-capped with USG hydro-stone. A type-5582 Instron universal testing machine compressed the specimen at a loading speed of 6 mm/min, until final failure happened. The peak force (F_c) was recorded. The compressive strength was calculated as $\sigma_c = \frac{F_c}{ab}$, where a is the length and b is the width.

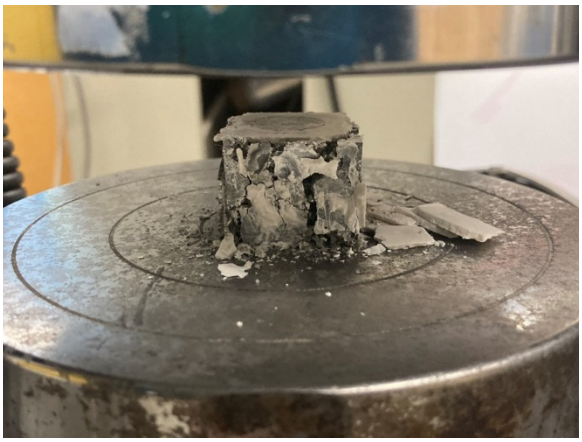

Figure 8.25 A crushed cubic specimen

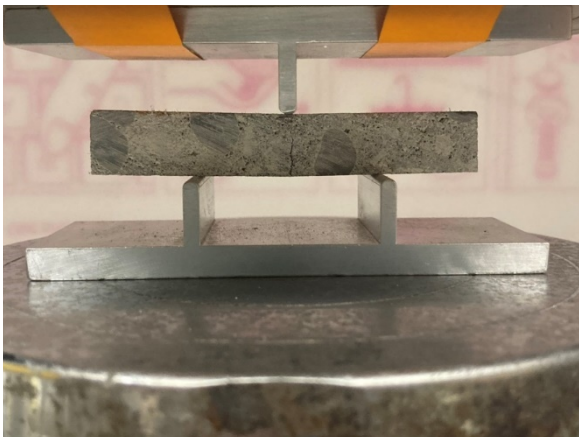

Figure 8.26 A beam-shaped specimen

Beam-shaped specimens (Figure 8.26) were tested in a three-point bending setup to measure the flexural strength. The specimen was about 13 mm × 13 mm × 76 mm large. Similar to the testing setup in Chapter 7, two round-tip supports carried the specimen at the two ends, and a third pin compressed the specimen in the middle from the top. The loading rate was 6 mm/min, and the peak force (F_f) was recorded. The flexural strength was calculated as $\sigma_f = \frac{3LF_f}{2bd^2}$, where L is the span between the two supports, b is the width, and d is the height.

Table 8.2 The composition of the reference concrete

OPC	Sand	Gravel	Water
23.05%	31.17%	34.91%	10.87%

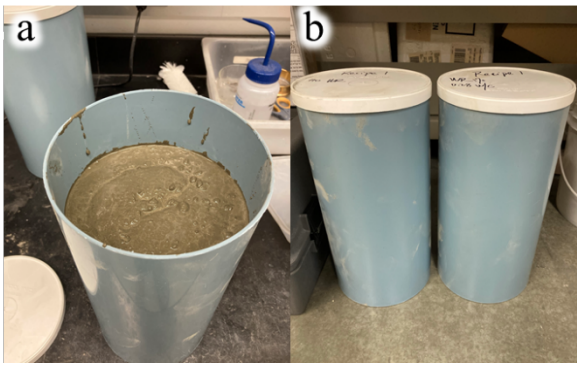

Figure 8.27 Production of the reference concrete sample: (a) casting; (b) curing.

Reference concrete samples were produced (Table 8.2), following ASTM C192/192M. No superplasticizer (SP) was added. The materials were manually mixed with a small shovel. Standard cylinders (152.4 mm × 304.8 mm) with flat lids were used for casting (Figure 8.27a). The material was sealed by the lids and cured in the cylinder for 28 days (Figure 8.27b). No compaction was performed. After curing, the reference concrete was removed from the cylinders and cut into cubic or beam-shaped specimens, similar to the green concrete samples.

8.4 Results and discussion

Altogether, 3 slab-sized samples were produced and tested. As shown in Table 8.1, the water content in Sample 1 was 4.96%. Binder loss was observed during compaction (Figure 8.28). The water content in Sample 2 and Sample 3 was 4.25%. No binder loss could be detected during S-CSA.

Figure 8.28 Binder loss of Sample 1 during compaction

The measured 28-day compressive strength and flexural strength of Sample 1 are shown in

Table 8.3, Figure 8.29, and Figure 8.30. Four specimens are tested for each location. Typical compressive and flexural testing curves and results are shown in Figure 8.31 and Figure 8.32. Ductility is measured by the fracture work, i.e., the area under the stress-strain curve. Sample 1 is 20-50 times more ductile than the reference concrete (Table 8.4).

Table 8.3 The 28-day compressive strength and flexural strength of Sample 1

Compressive strength (MPa)				Flexural strength (MPa)			
Location		Ave.	Std dev.	Location		Ave.	Std dev.
Corner	top	77.29	2.61	Corner	top	9.70	0.76
	bottom	77.79	4.11		bottom	10.84	0.81
Interior	top	71.59	0.82	Interior	top	10.75	0.58
	bottom	71.66	3.38		bottom	10.87	0.53
Boundary	top	77.20	3.95	Boundary	top	10.12	0.81
	bottom	70.28	3.50		bottom	10.59	0.74

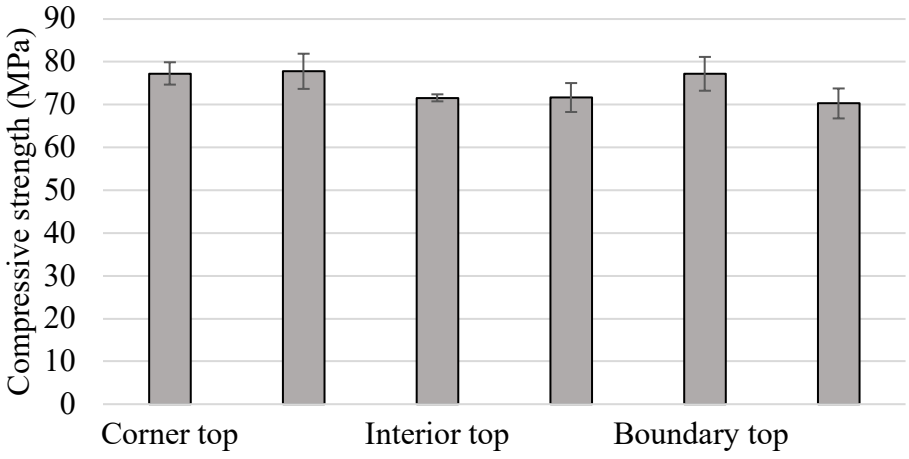

Figure 8.29 The 28-day compressive strength of Sample 1

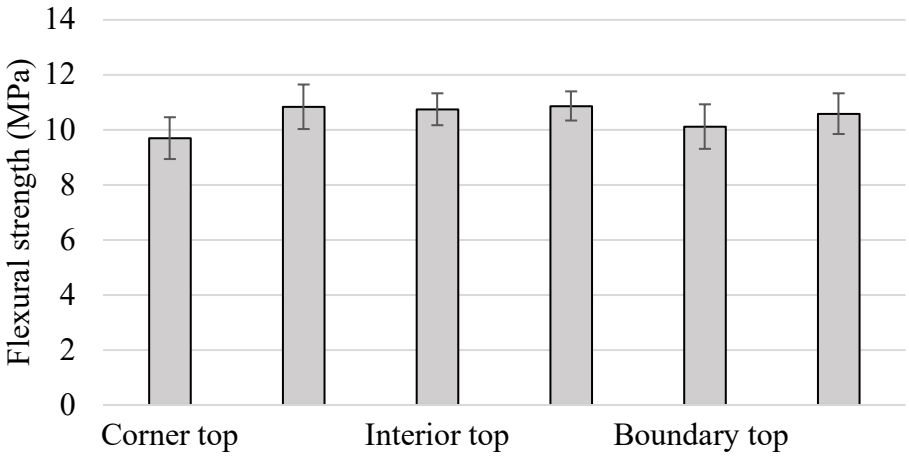

Figure 8.30 The 28-day flexural strength of Sample 1

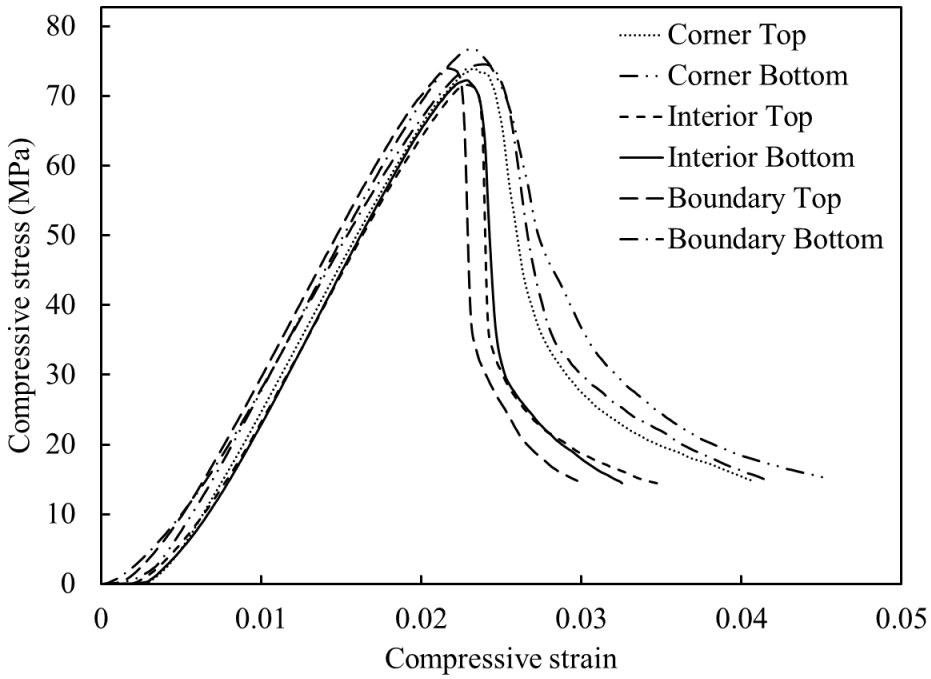

Figure 8.31 Typical 28-day compressive strength testing curves of Sample 1

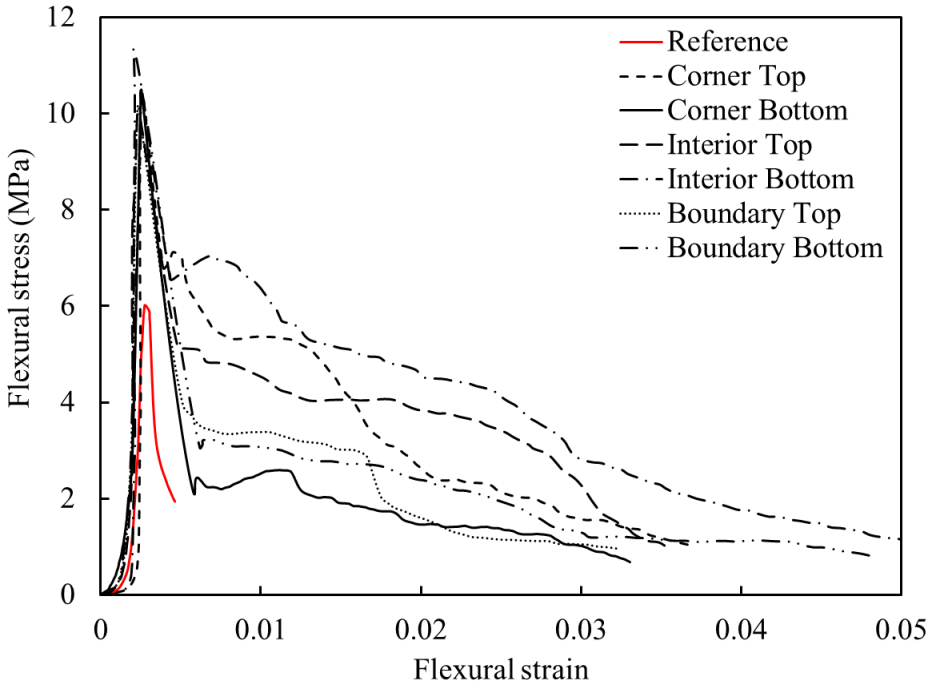

Figure 8.32 Typical 28-day flexural strength testing curves of Sample 1

Table 8.4 Fracture work calculated from the 28-day flexural strength testing curves of Sample 1

Location		Fracture work (MPa)	Reference fracture work (MPa)
Corner	top	0.12165	0.00333
	bottom	0.06979	
Interior	top	0.12977	
	bottom	0.18856	
Boundary	top	0.08210	
	bottom	0.10746	

The measured 28-day compressive strength and flexural strength of Sample 2 are shown in Table 8.5, Figure 8.33, and Figure 8.34. Four specimens were tested for each location. Typical compressive and flexural testing curves and results are shown in Figure 8.35 and Figure 8.36. It is 40-80 times more ductile than the reference concrete (Table 8.6).

Table 8.5 The 28-day compressive strength and flexural strength of Sample 2

Compressive strength (MPa)				Flexural strength (MPa)			
Location		Ave.	Std dev.	Location		Ave.	Std dev.
Corner	top	97.67	3.28	Corner	top	15.09	0.36
	bottom	98.16	4.13		bottom	14.61	0.50
Interior	top	102.07	2.38	Interior	top	15.25	0.64
	bottom	98.31	4.20		bottom	15.37	0.64
Boundary	top	101.33	2.68	Boundary	top	15.26	0.91
	bottom	98.66	2.88		bottom	14.93	0.47

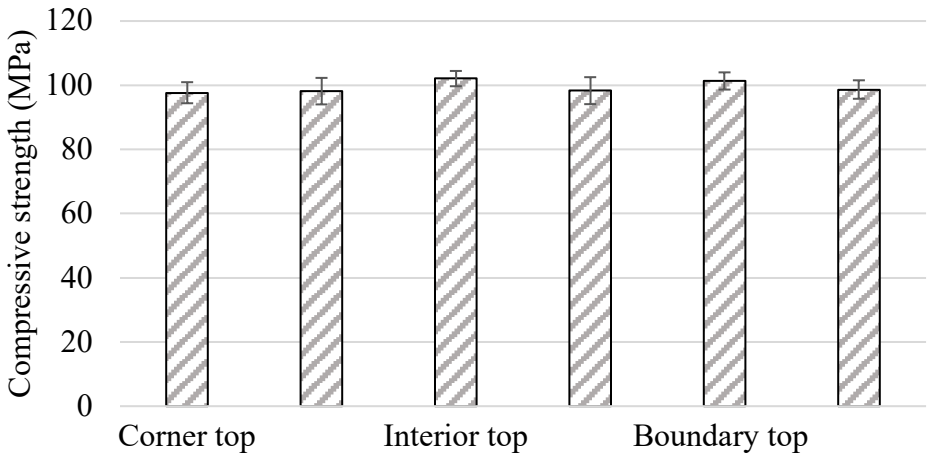

Figure 8.33 The 28-day compressive strength of Sample 2

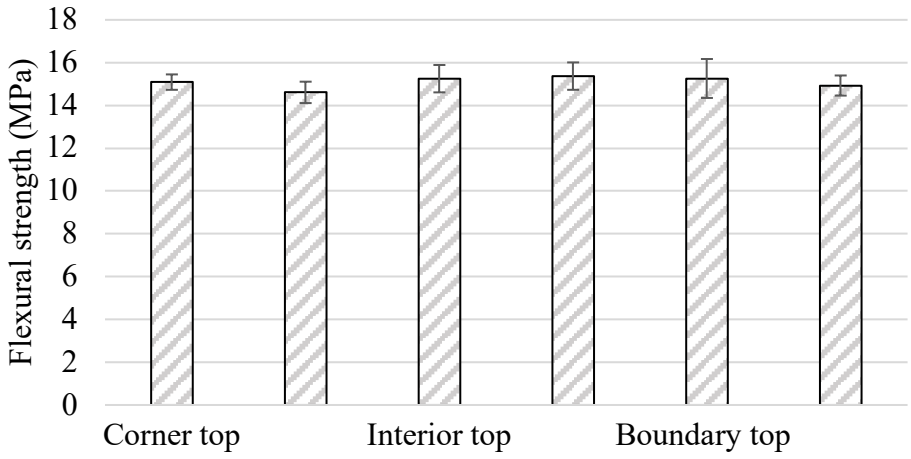

Figure 8.34 The 28-day flexural strength of Sample 2

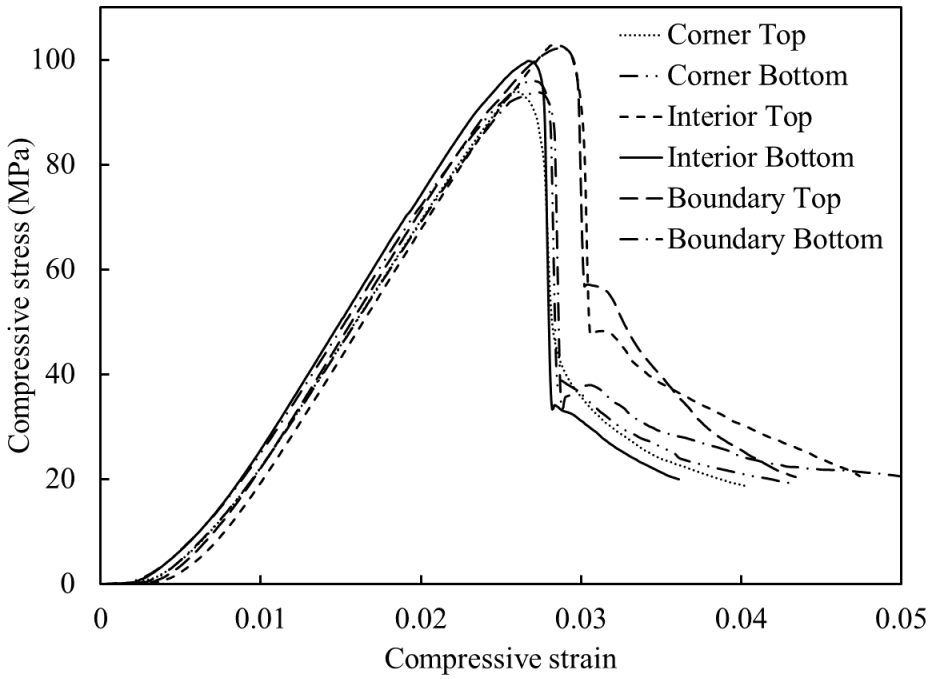

Figure 8.35 Typical 28-day compressive strength testing curves of Sample 2

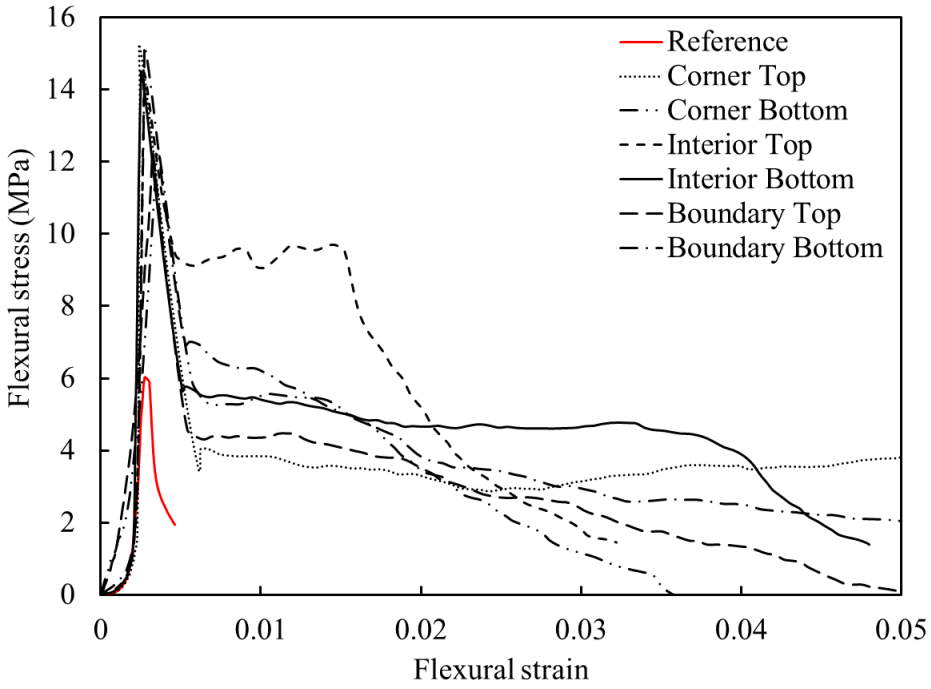

Figure 8.36 Typical 28-day flexural strength testing curves of Sample 2

Table 8.6 Fracture work calculated from the 28-day flexural strength testing curves of Sample 2

Location		Fracture work (MPa)	Reference fracture work (MPa)
Corner	top	0.22055	0.00333
	bottom	0.13314	
Interior	top	0.19490	
	bottom	0.21805	
Boundary	top	0.14453	
	bottom	0.27002	

The measured 28-day compressive strength and flexural strength of Sample 3 are shown in Table 8.7, Figure 8.37, and Figure 8.38. Four specimens were tested for each location. Typical compressive and flexural testing curves and results are shown in Figure 8.39 and Figure 8.40. It is 20-90 times more ductile than the reference concrete (Table 8.8).

Table 8.7 The 28-day compressive strength and flexural strength of Sample 3

Compressive strength (MPa)				Flexural strength (MPa)			
Location		Ave.	Std dev.	Location		Ave.	Std dev.
Corner	top	103.82	3.67	Corner	top	15.18	0.86
	bottom	104.59	2.33		bottom	14.88	1.00
Interior	top	103.79	5.31	Interior	top	14.69	0.98
	bottom	99.49	2.55		bottom	15.85	0.85
Boundary	top	100.73	2.33	Boundary	top	16.03	0.68
	bottom	100.70	4.72		bottom	15.78	0.92

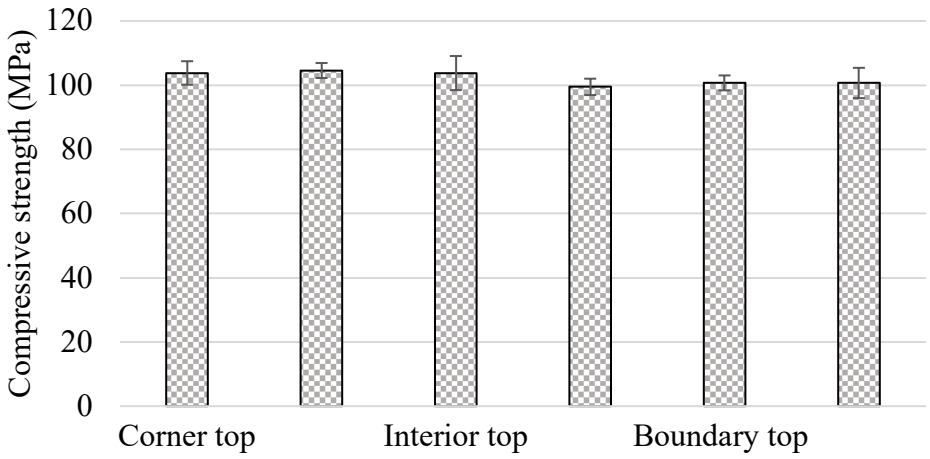

Figure 8.37 The 28-day compressive strength of Sample 3

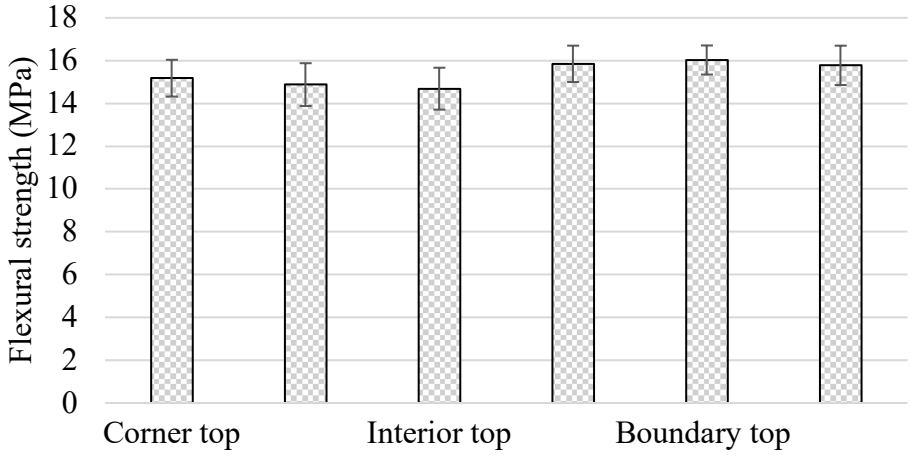

Figure 8.38 The 28-day flexural strength of Sample 3

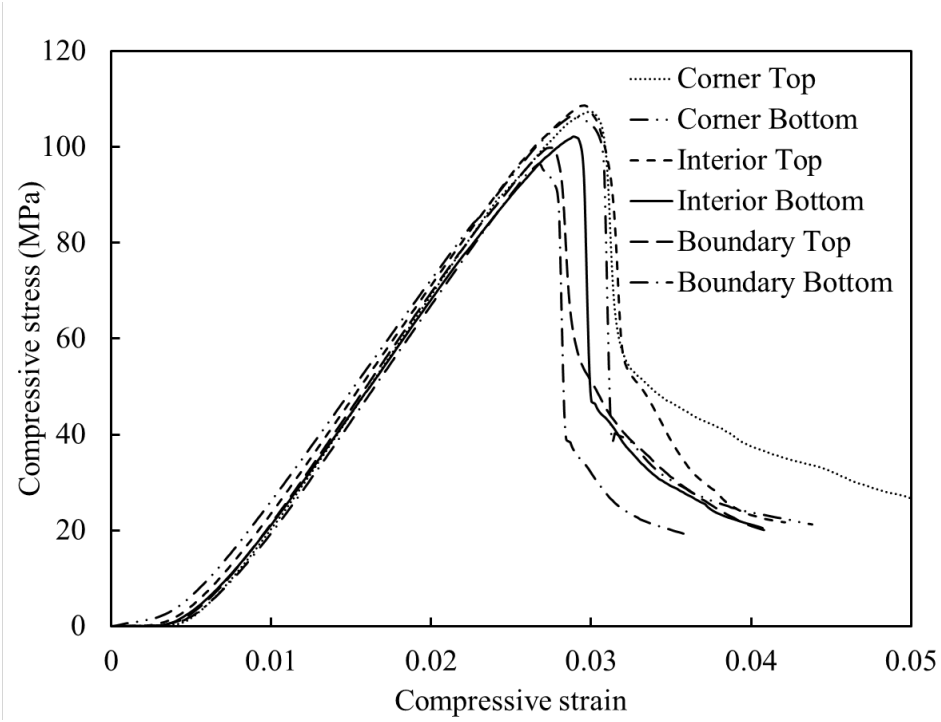

Figure 8.39 Typical 28-day compressive strength testing curves of Sample 3

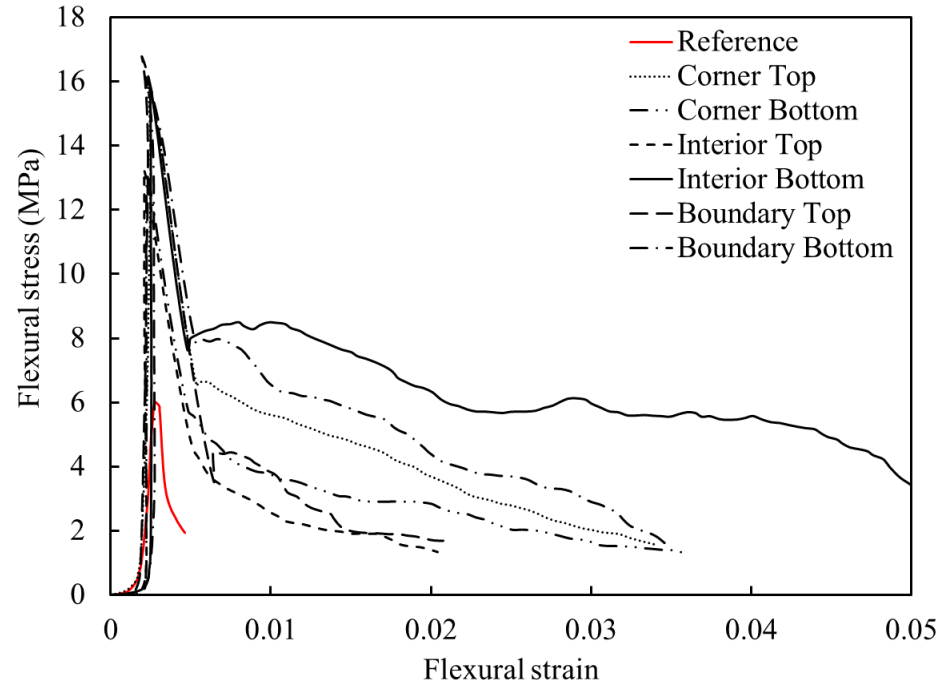

Figure 8.40 Typical 28-day flexural strength testing curves of Sample 3

Table 8.8 Fracture work calculated from the 28-day flexural strength testing curves of Sample 3

Location		Fracture work (MPa)	Reference fracture work (MPa)
Corner	top	0.14715	0.00333
	bottom	0.10892	
Interior	top	0.06166	
	bottom	0.33691	
Boundary	top	0.08256	
	bottom	0.17059	

Figure 8.41 and Figure 8.42 summarize the strengths of the three slab-sized samples. The average 28-day compressive strength of Sample 2 and Sample 3 is 100.8 MPa, much higher than the compressive strength of regular concrete (usually in the range of 35-55 MPa) (Mehta 1986), somewhat comparable to the compressive strength of ultrahigh-performance concrete (UHPC) (120 to 150 MPa) (Schmidt et al. 2004). Notice that the low-binder-content green concrete is based on only 14% OPC, nearly halved from a typical concrete.

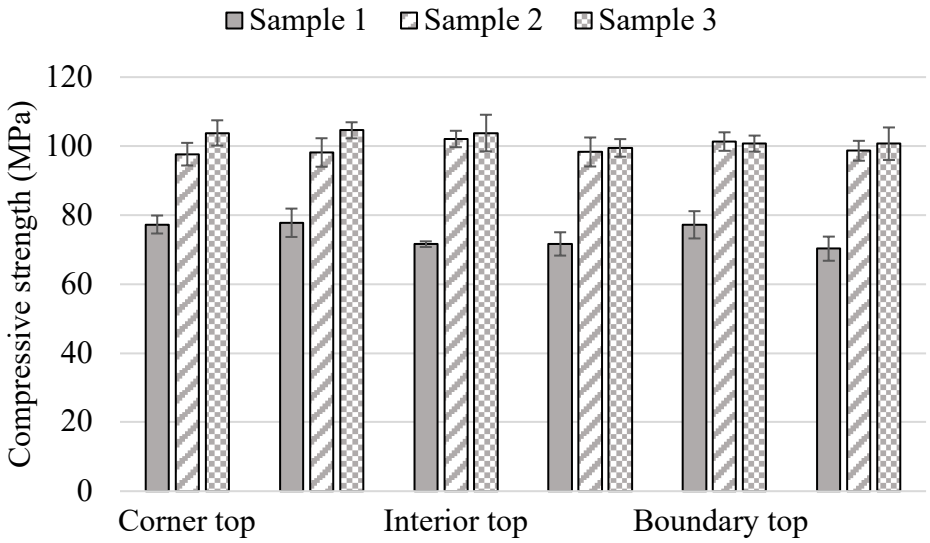

Figure 8.41 Comparison of the 28-day compressive strengths of Samples 1, 2, and 3

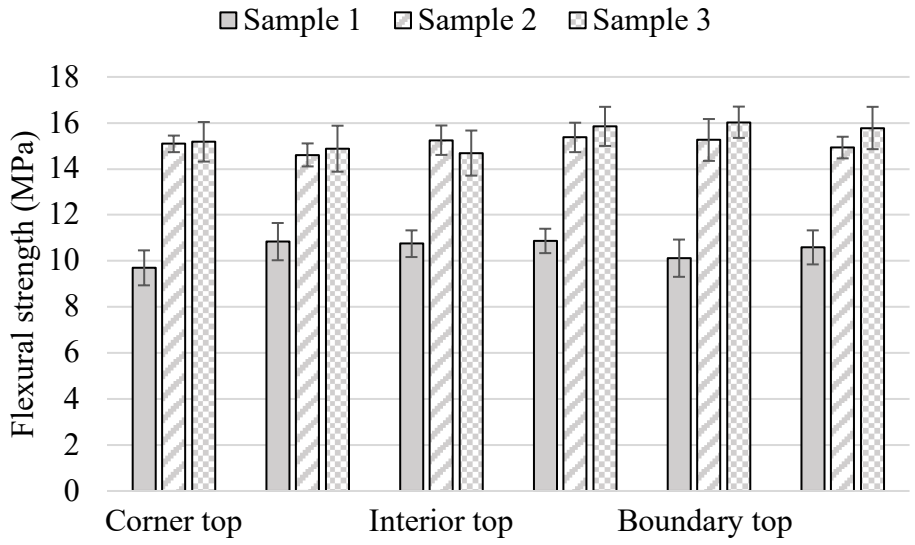

Figure 8.42 Comparison of the 28-day flexural strengths of Samples 1, 2, and 3

The average flexural strength of Sample 2 and Sample 3 is 15.2 MPa. Compared with the typical flexural strength of unreinforced concrete (2-6 MPa) (Mehta 1986), the material is many times stronger. For steel-reinforced concrete, the typical flexural strength is usually 10-15 MPa (MacGregor et al. 1997). The low-binder-content green concrete has reached the high-end of that range. Even compared with UHPC, which typically has a

flexural strength between 15 and 25 MPa (Schmidt et al. 2004), the material is on the same level.

The compaction pressure is only 15 MPa, in the range of regular compression molding (Tatara 2017). At such a relatively low pressure level (compared to P_c = 110 MPa in Chapter 4), the S-CSA system design and operation is quite straightforward, beneficial to the cost-performance balance as well as the operational safety.

As shown in Figure 8.41 and Figure 8.42, at different locations, the strength varies by 4-9%; Sample 2 and Sample 3 have similar properties. Such a data scatter is normal for regular concretes (Kong and Evans 1983). That is, the produced material is uniform. This is confirmed by the SEM images taken from different specimens (Figure 8.43 and Figure 8.44). The SEM images show that the microstructure is dense, and the microfibers are well bonded.

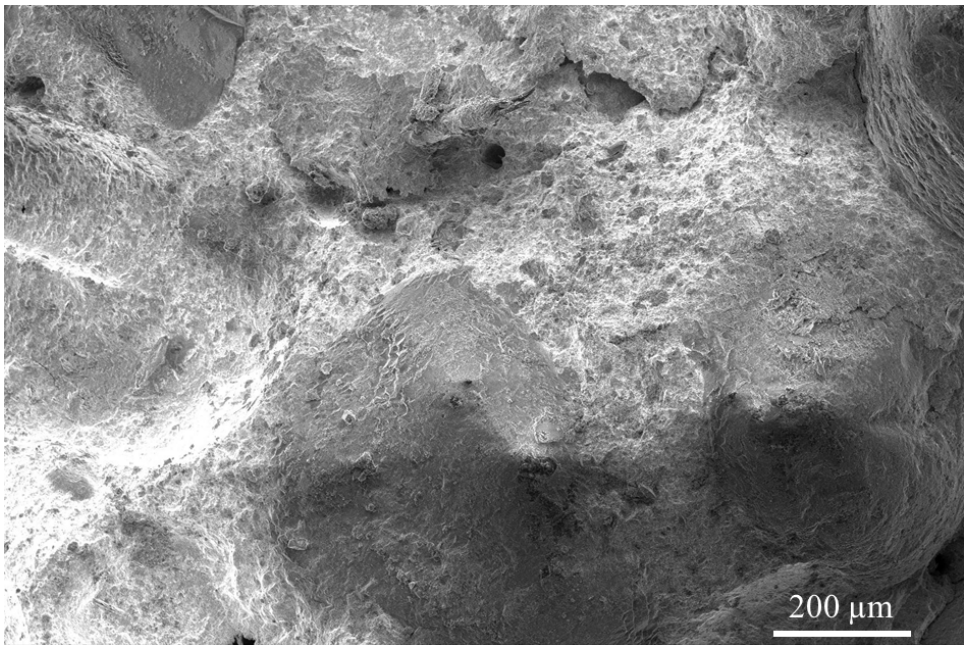

Figure 8.43 SEM image taken from fracture surface of Sample 3

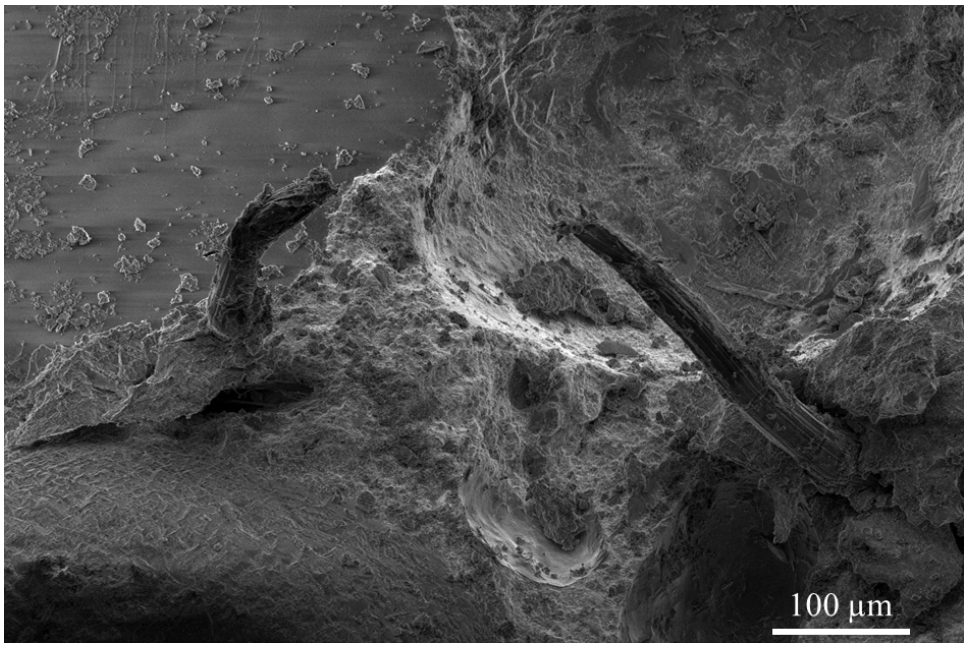

Figure 8.44 SEM image showing that MF are well embedded (Sample 3)

8.5 Conclusions

To summarize, through sectioned compaction self-assembly (S-CSA), we produced slab-sized, 220-kg low-binder-content green concrete samples. A compaction system was designed and fabricated. With a compaction pressure of 15 MPa, with only ~14% cement binder, the average compressive strength of the produced material could be more than 100 MPa, and the flexural strength could exceed 15 MPa. The ductility was 20-90 times better than that of regular concrete. The uniformity was satisfactory. This study paved the road to manufacturing full-size structural components.

Chapter 8, in part, is currently being prepared to be submitted for publication. Haozhe Yi, Kiwon Oh, Rui Kou, and Yu Qiao. The dissertation author was the primary investigator and first author of the paper.

Chapter 9 Summary and future work

In the current study, we systematically investigated the compaction self-assembly (CSA) technique to fabricate green construction materials. Sectioned compaction self-assembly (S-CSA) was developed to scale up the production.

Through CSA, we processed a sand-filler thermoplastic-binder composite material using Polyethylene (PE) as the binder material. With a ~10 wt% binder content, the compressive strength is 70-100 MPa, and the flexural strength is ~15 MPa. It offers a method to upcycle the large amount of waste plastics.

With an epoxy binder, algae-filler artificial timber was formed and tested. With a low binder content of 2-4 wt%, the flexural strength is comparable with those of typical softwoods. This study may open a door to carbon-sink buildings and infrastructures.

Low-binder-content green concrete based on ordinary portland cement (OPC) was the main focus of our work. Parameterized studies were carried out on inch-sized (~10 grams) small samples for prove-of-concept testing. The key factors include the compaction pressure, the OPC content (10-15%), and the water/cement ratio. Other important parameters are the sand type, the sand grain size, and the polymer additives. Through S-CSA, we scaled up the production to process brick-sized (~1 lb) samples. The requirement of the machine capacity and the mold complexity was much reduced. Advanced binders was explored. Microfibers (MF), ground quartz (GQ), and viscosity modifying admixture (VMA) were identified as the key components. With the advanced binder system, the compaction pressure was significantly reduced to 15 MPa. At this pressure level, samples with 15 wt% OPC could reach a compressive strength of ~80 MPa, and a flexural strength of ~12 MPa. The processing was further scaled up to fabricate paver-sized (~20 lbs)

samples and, eventually, full-sized (~500 lbs) OPC-based low-binder-content green concrete slabs. When the OPC content was 15 wt% and the compaction pressure was 15 MPa, the compressive strength and the flexural strength could reach ~100 MPa and ~15 MPa, respectively. The ductility was 1-2 orders of magnitude higher than that of conventional concrete.

Development of low-carbon-footprint green concrete is a critical element in the battle against the global climate change. New technologies are urgently required not only to reduce the carbon emission during the materials production, but also to mitigate the problems of the unavailable raw materials, the relatively poor cost efficiency, the difficulty in scaling up, etc. Our preliminary results demonstrate the potential of CSA and S-CSA. In the future, we can optimize the parameters to better fit with the identified market niche, e.g., precast slabs, panels, and columns. We will extend the CSA and S-CSA processes to new filler-binder systems, including municipal solid waste incineration (MSWI) ashes. For the ultralow-binder-content polymer concrete, more energy sufficient approaches will be developed for waste plastic binders. For the algae-derived artificial timber, we need to significantly increase the sample size.

REFERENCE

1. Abdel-Fattah H, El-Hawary MM. 1999. Flexural behavior of polymer concrete. Constr Build Mater. 13(5):253–262.

2. Advani SG, Hsiao K-T. 2012. Manufacturing techniques for polymer matrix composites (PMCs). Elsevier.

3. Ahmad SH, Lue DM. 1987. Flexure-shear interaction of reinforced high strength concrete beams. Struct J. 84(4):330–341.

4. Al-Salem SM, Lettieri P, Baeyens J. 2009. Recycling and recovery routes of plastic solid waste (PSW): A review. Waste Manag. 29(10):2625–2643.

5. Alujas A, Fernández R, Quintana R, Scrivener KL, Martirena F. 2015. Pozzolanic reactivity of low grade kaolinitic clays: Influence of calcination temperature and impact of calcination products on OPC hydration. Appl Clay Sci. 108:94–101. doi:https://doi.org/10.1016/j.clay.2015.01.028. https://www.sciencedirect.com/science/article/pii/S0169131715000459.

6. Ang BW, Su B. 2016. Carbon emission intensity in electricity production: A global analysis. Energy Policy. 94:56–63.

7. Association CEC. 2018. Key Facts and Figures. Key Facts.

8. Avet F, Snellings R, Alujas Diaz A, Ben Haha M, Scrivener K. 2016. Development of a new rapid, relevant and reliable (R3) test method to evaluate the pozzolanic reactivity of calcined kaolinitic clays. Cem Concr Res. 85:1–11. doi:https://doi.org/10.1016/j.cemconres.2016.02.015. https://www.sciencedirect.com/science/article/pii/S0008884616302368.

9. Balayssac JP, Détriché CH, Grandet J. 1995. Effects of curing upon carbonation of concrete. Constr Build Mater. 9(2):91–95.

10. Barnard PR. 1964. Researches into the complete stress-strain curve for concrete. Mag Concr Res. 16(49):203–210.

11. Beaudoin JJ. 1990. Handbook of fiber-reinforced concrete. Principles, properties, developments and applications.

12. Bedi R, Chandra R, Singh SP. 2013. Mechanical properties of polymer concrete. J Compos. 2013.

13. Benhelal E, Zahedi G, Shamsaei E, Bahadori A. 2013. Global strategies and potentials to curb CO2 emissions in cement industry. J Clean Prod. 51:142–161.

14. Billmeyer FW, Billmeyer FW. 1984. Textbook of polymer science. Wiley New York.

15. Biron M. 2013. Thermosets and composites: material selection, applications, manufacturing and cost analysis. Elsevier.

16. Blaas H, Kroeze C. 2014. Possible future effects of large-scale algae cultivation for biofuels on coastal eutrophication in Europe. Sci Total Environ. 496:45–53.

17. Blank LM, Narancic T, Mampel J, Tiso T, O'Connor K. 2020. Biotechnological upcycling of plastic waste and other non-conventional feedstocks in a circular economy. Curr Opin Biotechnol. 62:212–219.

18. Błaszczyński T, Król M. 2015. Usage of green concrete technology in civil engineering. Procedia Eng. 122:296–301.

19. Bloem DL. 1968. Concrete strength in structures. In: Journal Proceedings. Vol. 65. p. 176–187.

20. Bozkurt O, İslamoğlu M. 2013. Comparison of cement-based and polymer-based concrete pipes for analysis of cost assessment. Int J Polym Sci. 2013.

21. Buchanan AH, Levine SB. 1999. Wood-based building materials and atmospheric carbon emissions. Environ Sci Policy. 2(6):427–437.

22. Bux F, Chisti Y. 2016. Algae biotechnology: products and processes. Springer.

23. Caldarone MA. 2014. High-strength concrete: a practical guide. CRC press.

24. Charoenkit S, Yiemwattana S. 2016. Living walls and their contribution to improved thermal comfort and carbon emission reduction: A review. Build Environ. 105:82–94.

25. Chen T, Chow BJ, Wang M, Zhong Y, Qiao Y. 2017. High-Pressure Densification of Composite Lunar Cement. J Mater Civ Eng. 29(10):6017013.

26. Chen T, Chow BJ, Zhong Y, Wang M, Kou R, Qiao Y. 2018. Formation of polymer micro-agglomerations in ultralow-binder-content composite based on lunar soil simulant. Adv Sp Res. 61(3):830–836.

27. Cheng HL, Yang FH, Zhang J. 2012. Activation & Application Research in Concrete of Neimenggu High Aluminum Coal Gangue. In: Advanced Materials Research. Vol. 450. Trans Tech Publ. p. 1400–1404.

28. Chi Z, Elloy F, Xie Y, Hu Y, Chen S. 2014. Selection of microalgae and cyanobacteria strains for bicarbonate-based integrated carbon capture and algae production system. Appl Biochem Biotechnol. 172(1):447–457.

29. Consoli NC, Montardo JP, Donato M, Prietto PD. 2004. Effect of material properties on the behaviour of sand—cement—fibre composites. Proc Inst Civ Eng Improv. 8(2):77–90.

30. Cyr M. 2013. Influence of supplementary cementitious materials (SCMs) on concrete durability. In: Eco-efficient concrete. Elsevier. p. 153–197.

31. Dacheng GZZXZ, Ruqi W. 1982. Experimental Investigation of the Complete Stress-Strain Curve of Concrete [J]. J Build Struct. 1:1–12.

32. Darnell GR. 1991. Sulfur polymer cement, a new stabilization agent for mixed and Low-level radioactive waste. EG and G Idaho, Inc., Idaho Falls, ID (United States).

33. Dębowski M, Zieliński M, Grala A, Dudek M. 2013. Algae biomass as an alternative substrate in biogas production technologies. Renew Sustain Energy Rev. 27:596–604.

34. Deja J, Uliasz-Bochenczyk A, Mokrzycki E. 2010. CO2 emissions from Polish cement industry. Int J Greenh Gas Control. 4(4):583–588.

35. Detz RJ, van der Zwaan B. 2019. Transitioning towards negative CO2 emissions. Energy Policy. 133:110938.

36. Do J, Soh Y. 2003. Performance of polymer-modified self-leveling mortars with high polymer–cement ratio for floor finishing. Cem Concr Res. 33(10):1497–1505.

37. Duffy JE, Canuel EA, Adey W, Swaddle JP. 2009. Biofuels: algae. Science (80-). 326(5958):1345.

38. Elahi MMA, Shearer CR, Reza ANR, Saha AK, Khan MNN, Hossain MM, Sarker PK. 2021. Improving the sulfate attack resistance of concrete by using supplementary cementitious materials (SCMs): A review. Constr Build Mater. 281:122628.

39. Fasahati P, Liu JJ. 2015. Economic, energy, and environmental impacts of alcohol

dehydration technology on biofuel production from brown algae. Energy. 93:2321–2336.

40. Figovsky O, Beilin D. 2013. Advanced polymer concretes and compounds. CRC Press.

41. Gao T, Shen L, Shen M, Liu L, Chen F. 2016. Analysis of material flow and consumption in cement production process. J Clean Prod. 112:553–565.

42. Garcia-Lodeiro I, Palomo A, Fernández-Jiménez A. 2015. An overview of the chemistry of alkali-activated cement-based binders. In: Handbook of alkali-activated cements, mortars and concretes. Elsevier. p. 19–47.

43. Garg C, Jain A. 2014. Green concrete: efficient & eco-friendly construction materials. Impact J. 2(2):259–264.

44. Gourmelon G. 2015. Global plastic production rises, recycling lags. New Worldwatch Inst Anal Explor trends Glob Plast Consum Recycl Recuper http//www worldwatch org. 208.

45. Grace NF, Jensen EA, Eamon CD, Shi X. 2012. Life-cycle cost analysis of carbon fiber-reinforced polymer reinforced concrete bridges. ACI Struct J. 109(5):697–704.

46. Green DW, Winandy JE, Kretschmann DE. 1999. Mechanical properties of wood. Wood Handb wood as an Eng Mater Madison, WI USDA For Serv For Prod Lab 1999 Gen Tech Rep FPL; GTR-113 Pages 41-445. 113.

47. Hardjito D, Wallah SE, Sumajouw DMJ, Rangan BV. 2004. On the development of fly ash-based geopolymer concrete. Mater J. 101(6):467–472.

48. Harper CA. 2002. Handbook of plastics, elastomers, and composites. McGraw-Hill New York.

49. Hasanbeigi A, Price L, Lin E. 2012. Emerging energy-efficiency and CO2 emission-reduction technologies for cement and concrete production: A technical review. Renew Sustain Energy Rev. 16(8):6220–6238.

50. Ho DWS, Cui QY, Ritchie DJ. 1989. The influence of humidity and curing time on the quality of concrete. Cem Concr Res. 19(3):457–464.

51. Hossain ABMS, Salleh A, Boyce AN, Chowdhury P, Naqiuddin M. 2008. Biodiesel fuel production from algae as renewable energy. Am J Biochem Biotechnol. 4(3):250–254.

52. Ji J, Zhang Z, Yang L. 2017. Carbon emission reduction decisions in the retail-/dual-channel supply chain with consumers' preference. J Clean Prod. 141:852–867.

53. Joosten LAJ. 2001. The industrial metabolism of plastics: analysis of material flows, energy consumption and CO2 emissions in the lifecycle of plastics.

54. Juenger MCG, Siddique R. 2015. Recent advances in understanding the role of supplementary cementitious materials in concrete. Cem Concr Res. 78:71–80.

55. Karthik J, Jagannathan P. 2015. Study Of Strength Parameter Of Concrete By Replacing Cement By Flyash Enriched With Microbial Agents. Int Res J Eng Technol. 2(01):1–5.

56. Kazanskaya LF, Isakovsky VI, Fadeeva SA. 2019. Technological properties of self-compacting concrete mixtures with ground quartz sand. Int J Innov Technol Explor Eng. 8(12):799–803.

57. Kim J-K, Moon Y-H, Eo S-H. 1998. Compressive strength development of concrete with different curing time and temperature. Cem Concr Res. 28(12):1761–1773.

58. Kim Y, Worrell E. 2002. International comparison of CO2 emission trends in the iron and steel industry. Energy Policy. 30(10):827–838.

59. Kisku N, Joshi H, Ansari M, Panda SK, Nayak S, Dutta SC. 2017. A critical review and assessment for usage of recycled aggregate as sustainable construction material. Constr Build Mater. 131:721–740.

60. Kong F, Evans RH. 1983. Handbook of structural concrete.

61. Kou R, Zhong Y, Kim J, Wang Q, Wang M, Chen R, Qiao Y. 2019. Elevating low-emissivity film for lower thermal transmittance. Energy Build. 193:69–77.

62. Kou R, Zhong Y, Qiao Y. 2019. Effects of anion size on flow electrification of polycarbonate and polyethylene terephthalate. Appl Phys Lett. 115(7):73704.

63. Lachemi M, Hossain KMA, Lambros V, Nkinamubanzi P-C, Bouzoubaâ N. 2004. Self-consolidating concrete incorporating new viscosity modifying admixtures. Cem Concr Res. 34(6):917–926.

64. Lagerblad B, Vogt C. 2004. Ultrafine particles to save cement and improve concrete properties. Cement och Betong Institutet.

65. Lee Y, Pirt SJ. 1984. CO2 absorption rate in an algal culture: effect of pH. J

Chem Technol Biotechnol Biotechnol. 34(1):28–32.

66. Leemann A, Winnefeld F. 2007. The effect of viscosity modifying agents on mortar and concrete. Cem Concr Compos. 29(5):341–349.

67. Leet K, Bernal D. 1982. Reinforced concrete design. McGraw-Hill New York.

68. Lew D, Bakke J, Bloom A, Brown P, Caspary J, Clack C, Miller N, Orths A, Silverstein A, Simonelli J. 2021. Transmission Planning for 100% Clean Electricity: Enabling Clean, Affordable, and Reliable Electricity. IEEE Power Energy Mag. 19(6):56–66.

69. Licht S. 2017. Co-production of cement and carbon nanotubes with a carbon negative footprint. J CO2 Util. 18:378–389.

70. Liew KM, Sojobi AO, Zhang LW. 2017. Green concrete: Prospects and challenges. Constr Build Mater. 156:1063–1095.

71. Lloyd N, Rangan V. 2010. Geopolymer concrete with fly ash. In: Proceedings of the Second International Conference on sustainable construction Materials and Technologies. UWM Center for By-Products Utilization. p. 1493–1504.

72. MacGregor JG, Wight JK, Teng S, Irawan P. 1997. Reinforced concrete: mechanics and design. Prentice Hall Upper Saddle River, NJ.

73. Madlool NA, Saidur R, Hossain MS, Rahim NA. 2011. A critical review on energy use and savings in the cement industries. Renew Sustain Energy Rev. 15(4):2042–2060.

74. Mahasenan N, Smith S, Humphreys K. 2003. The cement industry and global climate change: current and potential future cement industry CO2 emissions. In: Greenhouse Gas Control Technologies-6th International Conference. Elsevier. p. 995–1000.

75. Marceau ML, Gajda J, VanGeem MG. 2002. Use of fly ash in concrete: Normal and high volume ranges. PCA R&D Ser.(2604).

76. McLellan BC, Williams RP, Lay J, Van Riessen A, Corder GD. 2011. Costs and carbon emissions for geopolymer pastes in comparison to ordinary portland cement. J Clean Prod. 19(9–10):1080–1090.

77. Mehta PK. 1986. Concrete. Structure, properties and materials.

78. Mehta PK. 2002. Greening of the concrete industry for sustainable development. Concr Int. 24(7):23–28.

79. Mehta PK. 2009. Global concrete industry sustainability. Concr Int. 31(2):45–48.

80. Meyer C. 2009. The greening of the concrete industry. Cem Concr Compos. 31(8):601–605.

81. Meyer T, Keurentjes JTF. 2005. Handbook of polymer reaction engineering. Wiley-VCH Verlag.

82. Mihranyan A. 2011. Cellulose from cladophorales green algae: From environmental problem to high-tech composite materials. J Appl Polym Sci. 119(4):2449–2460.

83. Mindess S, Young JF. 2002. Concrete. Prentice Hall.

84. Mirza SA, MacGregor JG, Hatzinikolas M. 1979. Statistical descriptions of strength of concrete. J Struct Div. 105(6):1021–1037.

85. Moreira D, Pires JCM. 2016. Atmospheric CO2 capture by algae: negative carbon dioxide emission path. Bioresour Technol. 215:371–379.

86. Motorwala A, Shah V, Kammula R, Nannapaneni P, Raijiwala DB. 2013. Alkali activated fly-ash based geopolymer concrete. Int J Emerg Technol Adv Eng. 3(1):159–166.

87. Neville AM, Brooks JJ. 1987. Concrete technology. Longman Scientific & Technical England.

88. Oh K, Chen T, Gasser A, Kou R, Qiao Y. 2019. Compaction self-assembly of ultralow-binder-content particulate composites. Compos Part B Eng. 175:107144.

89. Oh K, Chen T, Kou R, Yi H, Qiao Y. 2020a. Ultralow-Binder-Content Thermoplastic Composites Based on Lunar Soil Simulant. Adv Sp Res. doi:https://doi.org/10.1016/j.asr.2020.07.041. http://www.sciencedirect.com/science/article/pii/S0273117720305500.

90. Oh K, Chen T, Kou R, Yi H, Qiao Y. 2020b. Compaction Self-Assembly of Ultralow-Binder-Content Thermoplastic Composites Based on Lunar Soil Simulant. arXiv Prepr arXiv200406273.

91. Oh K, Yi H, Chen T, Chow BJ, Kou R, Qiao Y. 2020. Impact formation of

ultralow-binder-content composite “lunar cement.” CEAS Sp J.:1–5.

92. Oh K, Yi H, Kou R, Qiao Y. 2020a. Compaction self-assembly of a low-binder-content geopolymer material. J Mater Sci. doi:10.1007/s10853-020-05069-5.

93. Oh K, Yi H, Kou R, Qiao Y. 2020b. Sectioned processing of compaction self-assembly of an ultralow-binder-content particulate composite. Compos Commun.:100588.

94. Ohama Y. 1995. Handbook of polymer-modified concrete and mortars: properties and process technology. William Andrew.

95. Ollitrault-Fichet R, Gauthier C, Clamen G, Boch P. 1998. Microstructural aspects in a polymer-modified cement. Cem Concr Res. 28(12):1687–1693.

96. Pacheco-Torgal F, Jalali S, Labrincha J, John VM. 2013. Eco-efficient concrete. Elsevier.

97. Papadakis VG. 1999. Effect of fly ash on Portland cement systems: Part I. Low-calcium fly ash. Cem Concr Res. 29(11):1727–1736.

98. Park R, Paulay T. 1975. Reinforced concrete structures. John Wiley & Sons.

99. Pascault J-P, Sautereau H, Verdu J, Williams RJJ. 2002. Thermosetting polymers. CRC press.

100. Pascault J-P, Williams RJJ. 2009. Epoxy polymers: new materials and innovations. John Wiley & Sons.

101. Pavlů T. 2018. The Utilization of Recycled Materials for Concrete and Cement Production-A Review. In: IOP Conference Series: Materials Science and Engineering. Vol. 442. IOP Publishing. p. 12014.

102. Popovics S. 1973. A numerical approach to the complete stress-strain curve of concrete. Cem Concr Res. 3(5):583–599.

103. Popovics S. 1998. Strength and related properties of concrete: A quantitative approach. John Wiley & Sons.

104. Rabi M, Cashell KA, Shamass R. 2019. Flexural analysis and design of stainless steel reinforced concrete beams. Eng Struct. 198:109432.

105. Ragan MA, Craigie JS. 1976. Physodes and the phenolic compounds of brown algae. Isolation and characterization of phloroglucinol polymers from Fucus vesiculosus (L.). Can J Biochem. 54(1):66–73.

106. Rangan BV. 2008. Fly ash-based geopolymer concrete.

107. Rubin AJ, Cassel EA, Henderson O, Johnson JD, Lamb III JC. 1966. Microflotation: New low gas-flow rate foam separation technique for bacteria and algae. Biotechnol Bioeng. 8(1):135–151.

108. Schmidt M, Fehling E, Geisenhanslüke C. 2004. Ultra high performance concrete (UHPC). In: Proceedings of the international symposium on ultra High Performance Concrete, Kassel, germany. university of Kassel, germany.

109. Scrivener K, Martirena F, Bishnoi S, Maity S. 2018. Calcined clay limestone cements (LC3). Cem Concr Res. 114:49–56.

110. Shakhmenko G, Birsh J. 1998. Concrete mix design and optimization. In: Proceedings of the 2nd International Symposium in Civil Engineering. p. 1–8.

111. Sharma M, Bishnoi S, Martirena F, Scrivener K. 2021. Limestone calcined clay cement and concrete: A state-of-the-art review. Cem Concr Res. 149:106564.

112. Shi C, Wu Z, Xiao J, Wang D, Huang Z, Fang Z. 2015. A review on ultra high performance concrete: Part I. Raw materials and mixture design. Constr Build Mater. 101:741–751.

113. Siddique R. 2011. Utilization of silica fume in concrete: Review of hardened properties. Resour Conserv Recycl. 55(11):923–932.

114. Singh B, Ishwarya G, Gupta M, Bhattacharyya SK. 2015. Geopolymer concrete: A review of some recent developments. Constr Build Mater. 85:78–90.

115. Sivakrishna A, Adesina A, Awoyera PO, Kumar KR. 2020. Green concrete: A review of recent developments. Mater Today Proc. 27:54–58.

116. Song PS, Hwang S. 2004. Mechanical properties of high-strength steel fiber-reinforced concrete. Constr Build Mater. 18(9):669–673.

117. Soratana K, Landis AE. 2011. Evaluating industrial symbiosis and algae cultivation from a life cycle perspective. Bioresour Technol. 102(13):6892–6901.

118. Su H, Hong Y, Chen T, Kou R, Wang M, Zhong Y, Qiao Y. 2019. Fatigue

Behavior of Inorganic-Organic Hybrid “Lunar Cement.” Sci Rep. 9(1):1–8.

119. Suhendro B. 2014. Toward green concrete for better sustainable environment. Procedia Eng. 95:305–320.

120. Suherman H, Sulong AB, Sahari J. 2013. Effect of the compression molding parameters on the in-plane and through-plane conductivity of carbon nanotubes/graphite/epoxy nanocomposites as bipolar plate material for a polymer electrolyte membrane fuel cell. Ceram Int. 39(2):1277–1284.

121. Talbot P, Gortares MP, Lencki RW, De la Noüe J. 1991. Absorption of CO2 in algal mass culture systems: a different characterization approach. Biotechnol Bioeng. 37(9):834–842.

122. Tatara RA. 2017. Compression molding. In: Applied plastics engineering handbook. Elsevier. p. 291–320.

123. Tedia A, Maru DS. 2014. Cost, Analysis and Design of Steel-Concrete Composite Structure RCC Structure. IOSR J Mech Civ Eng. 11(1):54–59.

124. Thomas M. 2013. Supplementary cementing materials in concrete. CRC press.

125. Torgal FP, Miraldo S, Labrincha JA, De Brito J. 2012. An overview on concrete carbonation in the context of eco-efficient construction: Evaluation, use of SCMs and/or RAC. Constr Build Mater. 36:141–150.

126. Wang J, Dai Q, Si R, Guo S. 2018. Investigation of properties and performances of Polyvinyl Alcohol (PVA) fiber-reinforced rubber concrete. Constr Build Mater. 193:631–642.

127. Wells ML, Potin P, Craigie JS, Raven JA, Merchant SS, Helliwell KE, Smith AG, Camire ME, Brawley SH. 2017. Algae as nutritional and functional food sources: revisiting our understanding. J Appl Phycol. 29(2):949–982.

128. Wijesekara I, Kim S. 2015. Application of marine algae derived nutraceuticals in the food industry. Mar algae Extr Process Prod Appl. 35:627–638.

129. Wilson ML, Kosmatka SH. 2011. Design and control of concrete mixtures. Portl Cem Assn, Skokie, Ill.

130. Wongpa J, Kiattikomol K, Jaturapitakkul C, Chindaprasirt P. 2010. Compressive strength, modulus of elasticity, and water permeability of inorganic polymer concrete. Mater Des. 31(10):4748–4754.

131. Wood SL. 1992. Evaluation of the long-term properties of concrete. Portland Cement Association Skokie.

132. Worrell E, Price L, Martin N, Hendriks C, Meida LO. 2001. Carbon dioxide emissions from the global cement industry. Annu Rev energy Environ. 26(1):303–329.

133. Xu G, Shi X. 2018. Characteristics and applications of fly ash as a sustainable construction material: A state-of-the-art review. Resour Conserv Recycl. 136:95–109.

134. Yi H, Oh K, Kou R, Qiao Y. 2020a. Sand-filler structural material with a low content of polyethylene binder. Sustain Mater Technol. 25. doi:10.1016/j.susmat.2020.e00194.

135. Yi H, Oh K, Kou R, Qiao Y. 2020b. Ultralow-Binder-Content Artificial Timber Based on Algae Filler. arXiv Prepr arXiv200602574.

136. Zhang S, Worrell E, Crijns-Graus W. 2015. Evaluating co-benefits of energy efficiency and air pollution abatement in China's cement industry. Appl Energy. 147:192–213.

137. Zhong Y, Kou R, Wang M, Qiao Y. 2019. Synthesis of centimeter-scale monolithic SiC nanofoams and pore size effect on mechanical properties. J Eur Ceram Soc. 39(7):2566–2573.

138. Zollo RF. 1997. Fiber-reinforced concrete: an overview after 30 years of development. Cem Concr Compos. 19(2):107–122.